ORGANIC SEMICONDUCTOR DEVICES FOR CHEMICAL SENSING AND BIO INTERFACES

by
Kalpana Besar

A dissertation submitted to Johns Hopkins University in conformity with the requirements for the degree of Doctor of Philosophy

Baltimore, Maryland
March, 2016

Abstract

The scope of this work is to establish organic field effect transistors (OFET) as a viable platform for sensing and for interfacing between biological and electronic materials.

In section 1 we discuss our approaches and strategies for designing gas sensor platforms for ammonia and ethylene using the OFET platform. For ammonia sensor, we devised an organic field-effect transistor (OFET) structure with tris(pentafluorophenyl)borane (TPFB) as ammonia receptor. OFETs with this additive could detect concentrations of 450 ppb v/v, with a limit of detection of 350 ppb. For printable versions of ammonia sensors, we simplified the OFET structure by replacing the gate electrode and the dielectric deposition steps with the introduction of static charges on the back surface of the polyethylene terephthalate (PET) substrate by corona charging, a procedure that is adaptable to roll-to-roll processing. This technique considerably decreased the time and the cost of production.

For ethylene sensors, we developed an OFET platform with an organic semiconductor layer containing palladium particles as ethylene receptor. With this unique active sensing layer, we could sense concentration of 50-ppm v/v.

In section 2, we studied OSCs as candidates for developing bio interfaces. In the first part of this section we investigated OFETs as an electronic bio sensing platform. We designed an OFET-based biosensor with a new receptor–antibody-functionalized composite top dielectric layer consisting of a fluorinated polymer (CYTOP) and

vapor-deposited hydrocarbon (tetratetracontane). Using glial fibrillary acidic protein (GFAP) as a model protein analyte, this sensor platform demonstrated significant selectivity and recognition of target protein even in concentrated non-target protein backgrounds.

In second part of section 2, we studied electrical properties of functionalized self-assembling nanowires using OFET structures. The effect of systematic changes in amino acid composition on the semiconducting/conducting functionality of the nanostructures was analyzed. The study shows that these self-assembling peptides can be used successfully to transmit electronic signals over biologically relevant distances. This library of nanowires should be instrumental in electrically manipulating and stimulating cells for bioengineering purposes.

The strategies and the results discussed here open new pathways for the future development of these areas.

Readers

Professor Howard E. Katz (Advisor)

Professor John D. Tovar (Chair of the defense Committee)

To my Parents

Acknowledgements

I would like to take this opportunity to thank Professor Howard Katz for giving me this chance to work with a wonderful group of people and for supporting me to pursue all my scientific theories and out of the box ideas for last five years. You have taught me to have a positive outlook about research and life in general by showing me how I can learn something invaluable from each and every experience no matter what the results are.

I need to give a very special thanks to my mentor Weiguo Huang, who has been the perfect mentor and a wonderful friend through out. You have shown immense patience in answering each and every query with a smile and have practically taught me how to conduct and design a good experiment. Thank you for all your support and encouragement, without you I would have been lost.

I can't come up with a big enough gesture to thank all the wonderful people in Katz group; Dr. Ming-Ling Yeh, Dr. Weiguo Huang, Dr. Josue F. Martinez-Hardigree, Robert Ireland, Dr. Thomas Dawidczyk, Dr. Jasmine Sinha, Dr. Xin Guo, Olivia Alley, Dr. Yu Liu, Jennifer Dailey, Wenmin Guo, Dr. Xingang Zhao, Hyun-June Jang, Dr. Xin Guo, Dr. Deepa Madan. Thank you for being my friends and a very strong support system.

I owe a big thanks to all the collaborators with whom I had the good fortune to work. Material science is definitely a very diverse field, which exposed me to various interdisciplinary research opportunities. Thank you Professor Patrick N. Breysse, Professor Ana Rule (School of Public Health School); Professor Ioannis J. Kymissis,

Dr. Shyuan Yang (University of Columbia); Professor John D. Tovar, Herdeline Ann Ardona, Dr. Allix Sanders (Department of Chemistry, Johns Hopkins University) for giving me invaluable insights and support for my research. Meeting people from such varied backgrounds has definitely turned my PhD into a very dynamic and fascinating journey. Of course, it also expanded the resources at my disposal.

Mum and Dad, Rachana, Gajender, Sunny Chugh and Fozia Ahmed; thank you for being the most amazing family and for all your faith, love and unwavering support! You define me.

A very special thank to Misha Miglani, Manish Mandal, Dr. Asma Akhlaq, Kirtika Sharma, Bhaskar Chinnuri and Aditya Patel for being the most amazing friends.

Finally I would like to thank my Thesis Defense Committee; Prof. James Spicer, Prof. Hai-Quan Mao, Prof. John D. Tovar, Prof. Susanna Thon, Prof. Jonah Erlebacher, Prof. Arthur Bragg for giving their invaluable advice, time and insight.

Note: Specific acknowledgements for various contributions towards different projects are stated at the end of each chapter.

Table of Contents

List of Figures

List of Tables

List of schemes

Chapter 1

Introduction

1.1 Organic Semiconductors

Inorganic semiconductors like Si and Ge became the backbone of the electronics industry after the successful demonstration of the field effect in 1947 by Bell Laboratries[1]. After that introduction of solid-state devices paved the path for the microelectronics revolution. However, around the middle of the last century, the discovery of respectable dark current carrying capacity of organic materials[2,3] had initiated the advent of another very different electronic revolution called organic electronics. The need for large area, flexible, printable, low cost electronics has fueled the tremendous progress made in this field over a very short period of time.

The observation of conducting behavior of organic materials can be traced back to the early 20th Century[4,5]. In 1906 Pochettino discovered the photoconductivity in anthracene[6,7] but it wasn't until 1960 that electroluminescence in molecular crystals was discovered, which sparked a serious interest in the research community for molecular crystals[8,9]. Even after establishing the basic principle of electroluminescence using organic materials, the use of organic material for practical devices was a nothing more than a pipe dream due to severe drawbacks like low current and light densities and instability under ambient conditions[9]. It was only after the successful synthesis and controlled doping of conjugated polymers in 1970 that organic polymers became a viable practical option; this huge achievement was

recognized with the Nobel Prize in chemistry in 2000[9,10]. The undoped organic semiconductors (OSCs) received well-deserved attention much later in the 1980s after successful demonstration of an organic semiconductor based photovoltaic cell[9,11] along with the fabrication of first the organic field effect transistor (OFET)[9,12].

While most of the conventional organic compounds are insulators, recently a huge number of systems have been developed with conducting or semiconducting properties. The conjugated π bonds in the organic materials with delocalized orbitals are responsible for the deviation from insulating behavior of normal organic materials. In particular the organic materials with a band gap of less than 3.5 eV are categorized as organic semiconductors. Like inorganic semiconductors, organic semiconductors can conduct charges, emit or absorb light given the necessary stimulus. Today organic semiconductors are successfully used in electronic devices such as radiofrequency identification (RFID), solar cells, light emitting diodes and sensors. Companies like Thin Film Electronics, Universal Display, Sumitomo, BASF, and Solvay are aiming to commercialize these products based on organic semiconductors.

Organic semiconductors can be widely divided into two categories namely small molecules (e.g. pentacene) or oligomers and polymers (e.g. Poly (3-hexylthiophene-2,5-diyl) ((P3HT)). Chemical structures of some of the common organic semiconductors are illustrated in Figure 1. The major families of organic semiconductors are oligoacenes (e.g. pentacene and rubrene), oligothiophenes, discotic liquid crystals (e.g. systems based on triphenylene), triphenylamines (e.g. prototypical4,4'-bis(N-m-poly-N-phenylamino)biphenyl(TPD)), perylenes,

tetrathiafulvalenes, fullerenes, polyparaphenylene, polyparaphenylenevinylene, polyfluorene and polythiophene[13].

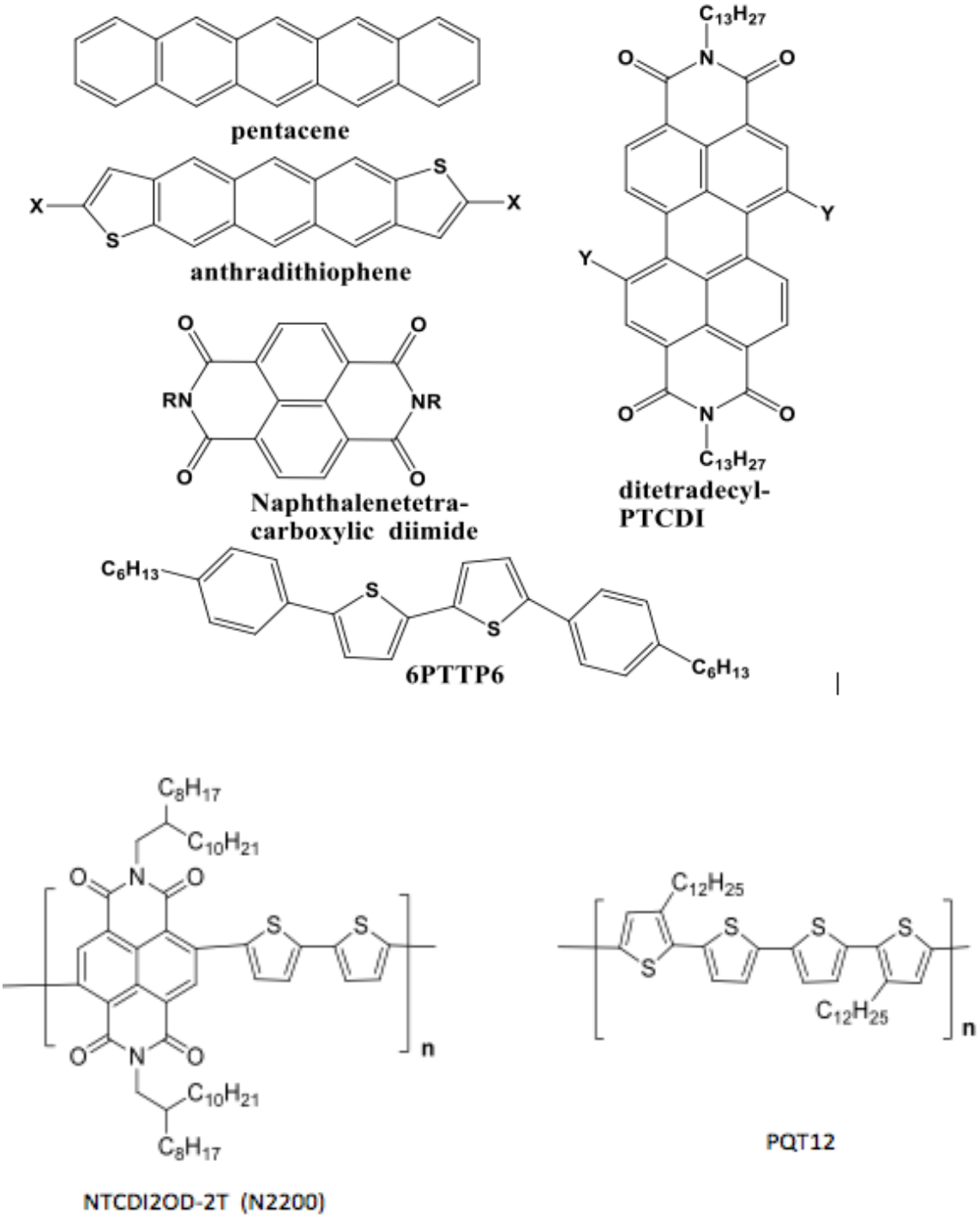

Figure 1 Chemical structures of some common organic semiconductors.

Organic semiconductors have conjugated π bonds; free radicals and charge transfer complexes, which are responsible for the charge transport[7]. Several plausible charge transport mechanisms have been proposed to understand the physics behind these materials but we are still not close to understanding and establishing the actual mechanisms with certainty[7,13].

In inorganic semiconductors the strong interaction between atoms, long-range order of atomic packing and perfect crystal structure leads to the overlapping of the atomic orbitals, delocalizing electronic state, and forming valence and conduction band separated by the forbidden gap. Thermal, optical or electrical excitation creates charge carriers (electrons) in the conduction band, which can move freely resulting in electrical conduction. On the other hand organic semiconductors have polycrystalline structures with many chemical and structural defects. Even in highly ordered organic materials, interactions between different molecules, like van der Waals interactions, hydrogen bonding and $\pi - \pi$ interactions, are mostly weak in nature, resulting in formation of narrow energy bands, namely, (the highest occupied molecular orbital) HOMO and (the lowest unoccupied molecular orbital) LUMO. These are, easily disrupted by the various types of disorder present in the material. Thus, although the band theory and concept of charge excitation hold some merit in explaining the conduction mechanism of organic semiconducting, it is the phonon assisted quantum mechanical tunneling or hopping mechanism across the band discontinuities which is considered to be largely responsible for charge transport in organic materials[9,14].

The recent growing interest in organic electronics is mainly due to the fact that this class of materials enjoys much greater tunability for optimizing its optoelectronic properties through chemical tailoring compared to other inorganic counterparts. Also, the possibility of introducing printing technology to achieve large area devices on various substrates (such as flexible PET or nano-paper) makes OSCs highly attractive for low-cost high-efficient fabrication purposes. Nevertheless, OSCs exhibit several drawbacks such as low charge carrier mobilities, inferior switch speeds, short operational lifetimes, and poor environmental stability compared with many inorganic analogs. Therefore, in order to take better advantage of these materials, it is wise to exploit their potential applications in circumstances in which the performances will not be limited by the above drawbacks, and the chemical sensitivity can be a bonus rather than a limitation.

Sensors are a particularly promising potential application for OSCs; high electronic circuit switching speeds are not required for sensors because the system response speed is limited by dynamic biochemical reactions and physical and chemical adsorption and desorption procedures at active sensing sites. More importantly, sensor sensitivity and selectivity can be optimized by controllably modifying OSC molecular structures. The potential to fabricate large area sensor devices on various flexible substrates using printing technology is highly interesting and attractive for wearable, conformable devices in particular.

1.2 Organic Field Effect Transistor (OFET)

Over the past decade, organic field effect transistors (OFETs) have been established as vehicles for alternative electronic technologies such as wearable electronics and robotic skin due to their attributes like printability, low cost, and flexibility[15]. From the first thiophene-based OFET reported by Koezuka *et al*. in 1987[12] to fully printable plastic based OFETs, several major milestones have been achieved, such as very high mobility, low hysteresis, and steadily improving stability[16–18]. An ultralight thin (<2 μm, 3 g m^{-2}) OFET reported by M. Kaltenbrunner *et al.* with a self-healing aluminum oxide gate dielectric added a new level to robustness and stability of OFETs[19]. The better understanding of the physics behind OFETS can enable tremendous improvement in OFET-based circuits.

An OFET is basically a three terminal device, namely gate, source and drain. It can be pictured as a sandwich structure consisting of a capacitor with one plate as the gate and the other plate as the semiconductor layer. The semiconductor layer is electrically interfaced with the other two electrodes. Figure 2 illustrates the basic schematic of an OFET.

The Gate electrode is made up of conductive material such as highly doped silicon or gold, platinum or silver deposited on an insulating substrate like glass or Mylar. As all the other layers are very thin, evaporated or printed films, which cannot support themselves structurally, the gate serves the dual purpose of the structural base for the device and of the conductive gate terminal.

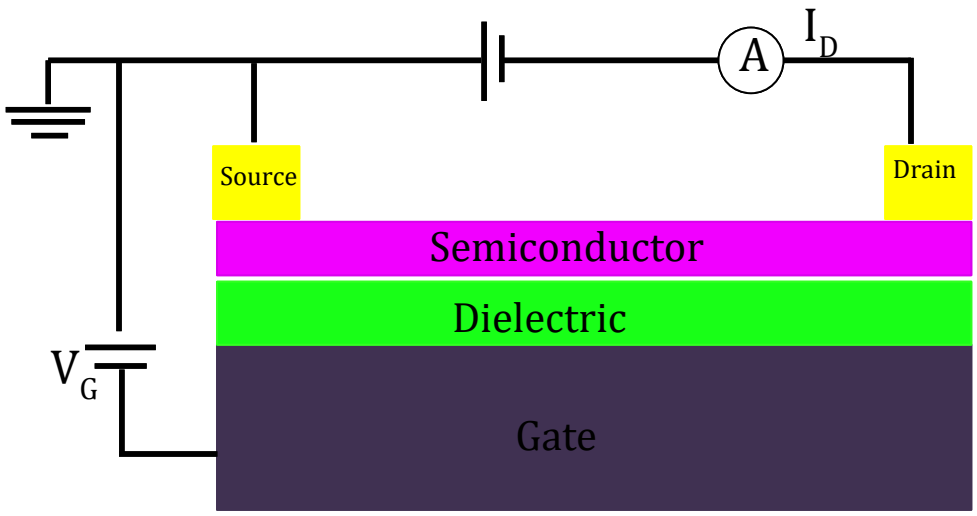

Figure 2 General schematic of an organic field effect transistor

Typically silicon dioxide is preferred as the dielectric material if silicon is the gate material but for making flexible devices, printable insulating polymers like polystyrene, parylene and poly (methyl methacrylate) (PMMA) are used. Organic semiconductor layers can be printed or spin coated using polymers like poly(3-hexylthiophene-2,5-diyl) (P3HT) or can be deposited using physical vapor deposition if small molecules like pentacene or (naphthalenetetracarboxylic diimide) (NTCDI) are being used. Source and drain electrodes are made of conductive materials (metals or polymers).

During operation, the capacitor in an OFET is charged by applying gate voltage (V_g) between the source and the gate electrodes which in turn accumulates charge carriers in a conductive channel at the interface of the insulating and the semiconductor layer; this channel can be easily modulated by the gate voltage applied. The charges in the channel are mobile in nature and thus on application of a

voltage (V_d) difference between source and drain, a current flows and this is known as the on state of the OFET.

An OFET generally operates in the accumulation regime as organic semiconductors have a very low intrinsic conductivity and the film is generally not doped intentionally. Source and drain electrodes are used to inject and collect charges from the semiconductor layer. A minimum nonzero gate voltage called threshold voltage (V_t) needs to be applied before a conduction channel can be formed. When a gate voltage V_g-V_t>0 is applied a conductive channel is formed at the interface with charges opposite in polarity to V_g applied. The concept of nonzero threshold voltage comes from several factors: the existence of shallow traps due to impurities and imperfections that needs to be filled in order to form a conductive channel is one; another contribution comes from the presence of dipoles at the insulator semiconductor interface; yet another and very important factor is the Fermi level mismatch between source, drain and the semiconductor material which requires a nonzero gate voltage to shift and match the Fermi levels[18,20].

The charge density in the channel is fairly uniform when V_d=0, on application of a voltage V_d, the potential across the channel is modified and so is the density of charge carriers. Equation (1) and (2) defines the relationship of the drain current with the drain and the gate voltages.

$$I_d = \frac{W}{L} C_i \mu \left(V_g - V_t - \frac{V_d}{2} \right) V_d , \quad V_d < V_g - V_t \qquad (1)$$

$$I_{dsat} = \frac{W}{2L} C_i \mu \left(V_g - V_t \right)^2 , \quad V_d > V_g - V_t \qquad (2)$$

$I_d = Drain\ current$

$W = Width\ of\ the\ channel$

$L = Length\ of\ the\ channel$

$C_i = Capacitance\ of\ the\ insulating\ layer$

$\mu = Mobility$

$Mobility\ is\ usually\ dependent\ on\ gate\ voltage\ and\ contact\ resistance$

$V_g = Gate\ voltage$

$V_t = Threshold\ voltage$

$V_d = Drain\ voltage$

Equation (1) governs the drain current when $V_d < V_g - V_t$. In this case the channel carrier density is still fairly uniform and therefore drain current increases linearly with the V_d. This regime is called the linear regime[20].

Equation (2) dictates the drain current behavior, when V_d is very close to $V_g - V_t$. In this case the potential gradient between the gate and the drain electrodes becomes 0 resulting in depletion of charges from a region close to the drain electrode. Any additional increase in V_d results in increase of the depletion region. This is called "pinching off " of the channel and at this stage the drain current is saturated[20].

Figure 3 demonstrates the transfer and output curves for an OFET with TIPS-pentacene as the semiconductor.

1.2.1 Section 1

Organic Field Effect Transistor as Sensing Platform For Gases

For years metal oxides, conductive polymers chemiresistors and inorganic field effect transistor sensors have been used for chemical sensing due to their reliability and portability, but these techniques still suffer from drawbacks like lack of high sensitivity, selectivity and high power consumption. The tendencies of OSCs to interact with the surroundings and the ease with which they can be tailored chemically among other suitable aspects have made them a prime choice for study and development of chemical sensors.

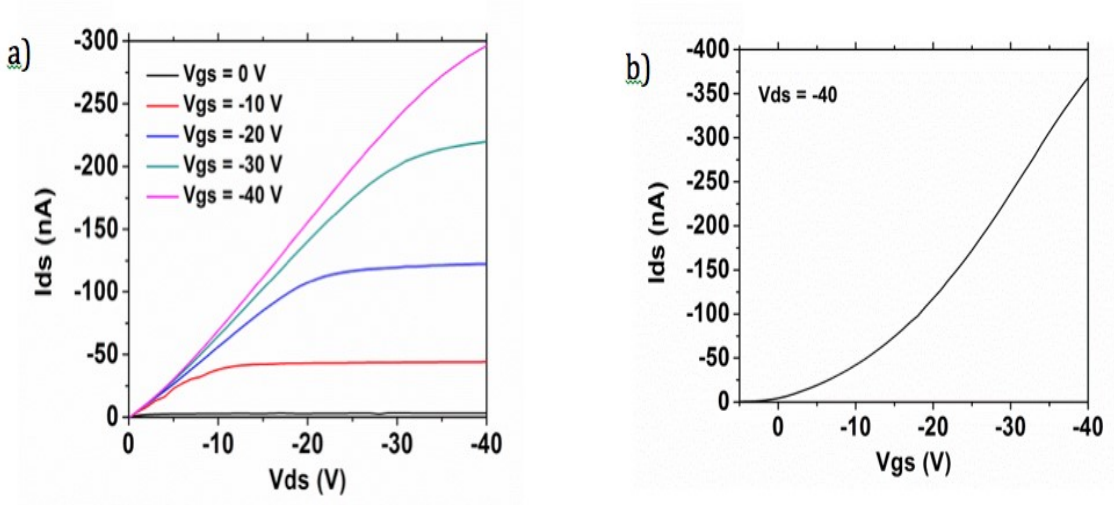

Figure 3 a) Output curve b) Transfer curve of a TIPS pentacene OFET

In OFETs the OSC film is the analytical sensing membrane. The separate "off" ($(V_t<V_g)$ and "on" ($V_t>V_g$) regime both have a different sensing mechanism[14]. This makes an OFET a more comprehensive multiparametric sensing system. When $V_g=0$ or less than V_t, the OFET is considered to be in the "off" state, and any drain current

at this point is essentially the intrinsic current of the OSC. At this stage the analyte will essentially permeate through the OSC and interact with its bulk. Any resulting change in the intrinsic conductivity is recorded as the measure of sensitivity of that particular analyte. This mechanism is basically the same mechanism as in the chemiresistive sensors. While during the "on" regime of the OFET the I_d flows through the 2- dimensional conduction channel and the interaction between the analyte and the active membrane not only influences the I_d but also affects the other parameters like threshold voltage and field effect mobility. Thus "on" state and "off" mechanisms are entirely different and both can supplement the sensing information in a complementary fashion, a clear advantage over the much relied upon chemiresistors. The performance of OFET devices is highly related to morphologies of different films[21–26] Specific morphological factors include grain size, connectivity, orientation or packing disorder in the films as all these factors influence density of traps and the grain boundary potential barrier which in turn directly affect the mobility and threshold voltage of the device[27].

The sensing mechanism for an OFET based sensor is deeply intertwined with the conduction mechanism[14]. For gas sensors, the most plausible sensing mechanism being proposed is that the gas molecules (analyte) can permeate the active semiconductor layer through the grain boundaries where the molecules can adsorb, attach chemically or be trapped physically. Structural and chemical properties of the analyte molecules can greatly affect the conductivity in OFET device by acting as traps (trapping the charge carriers) for charge carriers or by contributing to the charge flow. The gas molecules essentially change the grain boundary potential

barrier for conduction and the trap densities, which directly influences the mobility and the threshold voltage. These changes in the OFET parameters can be recorded and calibrated as the measure of sensitivity for the analyte of interest[14].

To summarize OFETs have been very instrumental in developing the very useful area of sensor technology. In our research we have tried to develop some of the most sensitive sensing platforms and circuits using the OFET base for analytes like ammonia[28,29] and ethylene.

1.2.3 Section 2

Bio Interfaces

Part 1

Electronic biosensing is another area where OFETs are strongly considered. Electronic biosensing is used for determining concentrations of biomolecules. In some cases, the presence of an analyte molecule induces a measured change in current flow, while in other cases; a new potential difference is established. In the particular case of a field effect biosensor, the potential difference is monitored as a change in conductance elsewhere in the device, such as across a film of an underlying semiconductor[30]. In OFET based biosensors the molecule interacts with the conductive channel via a protective barrier layer. It can be thought of as a second gate structure where the analyte molecule provides the second gate field and the barrier acts as the dielectric layer through which the field interacts with the active semiconducting layer.

We designed an OFET-based biosensor with a new receptor–antibody-

functionalized top dielectric layer. This layer, incorporating both a fluorinated polymer and vapor-deposited hydrocarbon, provided maximum capacitive coupling and minimal interference from the aqueous analyte solution, and allowed convenient solvent processing of the antibody-coupling layer. Using glial fibrillary acidic protein (GFAP) as a model protein analyte, this sensor platform demonstrated significant selectivity and recognition of target protein even in much more concentrated non-target protein backgrounds[31].

Part 2

Supramolecular chemistry has emerged as a promising way to rationally engineer the order of π-conjugated molecules that comprise OFETs through bottom-up assembly without utilizing expensive processing techniques such as lithography[32]. Biopolymers such as DNA[33], RNA[34] and polypeptides[35–42] or other biological scaffolds such as carbohydrates[43] and steroids[44] have been widely used as self-assembling systems for different applications including the construction of semiconducting and optoelectronic nanostructures. Specifically, peptide-based self-assembling systems derived from natural amino acids are considered as superior building blocks for structured materials because of the ease of synthesis via standard solid phase peptide synthesis and the wide variety of side chains that can be used to alter the molecular properties of each monomer[45].

More interestingly, various oligopeptides have been attached to π-conjugated components in order to form one-dimensional (1D) nanostructures with remarkable photophysical and electronic properties that show promise for

functional materials. Groups have either terminally attached the conductive π-functional unit(s) or embedded π-units within oligopeptide moieties. Among the advantages of this platform for organizing π-conjugated oligomers are the controlled assembly of heterogeneous mixtures of donor and acceptor containing materials[46–48] or addition of active groups for further functionality[49]. However, this limits the charge transport properties of the material because of the increased ratio of "insulating" peptide moieties, thus making it challenging to build electronic devices and directly characterize conductivity[43–51]. Related to this, attaching semiconducting units to self-assembling amide substituents that result in organogel formation have been reported to increase charge mobilities upon incorporation in OFETs[52–54]. Several examples of π-units such as oligothiophenes[55–57], oligophenylene- and oligothiophene-vinylenes[39,56–58], naphthalene/perylene diimides[36,59], tetrathiafulvalenes[48], hexabenzocoronenes[60], porphyrins[52,61,62], and poly(diacetylene)s[49] attached to peptide/amide self-assembling moieties have shown 1D-nanostructure formation and/or gel formation in aqueous and organic environments.

One distinct advantage of these self-assembled molecules is their compatibility with biological environments, making it possible to use these materials as self-assembled scaffold materials to support cells and to signal cells for differentiation or proliferation.

For our research we have functionalized self-assembling peptide molecules electrically in order to stimulate stem cells. A detailed study is conducted to rationally control the physical and electrical characteristics by controlling the amino

acid sequence to give us a library to chose from and custom design the specific molecules according to experimental conditions[63].

References

1. Arns, R. G. The other transistor: early history of the metal-oxide semiconductor field-effect transistor. *Eng. Sci. Educ. J.* **7,** 233–240 (1998).
2. Brunetti, F. G., Kumar, R. & Wudl, F. Organic electronics from perylene to organic photovoltaics: painting a brief history with a broad brush. *J. Mater. Chem.* **20,** 2934–2948 (2010).
3. Hideo, Akamatu, Hiroo, Inokuchi, Yoshio, M. Electrical Conductivity of the Perylene–Bromine Complex. *Nature* **173,** 168–169 (1954).
4. Volmer, M. Die verschiedenen lichtelektrischen Erscheinungen am Anthracen, ihre Beziehungen zueinander, zur Fluoreszenz und Dianthracenbildung. *Ann. Phys.* **345,** 775–796 (1913).
5. Koenigsberger, J. & Schilling, K. Über Elektrizitätsleitung in festen Elementen und Verbindungen. I. Minima des Widerstandes, Prüfung auf Elektronenleitung, Anwendung der Dissoziationsformeln. *Ann. Phys.* **337,** 179–230 (1910).
6. Pocchetino, A. Sul comportamento foto-electro dell' antracene. *Acad. Naz. Lincei Rendic* **15,** 355–368 (1906).
7. Okamoto, Y. *Organic Semiconductors*. (New York, Reinhold Pub. Corp, 1964).
8. Bonfiglioli, G. Recombination radiation in anthracene crystals. *Phys. Rev. Lett.* **14,** 229–232 (1965).
9. Brütting, W. *Physics of Organic semiconductors*. (Wiley-VCH, 2005).
10. Chiang, C. K. *et al.* Electrical conductivity in doped polyacetylene. *Phys. Rev. Lett.* **39,** 1098–1101 (1977).

11. Tang, C. W. Two-layer organic photovoltaic cell. *Appl. Phys. Lett.* **48,** 183–185 (1986).

12. Koezuka, H. Field-effect transistor with polythiophene thin film. *Synth. Met.* **18,** 699–704 (1987).

13. Coropceanu, V. *et al.* Charge transport in organic semiconductors. *Chem. Rev.* **107,** 926–952 (2007).

14. Bao, Zhenan, Locklin, J. J. *Organic Field-effect Transistors*. (CRC Press, 2007).

15. Fukuda, K., Takeda, Y., Mizukami, M., Kumaki, D. & Tokito, S. Fully solution-processed flexible organic thin film transistor arrays with high mobility and exceptional uniformity. *Sci. Rep.* **4,** 1–8 (2014).

16. Jiang, W., Li, Y. & Wang, Z. Heteroarenes as high performance organic semiconductors. *Chem. Soc. Rev.* **42,** 6113–6127 (2013).

17. Kola, S., Sinha, J. & Katz, H. E. Organic transistors in the new decade: Toward n-channel, printed, and stabilized devices. *J. Polym. Sci. Part B Polym. Phys.* **50,** 1090–1120 (2012).

18. Braga, D. & Horowitz, G. High-Performance Organic Field-Effect Transistors. *Adv. Mater.* **21,** 1473–1486 (2009).

19. Kaltenbrunner, M. *et al.* An ultra-lightweight design for imperceptible plastic electronics. *Nature* **499,** 458–465 (2013).

20. H., K. & Huang, J. Thin-Films Organic Electronic Devices. *Annu. Rev. Mater. Res.* 71–92 (2009). doi:10.1146/annurev-matsci-082908-145433

21. Himmelberger, Scott, Vandewal, Koen, Fei, Zhuping, Heeney, Martin, Salleo, A. Role of Molecular Weight Distribution on Charge Transport in

Semiconducting Polymers. *Macromolecules* **47,** 7151–7157 (2014).

22. Generali, G. *et al.* Correlation among morphology, crystallinity, and charge mobility in OFETs made of quaterthiophene alkyl derivatives on a transparent substrate platform. *J. Phys. Chem. C* **115,** 23164–23169 (2011).

23. Wong, L. Y. *et al.* Interplay of processing, morphological order, and charge-carrier mobility in polythiophene thin films deposited by different methods: Comparison of spin-cast, drop-cast, and inkjet-printed films. *Langmuir* **26,** 15494–15507 (2010).

24. Kline, R. J. *et al.* Dependence of regioregular poly(3-hexylthiophene) film morphology and field-effect mobility on molecular weight. *Macromolecules* **38,** 3312–3319 (2005).

25. Fei, Z. *et al.* Influence of side-chain regiochemistry on the transistor performance of high-mobility, all-donor polymers. *J. Am. Chem. Soc.* **136,** 15154–15157 (2014).

26. Kwiatkowski, J. J., Frost, J. M. & Nelson, J. The effect of morphology on electron field-effect mobility in disordered C60 thin films. *Nano Lett.* **9,** 1085–1090 (2009).

27. Noriega, R. *et al.* A general relationship between disorder, aggregation and charge transport in conjugated polymers. *Nat. Mater.* **12,** 1038–1044 (2013).

28. Huang, W. *et al.* Highly sensitive NH3 detection based on organic field-effect transistors with tris(pentafluorophenyl)borane as receptor. *J. Am. Chem. Soc.* **134,** 14650–14653 (2012).

29. Besar, K. *et al.* Printable ammonia sensor based on organic field effect

transistor. *Org. Electron.* **15,** 3221–3230 (2014).

30. Huang, W., Diallo, A. K., Dailey, J. L., Besar, K. & Katz, H. E. Electrochemical processes and mechanistic aspects of field-effect sensors for biomolecules. *J. Mater. Chem. C* **3,** 6445–6470 (2015).

31. Huang, W. *et al.* Label-free brain injury biomarker detection based on highly sensitive large area organic thin film transistor with hybrid coupling layer. *Chem. Sci.* **5,** 416–426 (2014).

32. Gasperini, a., Bivaud, S. & Sivula, K. Controlling conjugated polymer morphology and charge carrier transport with a flexible-linker approach. *Chem. Sci.* **5,** 4922–4927 (2014).

33. Seeman, N. C. DNA in a material world. *Nature* **421,** 427–431 (2003).

34. Chworos, A. *et al.* Building programmable jigsaw puzzles with RNA. *Science (80-.).* **306,** 2068–2072 (2004).

35. Reches, M. Casting Metal Nanowires Within Discrete Self-Assembled Peptide Nanotubes. *Science (80-.).* **300,** 625–627 (2003).

36. Ashkenasy, N., Horne, W. S. & Ghadiri, M. R. Design of self-assembling peptide nanotubes with delocalized electronic states. *Small* **2,** 99–102 (2006).

37. Diegelmann, S. R., Gorham, J. M. & Tovar, J. D. One-dimensional optoelectronic nanostructures derived from the aqueous self-assembly of π-conjugated oligopeptides. *J. Am. Chem. Soc.* **130,** 13840–13841 (2008).

38. Shao, H., Nguyen, T., Romano, N. C., Modarelli, D. A. & Parquette, J. R. Self-assembly of 1-D n-type nanostructures based on naphthalene diimide-appended dipeptides. *J. Am. Chem. Soc.* **131,** 16374–16376 (2009).

39. Matmour, R. & Cat, I. De. Oligo (p-phenylenevinylene)– Peptide Conjugates: Synthesis and Self-Assembly in Solution and at the Solid– Liquid Interface SI. *J. Am. Chem. Soc.* **130,** 14576–14583 (2008).

40. Jahnke, E., Lieberwirth, I., Severin, N., Rabe, J. P. & Frauenrath, H. Topochemical polymerization in supramolecular polymers of oligopeptide-functionalized diacetylenes. *Angew. Chemie - Int. Ed.* **45,** 5383–5386 (2006).

41. Gallaher, J. K., Aitken, E. J., Keyzers, R. A. & Hodgkiss, J. M. Controlled aggregation of peptide-substituted perylene-bisimides. *Chem. Commun.* **48,** 7961–7963 (2012).

42. Kim, S. H. & Parquette, J. R. A model for the controlled assembly of semiconductor peptides. *Nanoscale* **4,** 6940–6947 (2012).

43. Schmid, S., Mena-Osteritz, E., Kopyshev, A. & Bauerle, P. Self-assembling carbohydrate-functionalized oligothiophenes. *Org. Lett.* **11,** 5098–5101 (2009).

44. Kawano, S. I., Fujita, N. & Shinkai, S. Quater-, quinque-, and sexithiophene organogelators: Unique thermochromism and heating-free sol-gel phase transition. *Chem. - A Eur. J.* **11,** 4735–4742 (2005).

45. Cipriano, T. *et al.* Bioinspired peptide nanostructures for organic field-effect transistors. *ACS Appl. Mater. Interfaces* **6,** 21408–21415 (2014).

46. Ardoña, H. A. M. & Tovar, J. D. Energy transfer within responsive pi-conjugated coassembled peptide-based nanostructures in aqueous environments. *Chem. Sci.* **6,** 1474–1484 (2015).

47. Channon, K. J., Devlin, G. L. & MacPhee, C. E. Efficient energy transfer within

self-assembling peptide fibers: A route to light-harvesting nanomaterials. *J. Am. Chem. Soc.* **131,** 12520–12521 (2009).

48. Nalluri, S. K. M. & Ulijn, R. V. Discovery of energy transfer nanostructures using gelation-driven dynamic combinatorial libraries. *Chem. Sci.* **4,** 3699–3705 (2013).

49. Diegelmann, S. R., Hartman, N., Markovic, N. & Tovar, J. D. Synthesis and alignment of discrete polydiacetylene-peptide nanostructures. *J. Am. Chem. Soc.* **134,** 2028–2031 (2012).

50. Kumar, R. J., MacDonald, J. M., Singh, T. B., Waddington, L. J. & Holmes, A. B. Hierarchical self-assembly of semiconductor functionalized peptide a-helices and optoelectronic properties. *J. Am. Chem. Soc.* **133,** 8564–8573 (2011).

51. Sun, Y. *et al.* Semiconductive, one-dimensional, self-assembled nanostructures based on oligopeptides with π-conjugated segments. *Chem. - A Eur. J.* **17,** 4746–4749 (2011).

52. Umezawa, N., Matsumoto, N., Iwama, S., Kato, N. & Higuchi, T. Facile synthesis of peptide-porphyrin conjugates: Towards artificial catalase. *Bioorganic Med. Chem.* **18,** 6340–6350 (2010).

53. Jurchescu, O. D. *et al.* Correlation between microstructure, electronic properties and flicker noise in organic thin film transistors. *Appl. Phys. Lett.* **92,** (2008).

54. Prasanthkumar, S., Gopal, A. & Ajayaghosh, A. Self-assembly of thienylenevinylene molecular wires to semiconducting gels with doped metallic conductivity. *J. Am. Chem. Soc.* **132,** 13206–13207 (2010).

55. Schillinger, E. K., Mena-Osteritz, E., Hentschel, J., Borner, H. G. & Bauerle, P. Oligothiophene versus b-sheet peptide: synthesis and self-assembly of an organic semiconductor-peptide hybrid. *Adv. Mater.* **21,** 1562–1567 (2009).

56. Janssen, P. G. a *et al.* ssPNA templated assembly of oligo(p-phenylenevinylene)s. *Chem. Commun. (Camb).* **46,** 109–111 (2010).

57. Mba, M. *et al.* Synthesis and self-assembly of oligo(p-phenylenevinylene) peptide conjugates in water. *Chem. - A Eur. J.* **17,** 2044–2047 (2011).

58. Wall, B. D. *et al.* Variation of Formal Hydrogen-Bonding Networks within Electronically Delocalized π - Conjugated Oligopeptide Nanostructures. *Langmuir* **30,** 11375–11385 (2014).

59. Draper, E. R. *et al.* Air-stable photoconductive films formed from perylene bisimide gelators. *J. Mater. Chem. C* **2,** 5570–5575 (2014).

60. Yin, M., Shen, J., Pisula, W., Liang, M. & Zhi, L. Functionalization of Self-Assembled Hexa- peri -hexabenzocoronene Fibers with Peptides for Bioprobing. *J. Am. Chem. Soc* **131,** 14618–14619 (2009).

61. Giuntini, F., Alonso, C. M. a & Boyle, R. W. Synthetic approaches for the conjugation of porphyrins and related macrocycles to peptides and proteins. *Photochem. Photobiol. Sci.* **10,** 759–791 (2011).

62. Sol, V., Chaleix, V., Granet, R. & Krausz, P. An efficient route to dimeric porphyrin-RGD peptide conjugates via olefin metathesis. *Tetrahedron* **64,** 364–371 (2008).

63. Besar, Kalpana, Ardona, Herdeline Ann, Tovar, John D., Katz, H. E. Demonstration of Hole Transport and Voltage Equilibration in Self-

Assembled π - Conjugated Peptide. **9,** 12401–12409 (2015).

Section 1

Chapter 2

Ammonia Sensor

Ammonia sensing is of intense interest due to its potential association with chronic diseases like asthma, severe respiratory inflammations, and lung diseases arising from its presence as an environmental pollutant[1,2]. (see also https://www.sciencemag.org/content/343/6168/238.full, accessed 21 January 2014]. Currently the exposure limit for ammonia is effectively dictated by the ammonia sensing capabilities of available technologies rather than any detailed study on the effects of lower environmental ammonia concentrations that could be present.

Ammonia sensors with limits of detection ranging from as high as 200 ppm down to 0.35 ppm have been reported in the last decade, based on technologies such as metal-oxides, catalytic processes, organic polymer films, optical detection techniques and mass spectrometry coupled with gas chromatography (GC–MS)[3–7]. Organic field effect transistor (OFET) sensors are proposed for gas sensing as all the other mentioned techniques are either very expensive, bulky with high temperature requirements, lack high selectivity or have a limit of detection too high for non-occupational settings. OFET can provide potential high sensitivity, low cost, low weight and potential to make flexible[8], large area devices.

Many attempts have been made to improve the sensitivity; selectivity and stability of OFET based ammonia sensors. Wei *et al*. developed single-crystalline

micro/nanostructures of perylenediimide derivatives with a fast response rate, high ammonia sensitivity (1%) and long term stability[9]; Parra *et al*. reported molecular semiconductor-doped insulator heterojunction transducers which can detect "<200 ppm" ammonia vapor[10]; later, Bouvet and coworkers developed a novel semiconducting molecular material, $Eu_2[Pc(15C5)_4]_2[Pc(OC10H21)_8]$ as a quasi-Langmuir-Shäfer (QLS) film for use as a top-layer, and vacuum-deposited and cast film of CuPc as well as copper tetra-tert-butyl phthalocyanine (CuTTBPc) QLS film as sub-layers, achieving ammonia sensitivity in the range of 15-800 ppm[11]; Zan *et al.* developed a novel hybrid gas sensor based on amorphous indium gallium zinc oxide thin-film transistors, which can respond to "0.1 ppm" ammonia[12]. This latter detection limit is placed in quotes because in these experiments, the ppm concentration of ammonia gas in the chamber was expressed as mg per liter of chamber volume, which is *1329 times higher* than a more appropriate ppm definition for gas mixtures (μL/L).

Recently, X. Yu et.al reported flexible ammonia (NH_3) gas sensors based on solution-processable OFETs using TIPS-pentacene as active layer with a Poly(methyl methacrylate) (PMMA) dielectric layer on glass and plastic substrates[6] . The reported device is very low cost and printable, but as the sensor design is based on the morphology of the TIPS-pentacene film rather than chemical design, the highest sensitivity of these devices is only 10 ppm; though the high reversibility and stability were advantageous. Huang *et al.* also reported a printable pentacene based OFET ammonia senor with poly(vinyl alcohol), poly(4-vinylphenol), poly(methyl methacrylate) and polystyrene dielectric layers which affected the grain size and

morphology of the pentacene; the reported limit of detection was 1 ppm [5]. Tiwari *et al.* developed a poly-3-hexylthiophene based organic field-effect transistor ammonia sensor with detection ranging between 0.1-25 ppm, the ppm definition used in this work was 1mg ammonia/L, a thousand times more concentrated than 1 ppm v/v[7].

Along with sensitivity, selectivity is another crucial part of any sensor study, which can be a challenge for a device depending solely on morphological features, although this kind of dependence is very helpful for reversibility of the response. Li *et al.* developed a novel dendritic microstripe-based dialkyl tetrathiapentacene (DTBDT-C6) OFET ammonia sensor using a dip coating process to avoid the drawbacks of solution-processed films. The proposed device combines the two useful features of selectivity and reversibility, but could only detect 10 ppm of ammonia [4].

Thus although OFET based ammonia sensors technology have seen major advances and have shown great potential but detection of trace amount of ammonia by organic field effect transistors (sub ppm v/v) is still challenging.

2.1 Vapor Deposited Ammonia Sensor

2.1.1 Introduction

As a high level of sensitivity is one of the major challenges for ammonia sensing, we devised a unique scheme to increase the organic field-effect transistor (OFET) NH_3 response by using tris-(pentafluorophenyl)borane (TPFB) as receptor.

Boranes have frequently acted as complexation agent for Lewis bases[13,14] due to the strong interaction between boron atoms and lone pairs; furthermore, borane-amine complexes have also been widely used as light-emitting molecules[15] and in

fluorescent sensors[16]. TPFB is frequently used as a strongly Lewis acidic co-catalyst in numerous kinds of reactions, such as dehydration[17], Friedel-Crafts reactions, ring-opening reactions[18], and syndiospecific living polymerization[19]. Here, TPFB was chosen as the NH_3 receptor additive to the OFET semiconductors due to the strong interaction between boron atoms and nitrogen atoms[20] and its known sublimability under vacuum. Furthermore, the hydrogen bonds formed between hydrogen atoms and fluorine atoms also play a role in the complexation process, so the NH_3 molecule is tightly bound to TPFB through all its four hydrogen atoms (Figure 4).

OFETs with this additive detect concentrations of 450 ppb v/v, with a limit of detection of 350; in comparison, when triphenylmethane (TPM) was used as an additive, no obvious improvement of sensitivity was observed. These OFETs also showed considerable selectivity with respect to common organic vapors, and stability to storage. Furthermore, excellent memory of exposure was achieved by keeping the exposed devices in a sealed container stored at −30°C, the first such capability demonstrated with OFETs.

Experimental

2.1.2 Materials Used

Tris-(pentaflourophenyl)borane has been used as a complexing agent for ammonia. We used two semiconductors for OFET fabrication, copper phthalocyanine (CuPc) and cobalt phthalocyanine (CoPc). As a TPFB control, triphenylmethane (TPM) was used as an alternative additive due to its similar molecular shape with TPFB. Highly n-doped <100> silicon wafers with 300 nm thermally grown oxide were used as the

substrate for OFET. Gold was used to deposit the source and the drain electrodes. All materials were purchased from Sigma-Aldrich unless synthesized or otherwise denoted.

2.1.3 Device Fabrication

All OFETs were fabricated and characterized using standard methods. Highly n-doped <100> silicon wafers with 300 nm thermally grown oxide were diced into 1 inch by 1 inch substrates. The wafers were cleaned with piranha solution, sonicated in acetone and isopropanol, and then dried by forced nitrogen gas. Substrates were dried more thoroughly via 100°C vacuum annealing for 20 min prior to a 2-hour exposure to hexamethyldisilazane (HMDS) vapor at 100°C in a loosely sealed vessel. Organic semiconductors (OSCs, CuPc and CoPc) were thermally evaporated neatly or co-evaporated with TPFB or TPM directly onto HMDS treated substrates with a thickness of 6 nm at a rate of 0.3 Å/s for the OSCs, while the deposition rate of additive was 0.2 Å/s. Gold electrodes (50 nm) were then thermally vapor-deposited through a shadow mask (width/length (W/L) 32) at a rate of 0.3 Å/s. The pressure of the deposition chamber was $<5\times10^{-6}$ torr, and substrate temperature during the deposition was held constant at 25°C.

All the OFETs were measured using an Agilent 4155C semiconductor analyzer. Ammonia gas with a defined dilution (4.5 ppm in nitrogen) was purchased from PRAXAIR; 0.45 ppm ammonia concentration was achieved by mixing 4.5 ppm ammonia from a tank with pure nitrogen. A home-built, well-sealed exposure chamber with a volume of 4 liters was used, with a rotating fan inside to create a

uniform vapor concentration; the flow rate of gas through the chamber was 0.2 liter per minute.

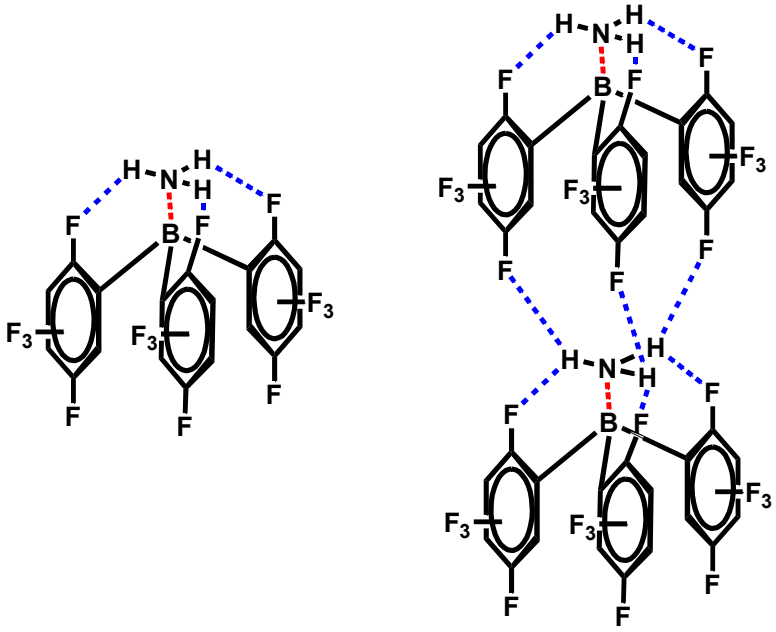

Figure 4 The host-guest interaction between ammonia and tris-(pentflurophenyl)borane.

2.1.4 Results and Discussion

The typical OFET transfer and output curves of CuPc and CoPc with and without additives are shown in Figure 5 (V_{ds} = -60 V). Mobilities, threshold voltages and on-off current ratios of these transistors are summarized in Table 1 Mobilities, threshold voltages and on-off current ratios of different transistors.. OFETs with TPFB as additive show lower mobility and require higher gate voltage to turn on than the other OFETs. One possible reason for this may be that the TPFB molecule contains many more locally dipolar bonds than TPM, which makes it more likely for TPFB to trap holes in the channel, thus giving a lower mobility and more negative threshold voltage.

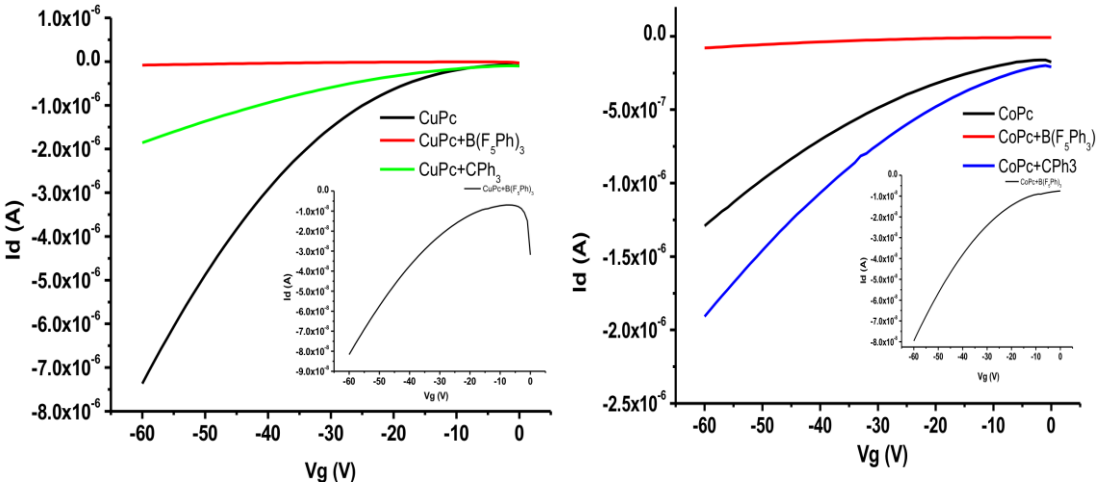

Figure 5 Typical organic field effect transistor transfer curves of CuPc and CoPc with and without additive (V_{ds}=-60 V).

Semiconductor	**μ ($cm^2 V^{-1}S^{-1}$)**	**V_{th} (V)**	**On/Off**
CuPc	5×10^{-3} to 1.3×10^{-2}	0	100
CuPc&B(F_5Ph)$_3$	7.8×10^{-5} to 2.3×10^{-4}	-4 to -8	10
CuPc&CPh_3	4.0×10^{-3} to 6.4×10^{-3}	0 to -1	10
CoPc	1.9×10^{-3} to 2.3×10^{-3}	0 to -3	10
CoPc&B(F_5Ph)$_3$	5.0×10^{-5} to 1.5×10^{-4}	-2 to -6	10
CoPc&CPh_3	3.0×10^{-3} to 5.0×10^{-3}	-1 to -2	10

Table 1 Mobilities, threshold voltages and on-off current ratios of different transistors.

The response of these devices to ammonia vapor were investigated by plotting the percent change in drain current, $100\% \times (I_{d,0} - I_d)/I_{d,0}$ (measured at V_g = −60 V, V_{ds} = −60 V) with respect to time of exposure to ammonia vapor. For some p-type

semiconductors, such as CuPc, CoPc, 6PTTP6, and pentacene[21–23], the OFET current is known to be higher in dry air due to oxygen doping than in nitrogen, the carrier gas used for ammonia. In order to get accurate responses to ammonia, all the devices were subjected to ambient aging for 3 days before ammonia exposure experiments. All the responses shown in the following figures are the value after correcting for the current decrease caused by replacing oxygen with nitrogen.

As shown in Figure 6, after exposure to 4.5ppm ammonia vapor for 30 minutes, the drain current of CuPc, CuPc+TPM decreased 13% and 12% respectively. For CuPc+TPFB, the decrease in drain current was 33%, which is much higher than the responses of CuPc and CuPc+TPM. For CoPc and CoPc+TMP (Figure 7), the decrease was 11% and 15% respectively, and for CoPc+TPFB, the decrease was 37%, which is also much higher than for CoPc and CoPc+TPM. This larger decrease is consistent with the strong interaction between TPFB and ammonia vapor increasing the binding of ammonia to the semiconductor surface, thus give a much higher relative response. While triphenylmethane has a similar molecular structure as tris(pentafluorophenyl)borane, it has no host-guest interaction with ammonia, and the enhancement in relative response was not obtained. After 90 minutes of exposure, the decrease in drain current of CuPc, CuPc+TPM and CuPc+TPFB were 24%, 15%, 41% respectively. For CoPc, CoPc+TPM and CoPc+TPM, the decreases were 16%, 22%, 44%, respectively. After 260 minutes of exposure, the drain current of CuPc, CuPc+TPM and CuPc+TPFB decreased by 38%, 25% and 51% respectively. For CoPc, CoPc+TPM and CoPc+TPFB the drain current decreased by 24%, 31%, 63% respectively. Over time, the rate of drain current decrease became lower.

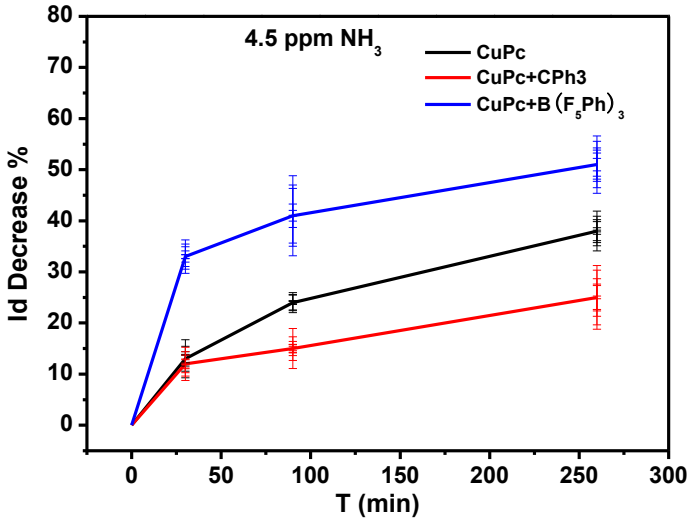

Figure 6 Drain current decrease of CuPc, CuPc+TPM and CuPc+TPFB devices vs time of exposure to 4.5 ppm ammonia.

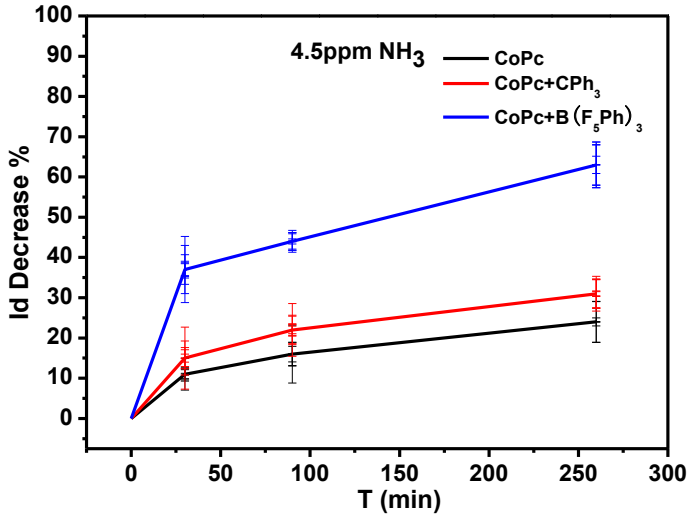

Figure 7 Drain current decrease of CoPc, CoPc+TPM and CoPc+TPFB devices vs time of exposure to 4.5 ppm ammonia.

In second set of experiments, CuPc+TPFB and CoPc+TPFB were exposed to a much lower ammonia concentration (0.45 ppm in nitrogen), and the results are shown in Figure 8 and Figure 9.

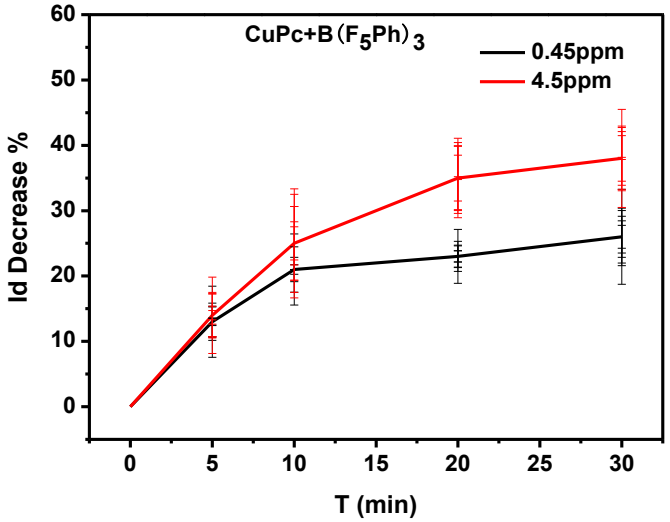

Figure 8 Drain current decrease of CuPc+TPFB devices vs time of exposure to 4.5 ppm and 0.45 ppm ammonia.

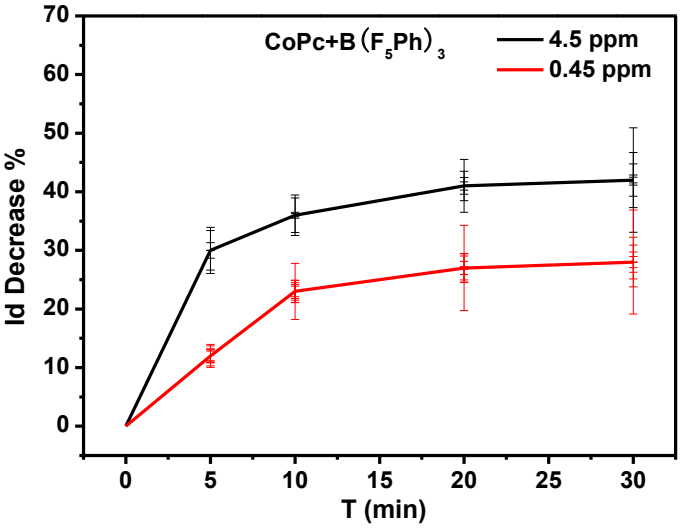

Figure 9 Drain current decrease of CoPc+TPFB devices vs time of exposure to 4.5 ppm and 0.45 ppm ammonia vapor

After 5 minutes exposure, the drain current of CuPc+TPFB and CoPc+TPFB decreased by 13% and 12% respectively, while after 10 minutes, the drain current decreased by 21% and 23%; after 20 and 30 minutes exposure, the drain current of CuPc+TPFB and CoPc+TPFB decreased by 23%, 26% and 27%, 28% respectively. In

comparison, responses of CuPc+TPFB and CoPc+TPFB to 4.5 ppm ammonia after 5, 10, 20, and 30 minutes are also shown in Figure 8 and Figure 9.

The selectivity of these devices was also investigated. Figure 10 displays the drain current change of CuPc+TPFB and CoPc+TPFB after exposure to different gas vapors Methanol, acetone, and ethyl acetate were chosen because of the possibility of oxygen interactions with TPFB involving the O and B atoms[24]. Dichloromethane is a highly volatile solvent that may exist under some circumstances at high concentration, so it was also desirable to check this vapor. As shown in Figure 10, all these solvents gave only small responses even at very high concentrations (several thousand ppm). Thus, TPFB is more sensitive and efficient in detecting NH_3 vapors than organic amine vapors. These devices also showed good stability to moisture, with I_d remaining above 50% of its original value even after 7 days of exposure to <30% relative humidity (RH) at 25 °C; only when the RH was higher than 50% did the devices show relatively fast linear decay. Water is filterable from NH_3 using a highly basic desiccant.

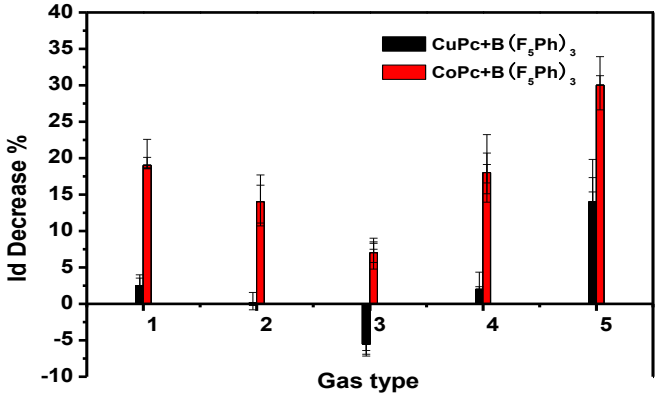

Figure 10 Drain current change of CuPc+B(F5Ph)3 and CoPc+B(F5Ph)3 devices in diffrent gas vapor for 5 minutes; 1, methanol (163,000 ppm); 2, acetone (320,000 ppm); 3, dichloromethane (658,000 ppm); 4, ethyl acetate (125,000 ppm); 5, ammonia(4.5 ppm).

Retention of the electrical effect of the exposure is important if it is not practical to read the device immediately after exposure. This requires prevention of diffusion of the analyte out of the device or even within the device. We found that simply maintaining the exposed device in a small container (1 inch diameter fluoroware) was insufficient to keep the post-exposure current reading constant. However, further investigation showed that placing the exposed devices in a small container and storing at low temperature (-30°C), the signal only gives a very small change one day later.

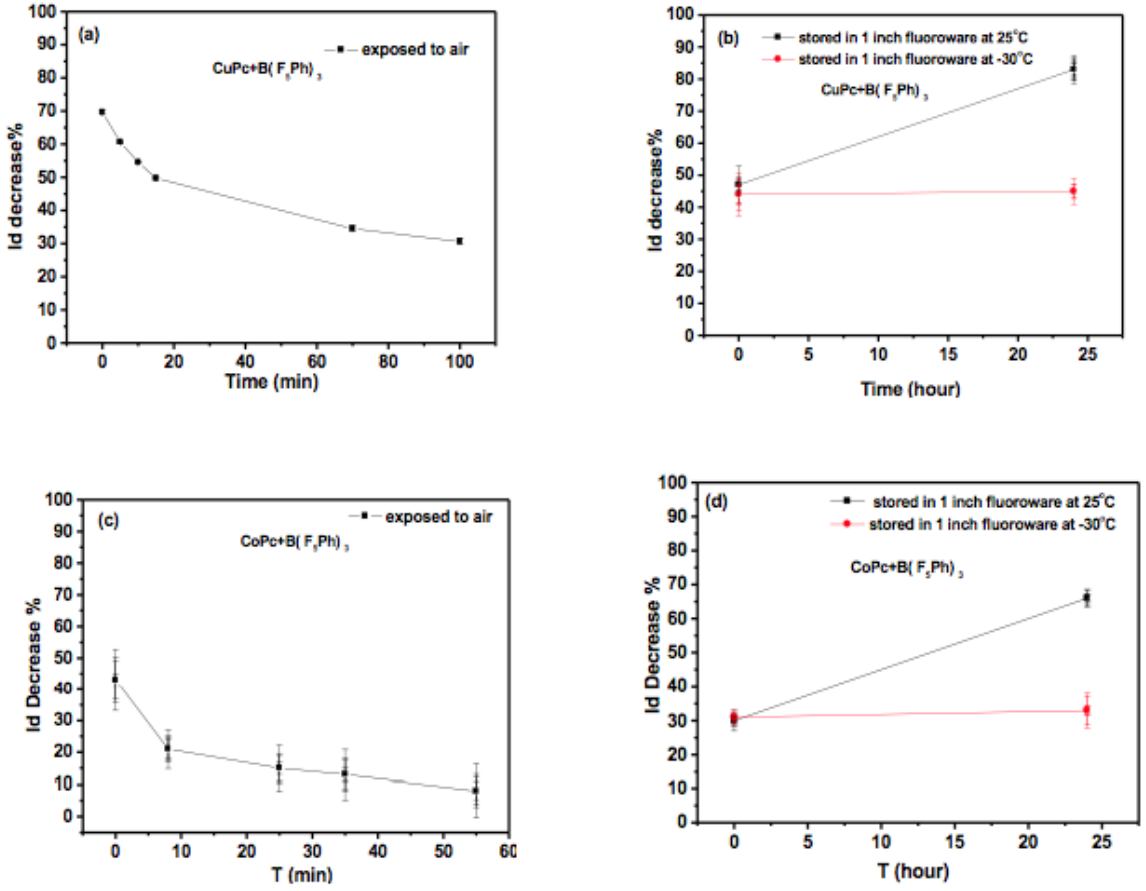

Figure 11 Drain current change of exposed devices under different storage conditions.

As shown in Figure 11, for CuPc+TPFB, an exposed device with a response of 70% drain current decrease gradually lost its response signal while stored in open air;

the device stored in small container at 25°C changed its signal drastically from 47% to 83% after 24 hours (perhaps because of ammonia diffusion within the device to more electronically active sites); however, for the device stored in a small container at -30°C, the signal only shows an insignificant change after 24 hours, from 44% to 45%. For CoPc+TPFB, the device stored in the open air also lost its signal and recover eventually; the device stored in the small container at 25 °C changed its signal drastically from 30% to 66% after 24 hours; while for the device stored in small container at -30°C, the signal shows a negligible change, from 31% to 33%. Numerous experiments show that the drift of the signal is less than 6% after one day stored in small container at -30°C

2.1.5 Conclusion

In conclusion, we have successfully developed a highly responsive ammonia detector using TPFB as a receptor. The specific host-guest interaction between ammonia and TPFB plays a critical role in enhancing the sensitivity of the sensor. Additionally, these OFETs also show excellent selectivity and stability. Device current changes were preserved by keeping the devices in a small container stored at -30°C To the best of our knowledge, this is the first report of using borane as a receptor in a sensitive organic field effect transistor.

Acknowledgements

We are grateful to the JHSPH Center for a Livable Future, the NIEHS Center in Urban Environmental Health (P30 ES 03819), and the Johns Hopkins Environment, Energy,

Sustainability, and Health Institute for support of this work.

We would also like to thank Weiguo Huang for insightful discussions and guidance throughout this project.

2.2 Printable Ammonia Sensor

2.2.1 Introduction

The detailed study required for designing personalized intervention strategies for the ammonia exposure in relation to human health and environmental monitoring not only calls for a highly sensitive sensing technique but also for cost effectiveness, high selectivity, light weight, compactness and mass production potential.

As reported in the previous section 2.1, we developed OFET-based ammonia sensors that could detect concentrations of 0.45ppm v/v, with a limit of detection of 0.35 v/v ppm, which is a very high sensitivity. These OFETs, however, were vapor-deposited, leading to long process time and high cost of production, making the sensor less feasible for mass-production.

To address these particular issues, we developed a printable OFET sensor with sensitivity of 0.5 ppm v/v for ammonia and a conservative limit of detection of 0.1 ppm, with a much more time and cost-efficient process than a vapor deposited structure. A key aspect of the process is corona charging of a polyethylene terephthalate (PET) substrate. PET, with a dielectric constant of 3.2, is a widely used dielectric material for charge storage applications (e.g. film capacitors). Numerous studies have been published on the nature of the charges on the PET surface due to corona charging [25–33]. Inherent static charges present on PET surfaces could be easily tailored by this technique or similar techniques like oxygen plasma to manipulate OFET characteristics, e.g. threshold voltage[34]. Taking advantage of

this technique, we have been able to use PET substrate as gate dielectric material and the static charges present on it as a static gate, thus significantly simplifying the OFET structure to that of a chemiresistor.

Experimental

2.2.2 Material

The schematic of the PET OFET fabrication process and the device structure are shown in **Error! Reference source not found.**. The modified OFET structure was developed on 12-μm thick PET sheets supplied by Mitsubishi polyester films. poly (3,3'''-didodecylquaterthiophene) (PQT-12) and 2,2'-[(2,5-dihexadecyl-3,6-dioxo-2,3,5,6-tetrahydropyrrolo[3,4-*c*]pyrrole-1,4-diylidene)dithiene-5,2-diylidene] dimalononitrile (DPP-CN) were synthesized in our laboratory. DPP-CN [35] was prepared according to modified literature procedures. For poly (3,3'''-didodecylquaterthiophene) (PQT-12) synthesis, 5,5'-bis(trimethylstannyl)-2,2'-bithiophene was purchased from Sigma-Aldrich and was further recrystallized for polymerization. 5,5'-Dibromo-4,4'-didodecyl-2,2'-bithiophene [36] was synthesized.

Synthesis of PQT12[37]

5,5'-Dibromo-4,4'-didodecyl-2,2'-bithiophene (0.5 mmol, 0.330 g), 5,5'-bis(trimethylstanny)-2,2'-bithiophene (0.5mmol, 0.246g), tris (dibenzylideneacetone)dipalladium(0) (0.02 mmol, 18.3 mg), and tri(o-tolyl)phosphine (0.08 mmol, 24.4 mg) were added to a reaction vial, which was then purged with argon for 15 min. Anhydrous chlorobenzene (15 mL) was added through a septum and the reaction mixture was then stirred at 115 °C for 72 h. The

reaction mixture was poured into methanol (150 mL) and HCl (10 mL). The polymer was filtered and subjected to Soxhlet extraction with acetone (24 h), hexane (24 h), dichloromethane (24 h) and chlorobenzene (24 h). The chlorobenzene fraction was concentrated and precipitated into methanol. Following filtration, the purified polymer (0.3 g, 90%) was obtained as a brown solid GPC: M_n = 20.5 kg/mol; M_w = 24.3 kg/mol; PDI = 1.2.

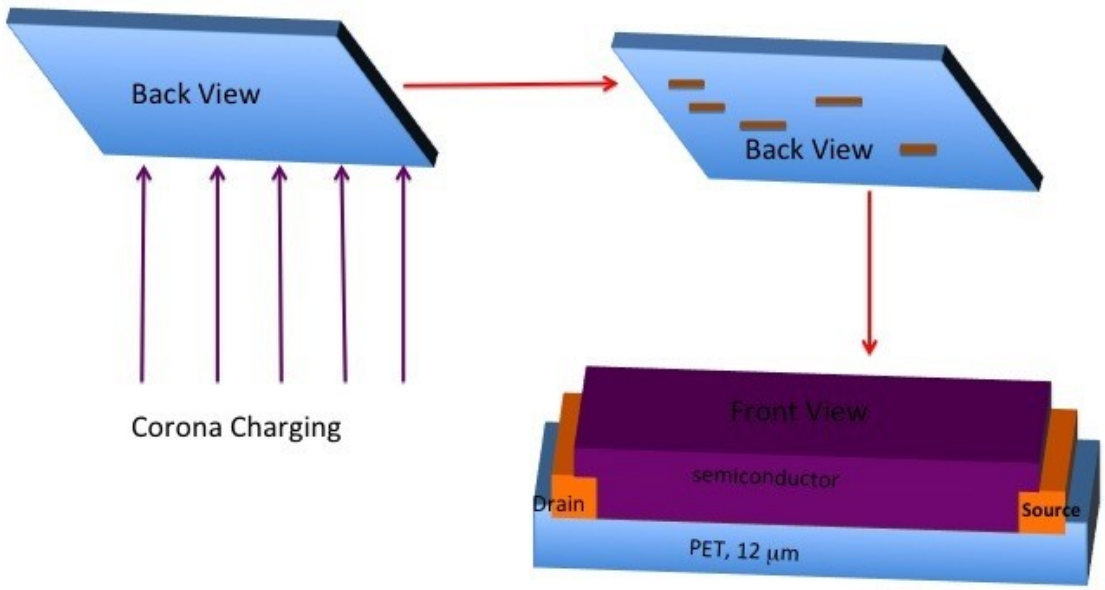

Figure 12 Schematic of device fabrication process

2.2.3 Device Preparation

The PET sheet was cut into 1 inch by 1 inch square samples. The samples were cleaned by keeping them in an ultrasonic bath for 10 minutes in isopropyl alcohol and then rinsed with distilled water. Following the cleaning process, samples were dried at ambient temperature and pressure. Semiconductor mobilities were measured and printed electrodes were initially characterized on Si/SiO_2 substrates with 300 nm of oxide.

Source-drain electrodes were made either of vapor-deposited gold (for initial tests of responsive plastic device materials) or silver ink processed via a pneumatic printing technique. Gold electrodes (50 nm thickness) were deposited by thermal vapor deposition using an interdigitated mask (channel width/length ratio approximately 308 (77000 μm /250 μm)) at 0.3 Å/s under 5×10^{-6} Pa. For printed silver electrodes on PET, the dispensing head is interfaced with a 3D stage, EFD dispensing system, and controlled by LabView for automated dispensing. The EFD system provides the back pressure before the dispensing step to allow suspension of the ink at the tip Figure 13. During dispensing, slight forward pressure is applied to allow the ink to contact the surface. The tip is then moved to draw the patterns while the ink continues to dispense by capillary action. The samples are baked at 110 ℃ for an hour after printing to allow the silver ink to cure. The printed silver source and drain with 100 μm and 300 μm channel length for the OFETs (W/L = 30) are shown in Figure 14.

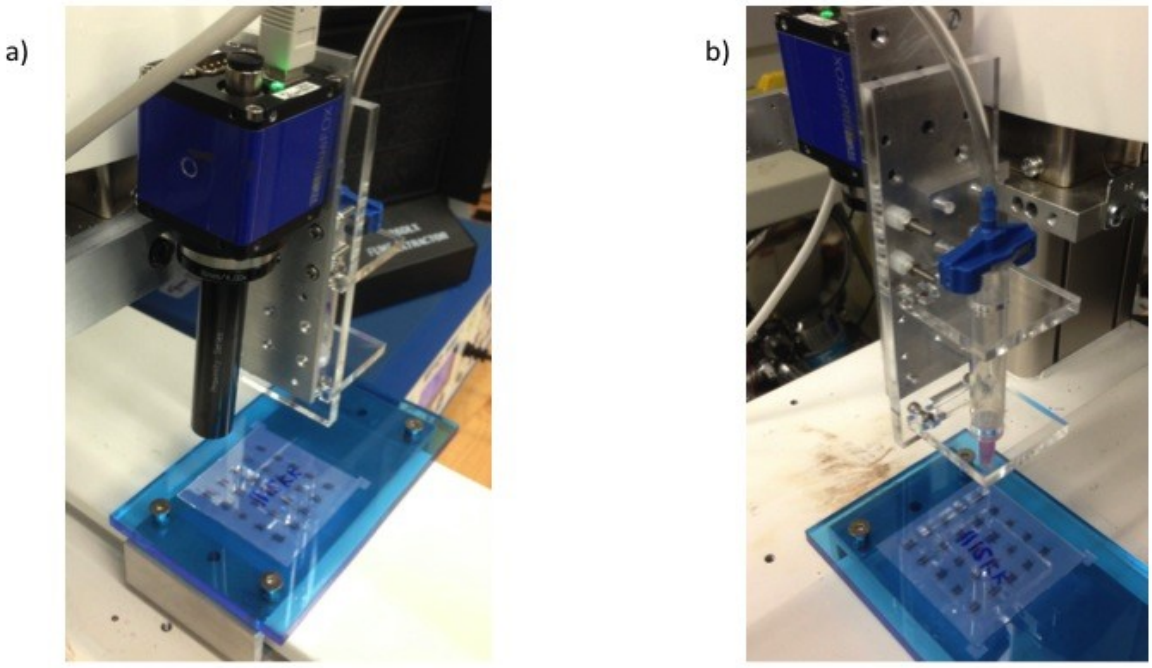

Figure 13 a) Bluefox camera interfaced with Labview for printing alignment, b) Pneumatic printing head interfaced with EDF.

For corona charging, PET substrates (with source-drain electrodes) were placed on the grounded metallic plate of the corona-charging set-up, with the free surface (back side, opposite to the source-drain electrodes) facing up to the needle electrode. In the corona discharge setup the needle electrode connects to a high (usually negative) DC voltage to create corona discharge for charging. There is a grid electrode interposed between the grounded plate and the needle electrode. This grid electrode connects to another (negative) DC potential and helps to create an almost uniform field of desired strength.

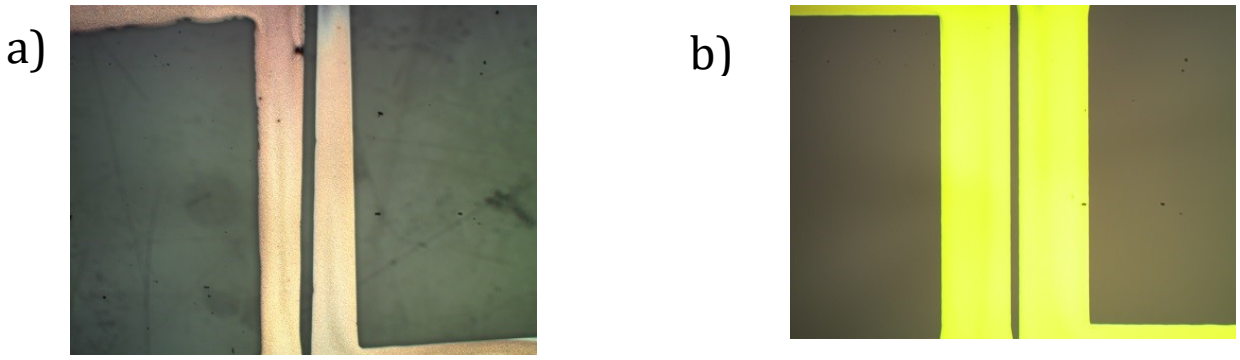

Figure 14 a) Printed source and drain on Si/SiO_2 with channel length 300 **µ**m b) Printed source and drain on PET with channel length 100 **µ**m.

We applied a -10,000 volts DC voltage at the needle electrode, which was modulated using the grid electrode to give a local voltage of -1500 V. The non-metallized side of the sample was charged in the corona discharge apparatus for 5-10 minutes.

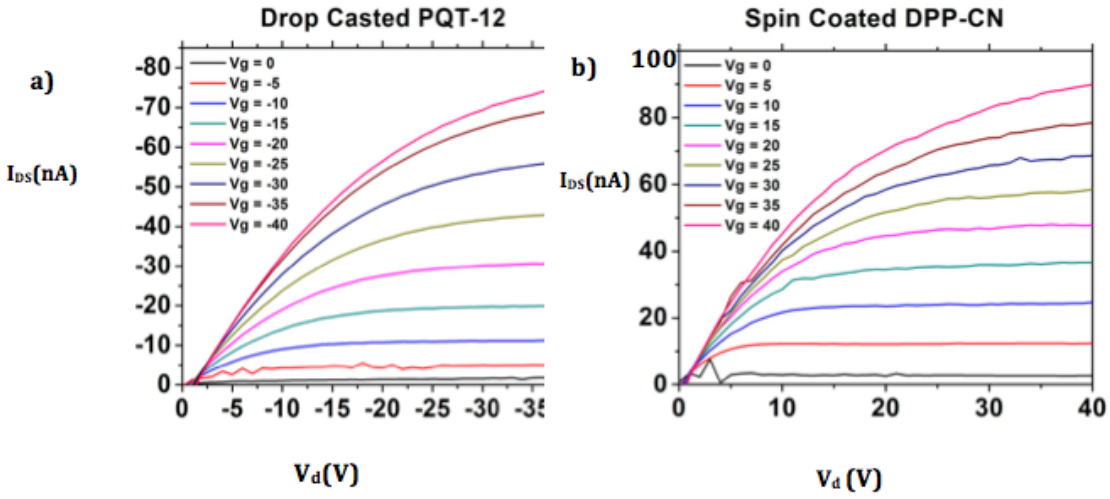

Figure 15 a) Output curve for silicon based PQT-12 OFET, b) Output curve for silicon based DPP-CN OFET.

PQT-12 and DPPCN were both used as 4 mg/ml solutions in cholorobenzene at 60°C, and were drop cast on the "front", source-drain electrode side of PET substrates following the corona charging process. Excess semiconductor solution was removed

from the device with absorbent wipes to minimize semiconductor film thickness. For baseline devices on Si substrates, PQT-12 films were drop cast while DPP-CN films were spincoated. The solvent was then allowed to evaporate at room temperature; no annealing was done. Output curves for these devices are shown in Figure 15.

2.2.4. Film Characterization and Sensor Test

All the OFET measurements were done using an Agilent 4155C semiconductor analyzer under ambient conditions. An NH_3 gas cylinder, concentration 5 ppm in nitrogen with blend tolerance +/- 10%, was purchased from Spec gas, Inc. An Enviromics gas dilution system (series 4040) was used to achieve an ammonia concentration of 0.5 ppm or lower by diluting 5 ppm ammonia with dry air. A sealed 1300 ml chamber with an outlet to allow continuous flow was used for ammonia exposure experiments; the flow rate of gas through the chamber was typically 1000 cm^3/min for 0.5 ppm exposure. For 1.5 ppm and 0.1 ppm the flow rate was 600 cm^3/min and 1500 cm^3/min, respectively according to the volume of dry air required to achieve different concentrations.

Responsive devices were tested at intervals of 5, 20, and 30 minutes in air to make sure of the initial stability of the devices to ambient conditions. Once a device stabilized in stationary air, it was put into a testing chamber with a plain air flow of 1000 cm^3/min to evaluate any effect of the increased air flow rate itself on device properties. For ammonia sensing experiments, devices were exposed to concentrations in the range of 0.1 to 1.5 ppm ammonia for 5 minutes or longer.

2.2.5 Results and Discussion

PET Device Charging

PET has been well studied for its charge storage applications and electret properties[25–28,30–34,38,39]. Electret effects and stability of surface potential in polymeric films have been largely attributed to hetero and homo charge formation due to polarization at low field and charge injection at higher fields during corona charging[29,30,40]. Although the most important factors for these effects are the field strength and time of exposure to the corona field, other factors like defects and sample geometry can also be important[40]. Temporal decay of the surface potential is a very crucial parameter for electret application and it has been related to processes such as surface conduction [41], atmospheric neutralization[40,42] sample polarization [43] and charge injection[25,40,44].

Inspired by the electret literature, plasma treatment using oxygen, UV and corona charging has been used to modulate threshold voltage of OFET's in several studies by modifying the density of states at the semiconductor-dielectric junctions. Chemical reaction between the charged plasma species and the dielectric surface can lead to trap states at the junction. Plasma treatment can introduce two types of charges, fixed and mobile. These charges are responsible for threshold voltage shift of the OFET due to the contribution to the field by the fixed charges and increase in conductivity due to mobile charges. The gate voltage does not modulate the mobile charges and hence this increase in conductivity is called parasitic conductivity [34].

We used corona-induced charge states in the bulk of a 12-micron thick sheet as the sole source of electric field instead of using interface trap states for threshold modulation. The implanted charges provide the field necessary to shift the threshold voltage so as to keep the device in accumulation mode. We found 12 microns to be the maximum thickness across which these charges were effective for our purposes. To optimize stability, grid voltage of -1500 V was chosen as charge decay has been reported to be slowest at -1500 V on PET surfaces [27].

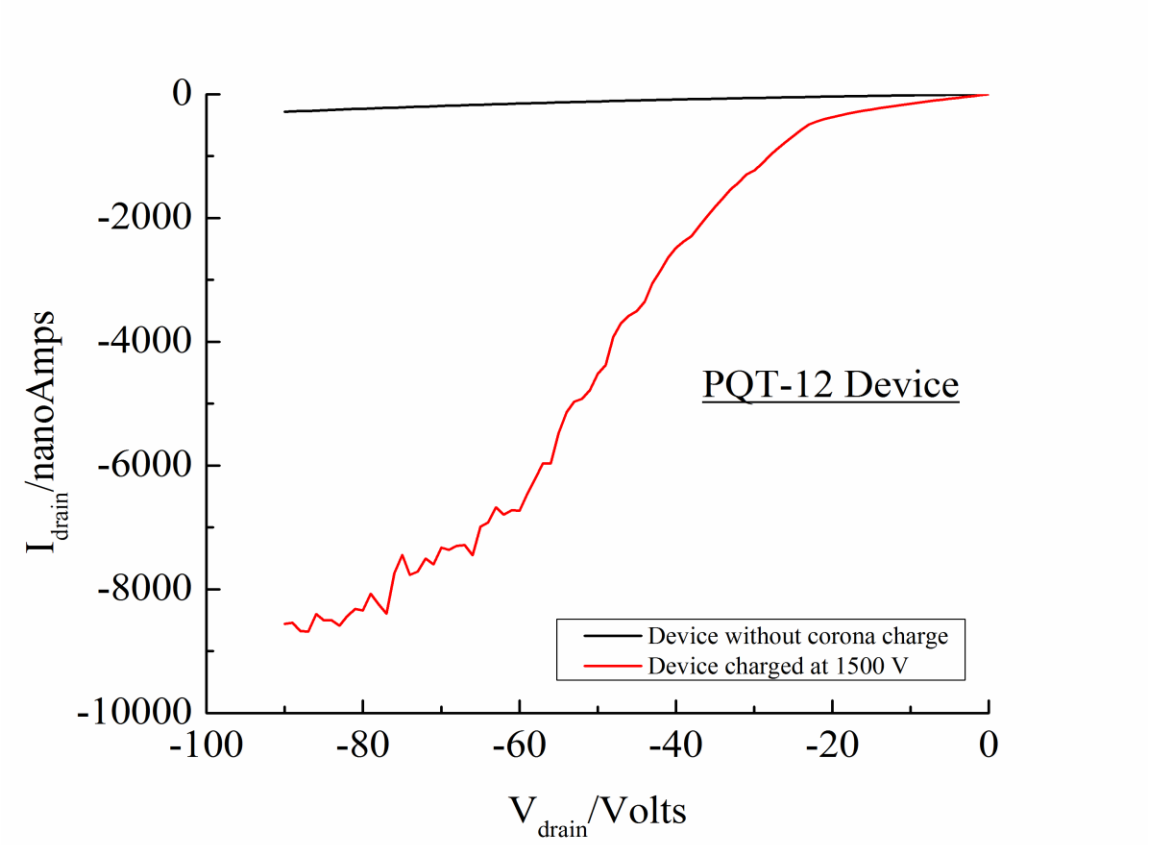

Figure 16 Output curve for a PQT-12 based device with static charges as gate.

Figure 16 shows I-V curves on PET substrates with static gate and gold electrodes, demonstrating the effect of corona charging in turning on the semiconductor by comparing charged and uncharged devices. For these experiments, electrodes were

vapor-deposited through a TEM grid with W/L=10). It can be clearly seen that corona induced trap states are the sole source of field effect in the PET based devices as the device without the corona treatment remains in the off state. It should be noted that conductivity of PQT-12 is low; hence high source-drain voltages are applied.

The magnitude of the drain current is notably high compared to typical silicon-based devices, because of the huge applied voltage (-1500 V) used to implant the charges (as compared to gate voltages and drain voltages applied in typical silicon devices (maximum +/-100 Volts)), the accumulation of the charges is enhanced leading to higher drain currents and little apparent "saturation" regime. Note that the implanting voltage level does not need to be applied during the operation of the device.

Surface charge densities for corona-induced charges were calculated using the linear regime FET equations

$$I_d = \mu C_{0x} \frac{W}{L} (V_{GS} - V_T) V_{ds}$$

And

$$C_{ox} \times \Delta V = \frac{Q}{A}$$

The calculation was done assuming that all the charges are on the interfaces of the device. Mobility was calculated using OFET structure with 200 nm PET as dielectric. The surface charge density calculated for different devices ranges between 2.4 ×

10^{12} to 9×10^{12} $\frac{\text{charges}}{\text{cm}^2}$. This is a typical range for OFET gate-induced charge densities.

Wang *et al.* and Dawidczyk *et al.* made similar observations using oxygen plasma and corona charging to manipulate the threshold voltage. In those cases, external gate voltage was used to turn on the device and the semiconductor-dielectric interface was exposed to the treatments that led to introduction of unwanted parasitic mobile charges, which could not be modulated, by gate field. In the present device, as the treatment is done on the bare side of PET, the mobile charges would need to travel through a 12 micron thickness of PET, which is less likely to happen. Our results agree with the theories presented in the preceding literature [34].

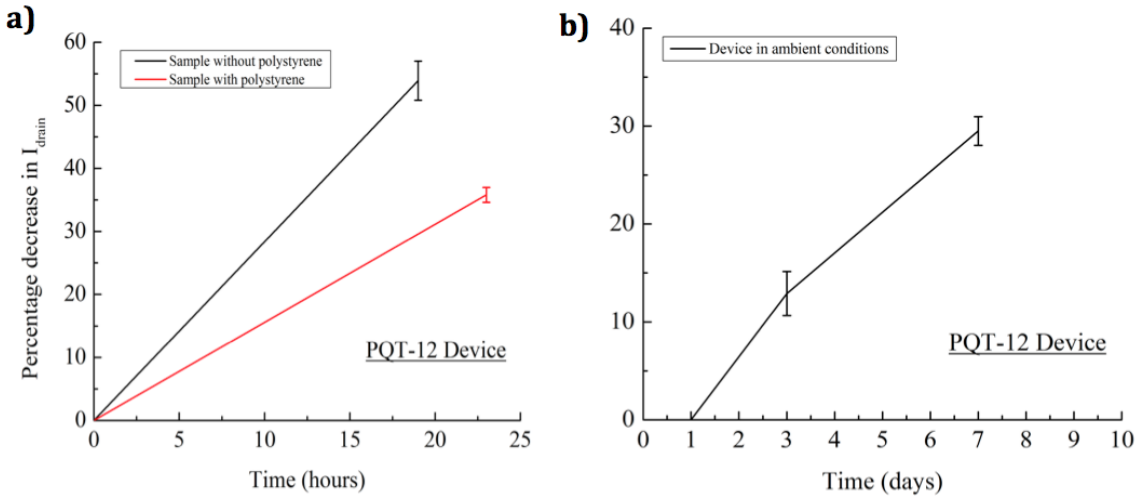

Figure 17 Demonstration of effect of additional polystyrene layer on the rate of charge desorption, average of 3 devices a) Stability increase due to polystyrene layer (24 hour ageing), time scale of hours b) with polystyrene layer, days timescale.

We anticipate the future need to stabilize the corona charged state. Major decay of the charges might be due desorption or migration with time, leading to instability of the device performance. To trap the charges or at least slow down the processes of

desorption, we spin-coated a very thin layer of polystyrene at 1000 rpm on the backside of the device after charging. Reports have shown that the charges can be stored better at the interface of two insulators [30]. Interaction of the semiconductor film with moisture and oxygen from air leads to decrease in drain current along with any change due corona embedded charges. The devices with additional polystyrene protection coating on the backside displayed better device performance than the devices without polystyrene. The stability increase given by the polystyrene layer is illustrated in Figure 17(a), where the polystyrene protective layer decreases the rate of charging effectiveness loss. After 24 hour aging in open-air the devices become stable. The stability of these charges and hence the resulting modified OFET (after aging) was studied over the period of a week and is comparable to silicon-based OFETs Figure 17 (b).

This experiment is just an initial demonstration of potential possible way to trap the electrostatic charges for longer periods of time in plastic substrate in order to obtain stable, always-on devices, and can clearly be further optimized, for example, by using a denser or even more hydrophobic polymer coating. Also, the effectiveness of this layer supports the hypothesis that the charged implanted from the back side are indeed active in controlling the conductance of the front-face semiconductor. There are several other polymers like Teflon and PEN etc., which can store charge better then PET but most of them have inferior mechanical, properties as compared to PET. According previous literature [45], charge storage lifetime for PET can be up to 300 days while for PEN it can be up to 90 years. As the cost and flexibility of the

device are major considerations here, PET seems to be the best compromise for developing the low cost flexible devices being discussed here.

Ammonia Response

The ammonia sensitivity was investigated by monitoring the percentage change in the drain current of PET-gold devices on exposure to 0.5 and 1.5 ppm of ammonia. The devices were exposed for 5, 20 and 30 minutes and the corresponding percentage decreases in current were 17.8%, 36.7% and 40.8% for 0.5 ppm exposure and 31.4%, 46% and 53.7% for 1.5ppm ammonia exposure respectively, as shown in Figure 18.

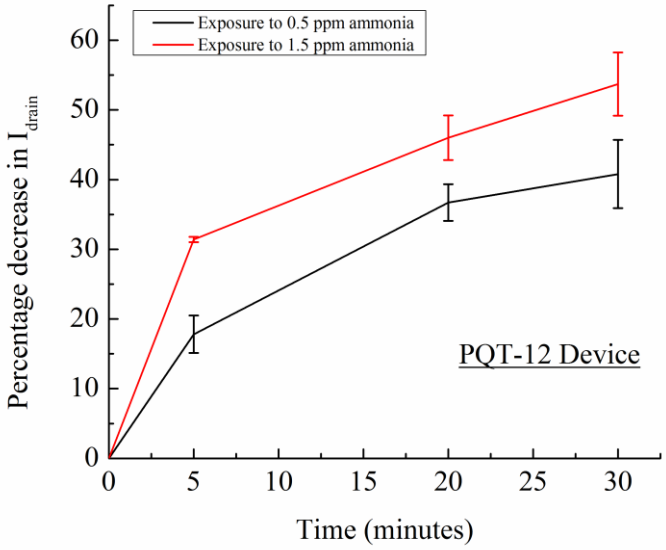

Figure 18 Percentage decrease in drain current after 5, 20, 30 minutes exposure to 0.5 ppm ammonia, average of 3 devices.

The devices were exposed to dry air at 1000 cm^3/min to account for any sensitivity of the device to dry air alone. As can be seen in Figure 19, an average drain current

decrease of only 2.9% was observed in 30 minutes, far less than the exposure-induced changes.

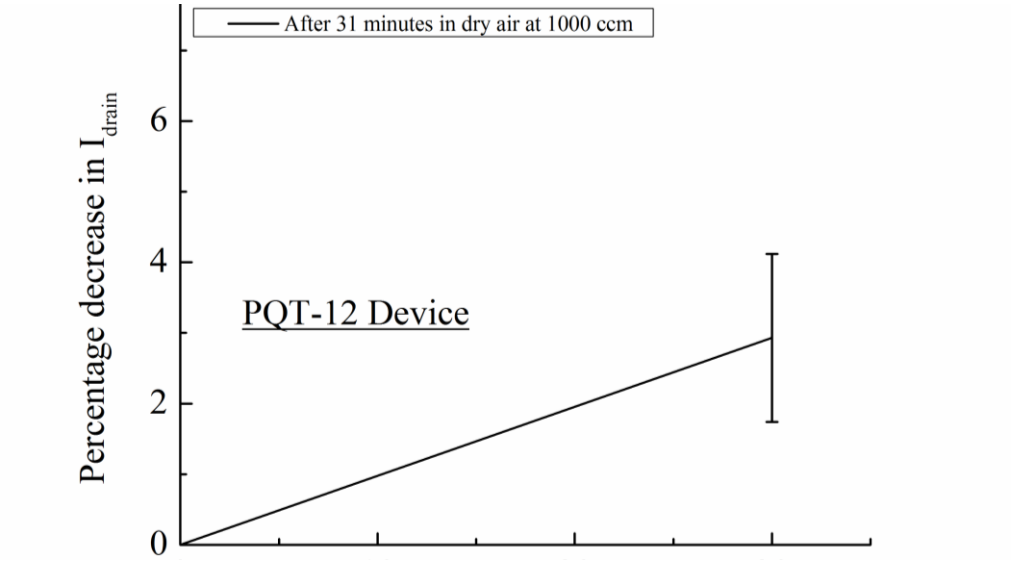

Figure 19 Effect of dry air exposure for 31 minutes at 1000 cc/min.

These responses to ammonia are very conservative as devices were measured outside the exposure chamber and there is a time lapse (>1minute) between ammonia exposure and recording of responses. The limit of detection for these sensors is at least as little as 0.1 ppm, Figure 20, which is below the current EPA regulation of 0.14-ppm ammonia exposure (www.epa.gov/iris/subst/0422.htm, (accessed 01/16/2014). To enable more uniform flow and to demonstrate an ultimately applicable format, we incorporated a sensing device inside a modified wearable Ogawa badge, as exhibited in Figure 21. This badge includes a porous front end that collimates and moderates airflow in front of the device. Devices with Ogawa sampler showed full recovery, in half the time, as compared to device without the sampler. It is possible that for PQT12, ammonia molecules delivered by

air flow had enough kinetic energy to reach less accessible but stronger binding sites, where it formed deeper and more stable traps, while the sampler limited the kinetic energy of the arriving ammonia and the vapor molecules only adsorbed on more exposed and more weakly bound sites.

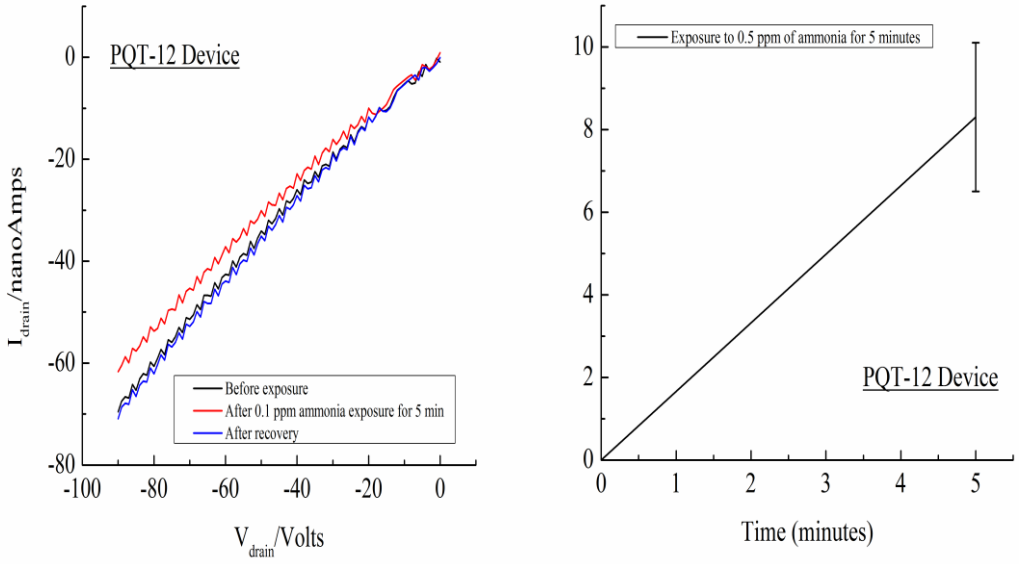

Figure 20 Response to 0.1 ppm of ammonia, flow rate 1500 cc/min, a) I-V plot and b) Reproducibility of three devices.

Figure 21 Ogawa badge sampler with responsive device mounted inside.

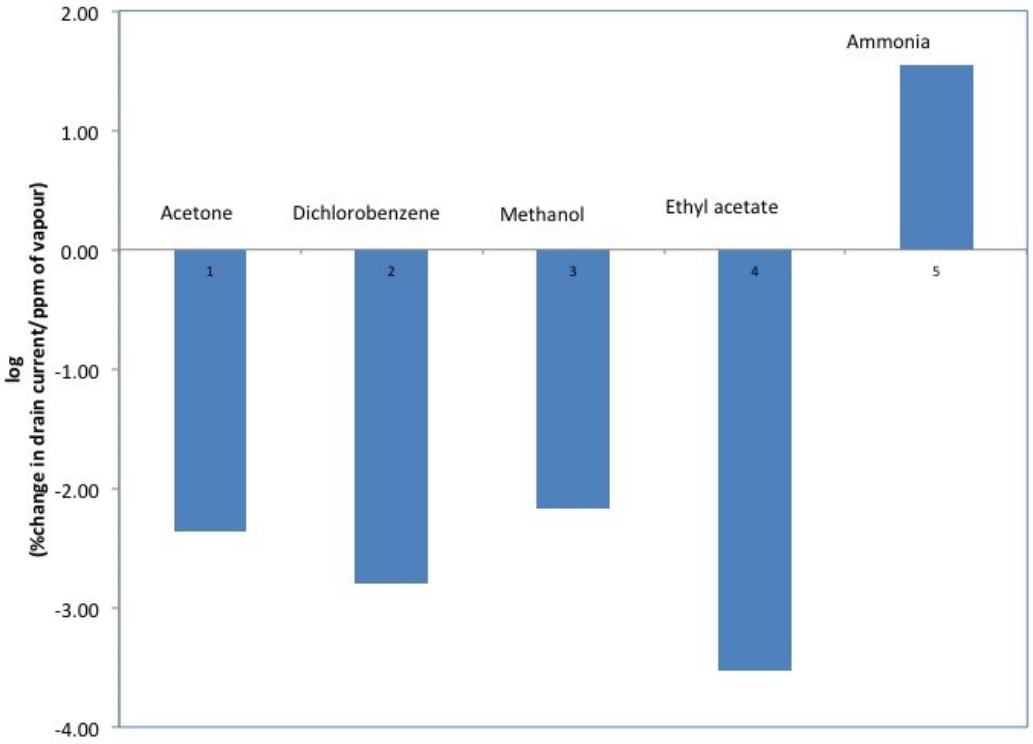

Figure 22 PQT-12 responses expressed as logarithmic percent change of current per ppm of analyte vapor.

Selectivity studies were conducted for common solvent vapors like acetone, methanol, ethyl acetate and dichlorobenzene, as these vapors can be present in agricultural or industrial environments.

Methanol was especially chosen, as it is a very good analogue of water due to similar polarity, size, electronegativity and binding properties. The devices were exposed to saturated vapor concentration of the listed solvent for 5 minutes. The logarithms of percent current decreases per ppm of the analyte vapors are shown in Figure 22, where it can be seen that the response for ammonia is much greater than for all the other vapors. The sensor reacts with other amines but the response magnitude is

smaller, probably due to the steric hindrance of those amines as compared to ammonia.

Along with selectivity, retention of the response is also a very important consideration for dosimetric sensors. As has been mentioned earlier, the reported devices recover when kept in open air and recording the response might not always be the most feasible option. This device if stored in a sealed fluorware container after exposure, at -30°C, retains the response. Some further decrease in current was observed in the exposed devices as well as control samples (Figure 23), because of the sub-ambient temperature at which they are tested after cold storage, but the current difference due to ammonia exposure remains apparent, and would allow retention of any differential response measurement between an exposed and a reference device. The storage temperature is apparently low enough to prevent debinding or diffusion of ammonia out of the device.

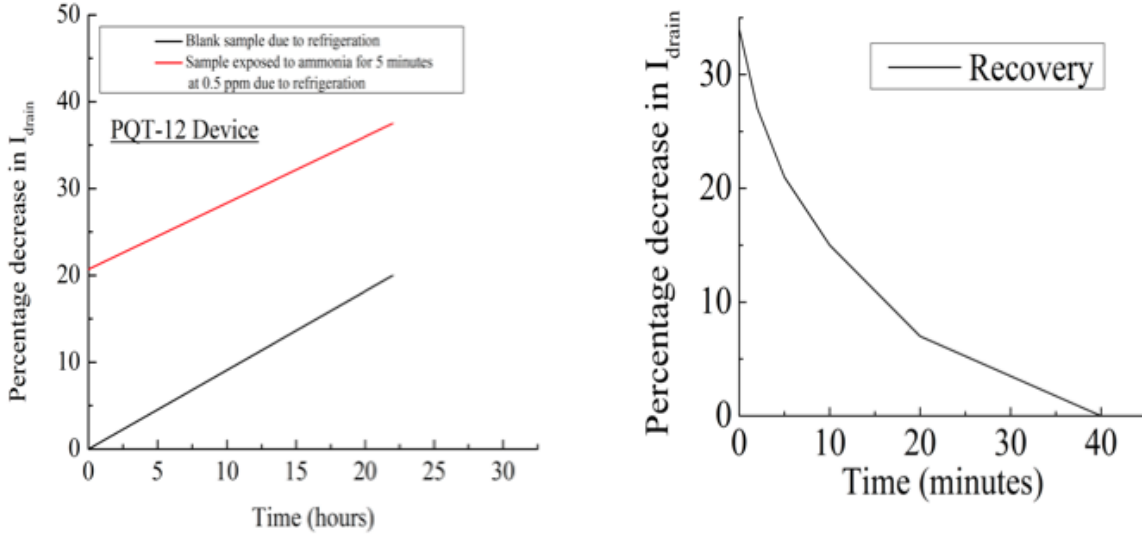

Figure 23 Current change of different exposed PQT-12 devices a) Stored in refrigerator b) Stored in air at room temperature after ammonia exposure.

Besides using low temperature to slow desorption of ammonia, we could conceivably retain the response using a bistable circuit comprising a pair of complementary inverters fed back to each other, with the ammonia acting as the stimulus to switch the output voltages. Once the status of the circuit is changed due to this external stimulus, it would not be easily reversible. One necessary condition to design such a device is to have two complementary semiconductors, which give opposite responses to ammonia, but where the magnitude of the response is similar. We have matched PQT-12 with the n-channel solution-deposited small molecule DPP-CN that gives almost the same response (15% increase in drain current), (Figure 24) but in the opposite direction, to 0.5 ppm of ammonia in five minutes using the same configuration as the PQT12 devices. Future work will utilize this or a similar pair of solution-deposited semiconductors with the goal of producing a responsive and all-printed bistable circuit.

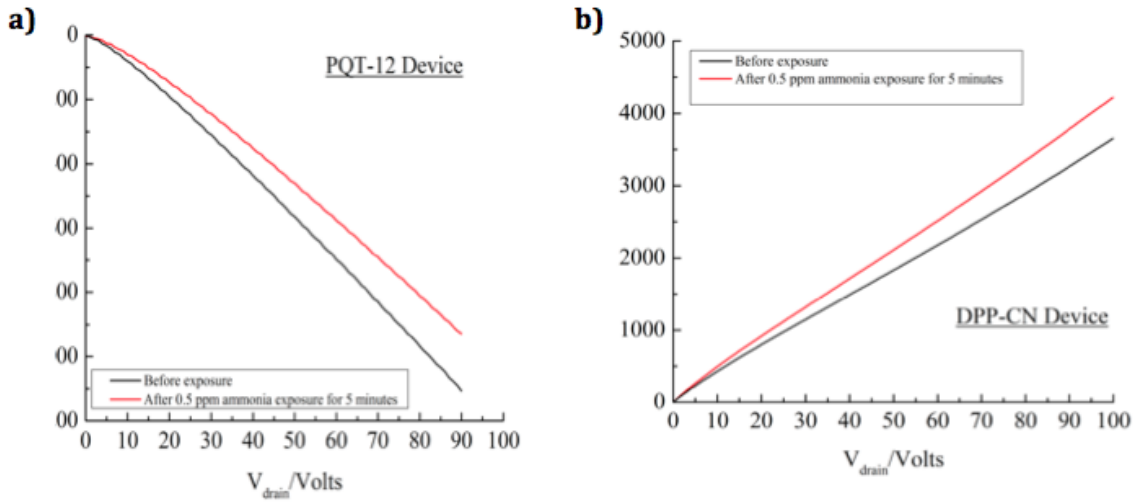

Figure 24 a) PQT-12 device, 16.2% decrease in drain current, b) 2,2'-[(2,5-dihexadecyl-3,6-dioxo-2,3,5,6-tetrahydropyrrolo[3,4-c]pyrrole-1,4-diylidene-5,2-diylidene]dimalononitrile device, 15.3% increase in drain current, on 0.5 ppm ammonia exposure for 5 minutes.

PQT-12 is obviously sensitive to ammonia, but due to its moderate mobility, high voltage has been required for operation. Using a blend of high mobility material "SP210" catalog number 1.39695.0200 SP210.0001 supplied by EMD Millipore Corporation (dba EMD Chemicals) (we are thankful to EMD Corporation for donating this material for research purpose) and PQT-12 in 3:1 ratio provided a good compromise between sensitivity and conductance. The sensitivity of the blend is lower than for pure PQT-12, but the device could operate well below 5 volts supply (Figure 25). Another alternative for lowering operating voltage is to simply use higher W/L ratios.

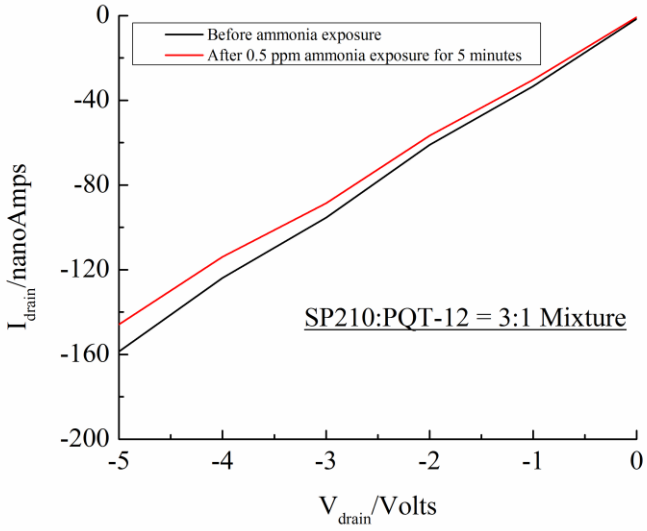

Figure 25 Low voltage operated device based on a blend of PQT-12 and another commercially available conductive polymer as the sensitive material.

2.2.6 Conclusion

We have developed a flexible and cost-efficient ammonia sensor platform with a sensitivity of 0.5 ppm and a limit of detection of 0.1 ppm that is well suited for large area (or roll-to-roll) processes. Devices based on PQT-12 and DPP-CN give opposite

responses to similar exposures to ammonia, which is essential to design a complementary logic-based ammonia sensor. The sensors are highly selective for ammonia over volatile organic compounds. Keeping the devices in a sealed container in a freezer can preserve current changes which can be useful for dosimetric sensors.

Acknowledgement

We are grateful to the NIOSH (Grant No. 5R21OH010190- 02) FlexTech Alliance and Johns Hopkins Environment, Energy, Sustainability & Health Institute for supporting this work. We want to thank Dr. Xin Guo for synthesis of PQT-12 and DPP-CN, used for this project. We would also like to thank EMD Chemicals for generously donating of SP210 polymer for this research project.

2.3 Challenges and Alternative Solution

We have achieved high sensitivity and selectivity for both, a vapor deposited ammonia sensor and for a fully printed version, but both the techniques still have some drawbacks. As has been discussed earlier, vapor deposition makes the OFET sensors more expensive and time consuming and thus unsuitable for mass production. On the other hand the printable version discussed in section 2.2 is feasible for mass production owing to easy processibilty but retaining the corona embedded charges for longer period of time effectively is still a challenge to be resolved.

For OFET sensors in general, when I_d is used as a parameter to measure the sensing activity, it becomes very important that a stable baseline is achieved as a reference for any changes in I_d due to day-to-day changes in temperature and humidity conditions. Also, as has been discussed earlier mobility and thus the I_d of an OFET are closely related to morphology of the film, which could be easily altered by even a slight change in deposition conditions from batch to batch.

To ensure that the variance in the performance of an OFET does not affect the sensing capabilities of the sensing platform, we suggest an inverter circuit to be used instead of a single OFET. Complimentary metal– oxide–semiconductor field-effect transistors (CMOS) circuits use a combination of p-type and n-type metal–oxide– semiconductor field-effect transistors (MOSFETs) to implement logic gates and other digital circuits. The basic circuit design is shown in Figure 26. The top FET is a PMOS type device while the bottom FET is an NMOS type device. Both

gates are connected to the input line. The output line connects to the drains of both FETs. A CMOS circuit functions as an inverter. Thus a high input gives a low output voltage and low voltage gives a high output voltage as is expected for any inverter.

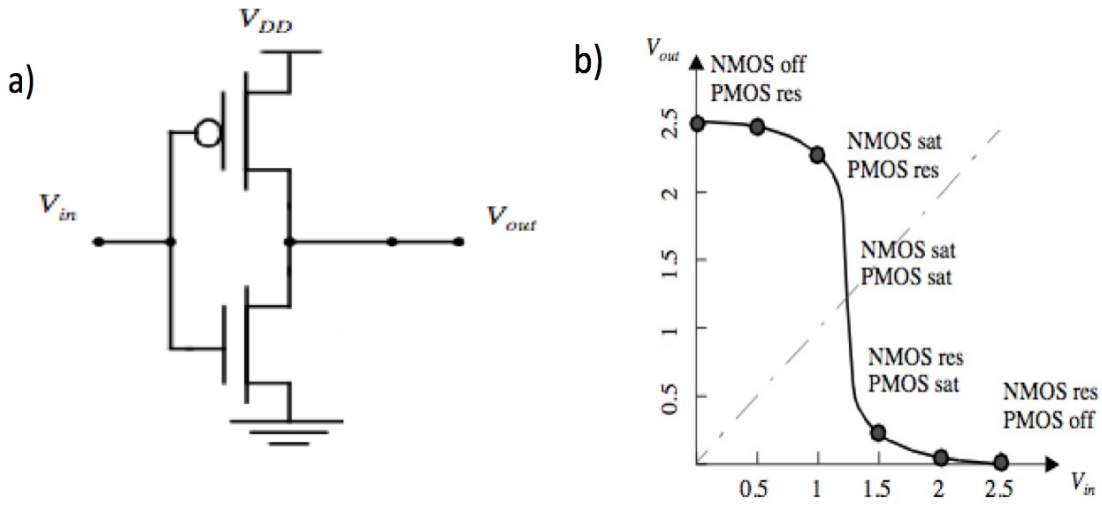

Figure 26 a) Circuit for a CMOS inverter b) Voltage transfer curve of a CMOS inverter, modes of operation are annotated-off, res(istive), sat(urated).

We would like to use DPP-CN and PQT-12 as the complimentary N and P type semiconductors for the inverter. Both of these semiconductors give equal response to ammonia in opposite directions. We published similar device structure for ammonia sensing[46] but the structure was a silicon based vapor deposited system with a very high limit of detection of 4 ppm.

Here we would like to propose a fully printable inverter-based structure for ammonia sensing with limit of detection as low as 0.1 ppm. In an inverter one OFET is always on, depending on the input voltage. The output voltage can also be manipulated by some other external stimulus, as that would change the resistance across the two OFETS. In this case we propose to use ammonia gas as the external stimulus, which would turn on the N-type OFET and would switch off the P type

OFET thus changing the output voltage from high to low. Following the basic design with statically charged gate on 12 micron PET, we have been able to demonstrate a preliminary result for the switching off the voltage using ammonia, Figure 27. Retention of the ammonia response (for testing the samples at a later time) might be a slight issue with either a single transistor or even with an inverter based device.

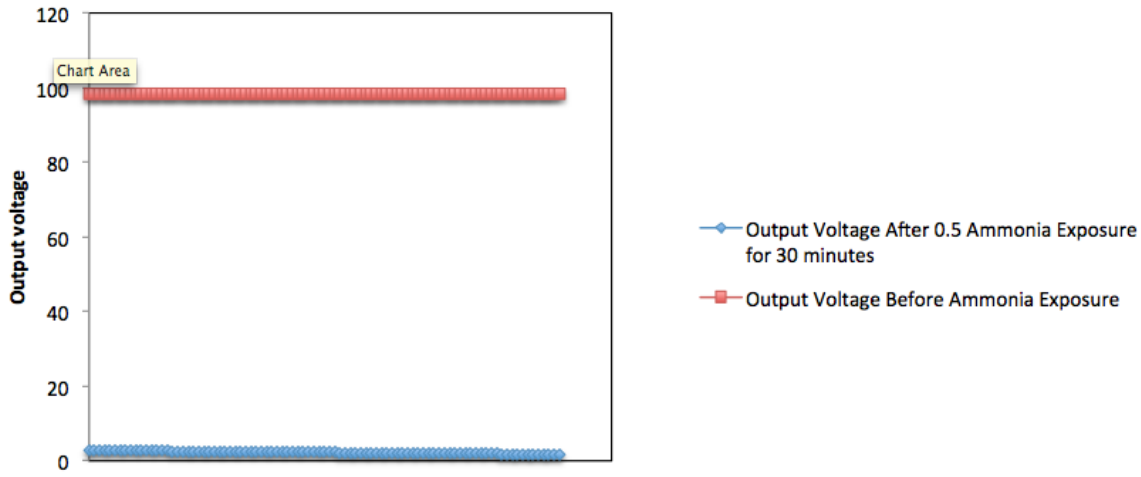

Figure 27 Response of an inverter based on static gate to 1ppm ammonia exposure.

In order to address the issue of response retention we plan to develop a bistable circuit with two inverters, where the output from one inverter is connected to the gate of the other inverter and vice versa. This kind of structure would retain any perturbation introduced if the overall gain in the voltage is more than 1. Schematic of such a device is shown in Figure 28. We would like to exploit the same for retention of response to ammonia exposure. For designing a bistable circuit, a traditional OFET structure with a gate electrode (to supply gate voltage) would be required. Thus we need to revert back to the conventional OFET structure.

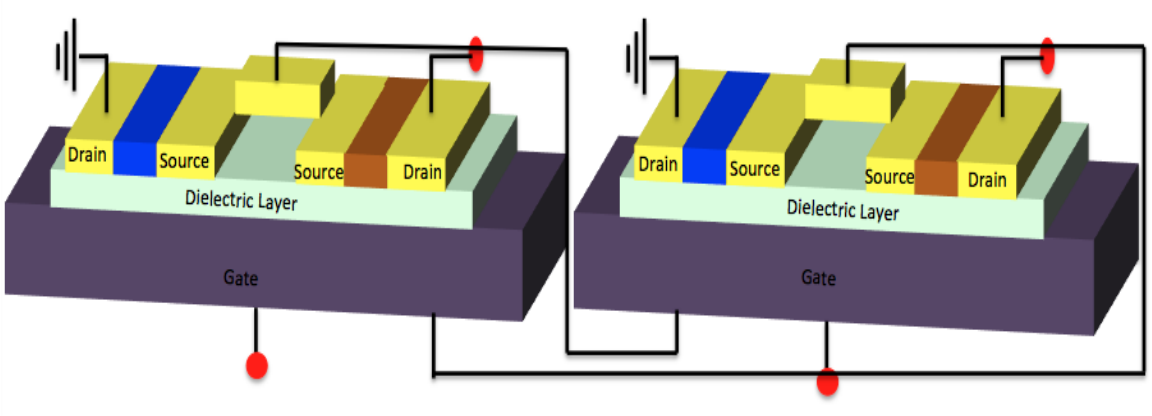

Figure 28 Schematic of a bistable circuit.

Using traditional OFET would resolve the issue of retention of corona embedded charges but then in this case again, we would need a reliable printable dielectric to achieve fully printable sensors. To achieve this goal we have designed a self-healing polymer dielectric[47].

2.4 Self-Healing Polymer

2.4.1 Introduction

As is well known, Printable and flexible electronic components are more susceptible to scratching, rupture, or other damage from bending or stretching due to their "soft" nature compared to their rigid counterparts, such as Si based electronics, resulting in loss of functionality. Self-healing ability, an important feature of living creatures[48–52], is highly desirable for these "soft" electronic devices. However, most research toward this goal has been limited to conductive media, such as conductive wire, film and bulk materials[49–54]; there has been very little work on integrating self-healing materials into organic field effect transistors (OFETs), and especially not as gate insulators. Developing a material that simultaneously exhibits excellent dielectric properties for OFETs and autonomic mechanical self-healing behavior is still an unmet challenge. Although two reports introduce self-healing dielectric layers into organic field effect transistors, they only demonstrate the healing behavior following dielectric breakdown, rather than after both mechanical and electrical breakdown[55,56], and the electrical self-healing process is relatively slow. Furthermore, these were not based on a potentially printable technology.

Here, we developed a versatile blend polymer system, poly(2-hydroxypropyl methacrylate)/poly(ethyleneimine) (PHPMA/PEI), as dielectric layer for high performance, self-healable, printable and flexible OFET for the first time; this polymer blend shows surprisingly high capacitance (1,400 nF/cm^2 at 120 nm thickness and 20 Hz), much higher than all previously reported polymer dielectrics[57–60], except for ion-gel dielectrics which contain more than 90% ions in

the material[61–64]. Furthermore, this blend polymer system exhibits excellent self-healing behavior.

2.4.2 Material Design

In order to obtain a high performance self-healable material as dielectric layer for printable and flexible OFETs, the material should be readily soluble in common solvents, thus allowing solution processability. More importantly, high capacitance is desirable, as well as capability for self-healing. Poly (methyl methacrylate) (PMMA) is a commonly used solution processable dielectric; however, it has no self-healing ability under mild conditions due to lack of dynamic bonding and reversible reaction sites. Therefore, we chose its derivative, poly (2-hydroxypropyl methacrylate) (PHPMA), as an alternative (Figure 29); the introduction of the hydroxyl group will significantly strengthen interactions between polymer chains via numerous dynamic hydrogen bonds. However, this polymer shows a high glass transition temperature, above 100 ^{o}C, indicating that the polymer chains have limited mobility at room temperature. In order to overcome this obstacle, we employ a more flexible polymer additive, poly(ethyleneimine) (PEI), which can interact with PHPMA through dynamic hydrogen bonds. The resulting blend polymer system shows an amorphous structure with a much lower glass transition temperature (below 40 ^{o}C). As a result, the polymer chains of the blend system have much higher freedom of motion at room temperature than PHPMA alone, which should significantly improve self-healing ability. Both poly (2-hydroxypropyl methacrylate) and poly (ethyleneimine) are readily soluble in ethanol, an environmentally friendly and inexpensive solvent, and an orthogonal solvent for

most semiconductors,[65–67] meaning that our blend dielectric layer can also be easily coated on semiconductor films without causing damage. Also, most solvents for semiconductors such as toluene, THF, chloroform, acetone, dichlorobenzene and dichloromethane cannot dissolve the blend dielectric layer, providing us a much more convenient and efficient way to manufacture devices with varied architectures.

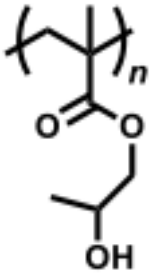

Poly(2-hydroxypropyl methacrylate)

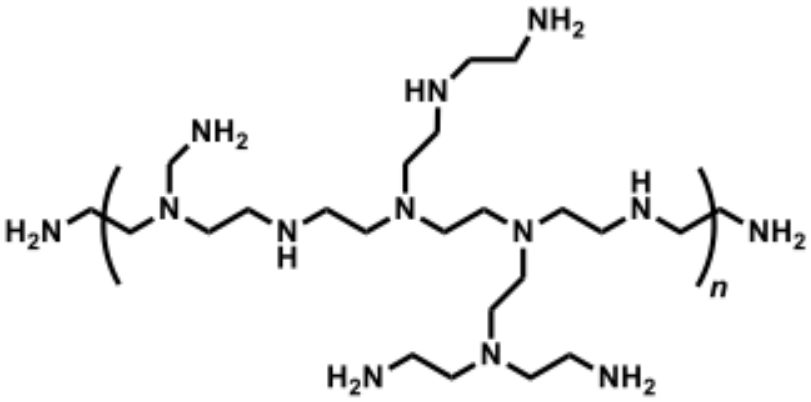

Poly(ethyleneimine)

2

Figure 29 Chemical structure of polymer used for making self healing polymer a) Chemical structure of 1: poly(2-hydroxypropyl methacrylate) (PHPMA); 2: poly(ethyleneimine) (PEI).

2.4.3 Device Fabrication For Self Healing OFET

Capacitors were prepared by spin coating polymers on ITO coated glass. Some polymer films were annealed at 100 ^{o}C for 60 minutes in N_2, and dried for 1 hour under vacuum. 50-nm-thick Au top contacts were deposited through a shadow mask to form a 37 μm by 37 μm square electrode.

OFETs were prepared on flexible substrates. Polymer dielectric was first spincoated on ITO-coated 127 μm thick PET thin sheets, then annealed at 100 ^{o}C for 1 hour in N_2, and dried for 1 hour under vacuum. Pentacene and 5FPE-NTCDI were thermally vapor deposited under high vacuum ~3 * 10^{-6} torr at rate of 0.3 Å/s with final thickness of 50 nm. During the deposition, the substrates were held at 80 ^{o}C. Quinacridone OFETs were fabricated according to previous literature[68] ; before quinacridone deposition, 30nm $C_{44}H_{90}$ was first deposited on the dielectric layer because the low surface energy of the aliphatic $C_{44}H_{90}$ is critical for growth orientation of the H-bonded molecules, providing π-stacking parallel to the gate electrode and therefore high mobilities[68] . P3HT solution was spin-coated at a speed of 1000 rpm for 90 seconds, then annealed at 80 ^{o}C for 15 minutes in N_2, and dried for 1 hour under vacuum. 50 nm Au source drain contacts were thermally vacuum-deposited at ~3 * 10^{-6} torr. Some pentacene and P3HT OFETs were also prepared on non-annealed dielectric blends.

For the self-healing OFETs, we first thermally deposited 50 nm Au source drain contacts on flexible PET sheets at ~3 * 10^{-6} torr, then drop cast P3HT solution (10 mg/mL in dichlorobenzene) on Au electrodes and annealed for 3 hours at 90 ^{o}C in vacuum; then self-healing polymer (200 mg/mL, PHPMA/PEI blend) ethanol

solution was drop cast on the P3HT layer to form a 16 ± 2 μm thick dielectric layer; finally 18 ± 5 μm carbon paint was coated on the self-healing polymer dielectric layer and dried under vacuum to form a gate electrode.

2.4.4 Electrical Characterization and Sensor Test

We used a MIM (metal-isolator-metal) architecture device for capacitance measurements; the results are shown in Table 2. PS (polystyrene) and PMMA (poly(methyl methacrylate)) show typical capacitance values as previous reports at a thickness around 100nm[61,62], PHPMA shows a higher capacitance value (66 nF/cm^2) than PS and PMMA at the same thickness range, and the value decreases proportionally with the increasing film thickness, which is a typical feature for electron polarized dielectric materials.

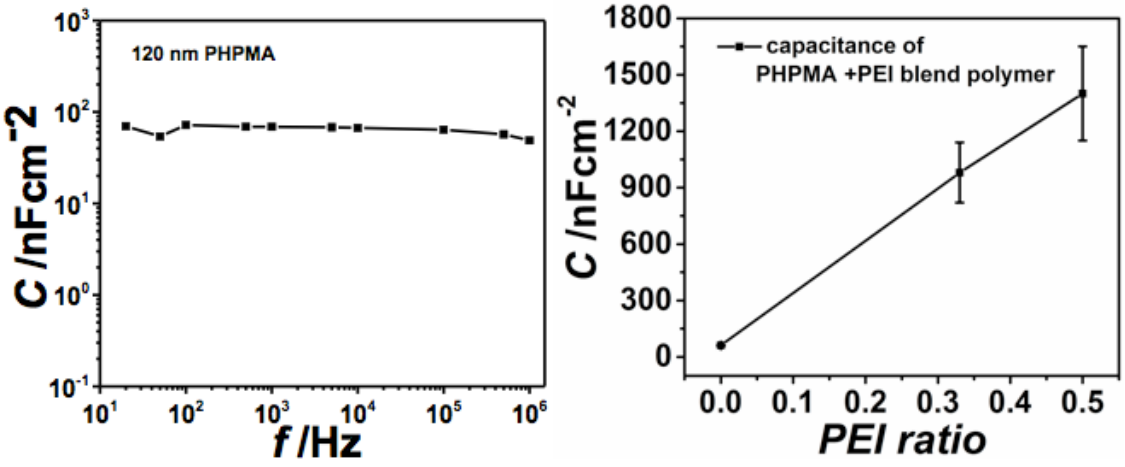

Figure 30 Capacitance of PHPMA film and PHPMA/PEI blend film over PEI weight ratio.

Surprisingly, after blending with PEI (2:1 weight ratio), the capacitance drastically increased up to 980 nF/cm^2, further increase of the PEI weigh ratio to 50% lead to a higher capacitance value of 1400 nF/cm^2 (Figure 30), which is higher than all the

reported polymer dielectrics[57–62,64] (except ion-gel dielectrics which contain more than 90% ions in the material). The possible reason for the high capacitance is that the lone electron pair on nitrogen atoms in poly(ethyleneimine) may generate large dipoles when interacting with the OH groups on PHPMA[69,70]. Additionally, the capacitance value has negligible dependence on film thickness; even a 16 μm thick film still exhibits a significantly high capacitance value of about 1060 nF/cm^2 at 20 Hz. This is the first report of a neutral polymer maintaining such high effective capacitance at a macroscopic thickness, useful for robustness and printability. The capacitance decreases with increasing of frequency, as shown in Figure 31, similar to what is observed with ion- polarized dielectric materials[61,62,64].

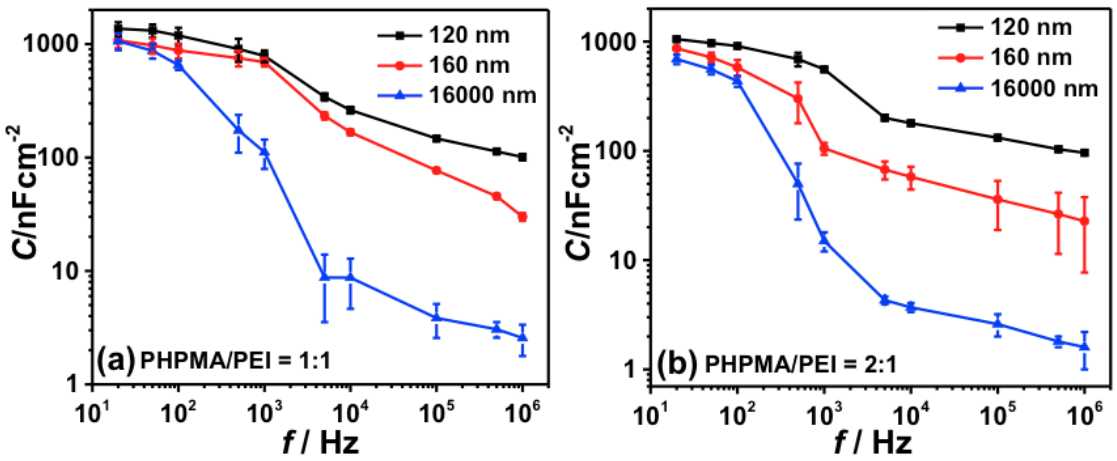

Figure 31 Capacitance frequency relationship at various thickness and diffrent PEI ratios a) PHPMA/PEI=1:1; 2) PHPMA/PEI=2:1.

From Figure 31, we noticed that the thickness dependence of capacitance per unit area is related to both PHPMA/PEI ratio and operating frequency. More specifically, at low frequency, such as 20 Hz, the capacitances of blend polymer film are largely independent of thickness, films with very wide thickness range (from 120nm to 16

μm) show a very narrow capacitance value distribution (650 nF/cm^2 to 1400 nF/cm^2), however, with increasing frequencies, the thickness dependence of film capacitance become more and more obvious.

The possible reason for this phenomenon may be that, at low frequency, the thicker film get enough time to be polarized by electrical field, therefore, thicker film shows comparable capacitance value with thinner film. However, at higher frequency, there is not enough time for thicker film to be completely polarized, resulting a smaller capacitance value compared to thinner films.

Dielectric layer	**Thickness [nm]**	**Capacitance [nF/cm^2] at 20Hz**
PS[a)] [10 mg/mL]	100 ± 15	26 ± 2
PMMA[b)] [10 mg/mL]	150 ± 20	20 ± 1
PHPMA[c)] [10 mg/mL]	120 ± 20	66 ± 4
PHPMA [100mg/mL]	1800 ± 200	5 ± 0.25
PHPMA + PEI[d)] [10mg/mL, 2:1][e)]	120 ± 20	980 ± 160
PHPMA + PEI [100mg/mL, 2:1]	3200 ± 200	900 ± 120
PHPMA + PEI [10mg/mL, 1:1]	120 ± 20	1400 ± 250
PHPMA + PEI [20mg/mL, 1:1]	160 ± 20	1050 ± 160
PHPMA + PEI [200mg/mL, 1:1]	16000 ± 1000	1060 ± 250

[a)]PS: polystyrene; [b)]PMMA: poly (methyl methacrylate); [c)]PHPMA: poly (2-hydropropyl) methacrylate; [d)]PEI: poly (ethyleneimine); [e)] All are weight ratios.

Table 2 Capacitance study for different dielectric layers.

Furthermore, PEI ratio in this blend polymer also affect this thickness dependence behavior, in the blend polymer film with higher PEI ratio, capacitance values show less thickness dependence, and in the blend polymer film with higher PHPMA ratio, capacitance values show higher thickness dependence, this make sense because capacitance value of solely PHPMA film is completely inverse proportional to its film

thickness. The very high capacitance of this unannealed polymer blend is also accompanied by significant loss, with the tangent of the phase angle approximately unity. The capacitance decreases, by a factor of 20-50, on baking for one hour at 100 °C followed by vacuum drying (the "annealed form"), and the loss tangent decreases by an order of magnitude as well. This is likely due to a combination of the driving away of low molecular weight components of the PEI, decreased free volume leading to more restricted functional group motion, and stabilized hydrogen bonds from which protons are less likely to be dislodged.

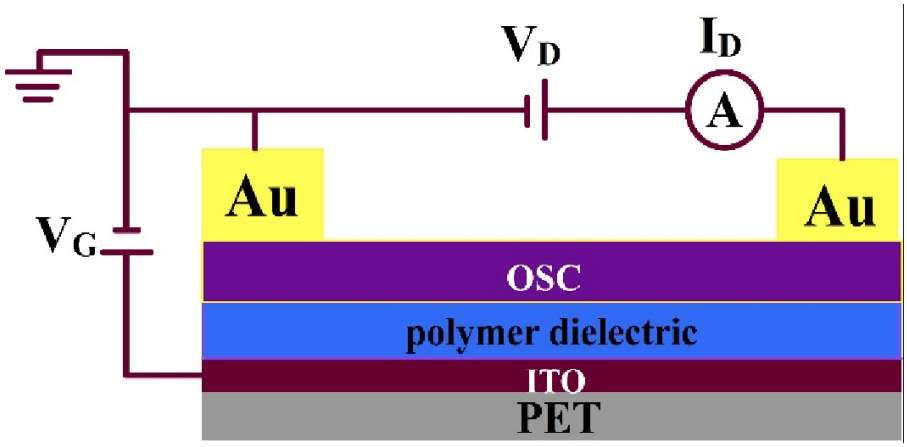

Figure 32 Schematic used for making SHP dielectric based OFETs.

In order to evaluate the performance of the self-healing polymer (PHPMA/PEI 1:1 blend) in OFETs when used as gate dielectrics, bottom-gated OFETs were fabricated on flexible ITO coated PET substrates (Figure 32). Four conjugated molecules: pentacene, *N*, *N*'-bis(2-(pentafluorophenyl)ethyl)-1,4,5,8-naphthalene tetracarboxylic acid diimide (5FPE-NTCDI), poly(3-hexylthiophene) (P3HT) and quinacridone[68], which cover the range of p and n-type, small molecule and polymer, hydrophilic and hydrophobic semiconductors, were employed to comprehensively

assess the performance of PHPMA/PEI (1:1) blend self-healing polymer as a dielectric material Figure 33.

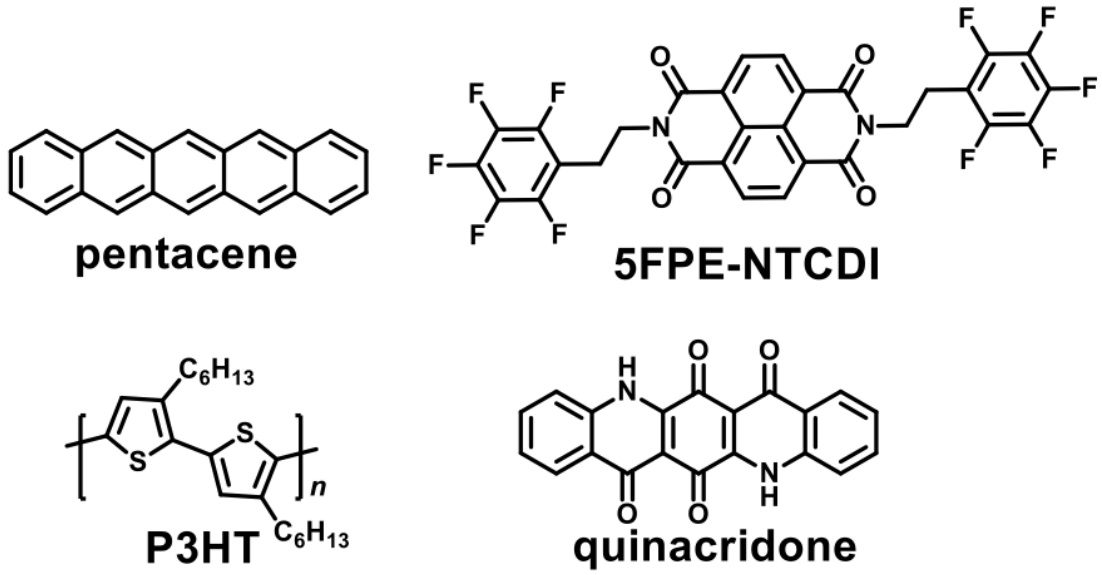

Figure 33 Chemical structure of four semiconductors used for making SHP dielectric based OFETs.

As a control, OFETs with PS, PMMA, PHPMA and SiO_2 (no surface treatment) as dielectrics were also fabricated under exactly the same conditions as for the self-healing polymer, the only difference being that the OFETs with SiO_2 as dielectric were fabricated on rigid silica wafers, not on flexible PET substrates.

Hydrophilic (highly polar) surfaces have generally been found to be unfavorable for charge carrier transport in OFETs due to their providing trap sites for electrons and holes[65–67], decreasing mobility and increasing the threshold voltage. However, our self-healing polymer-based OFETs still show significantly higher drain current values with lower driving voltages than for OFETs using the other four dielectrics due to the much higher capacitance of the blend, as we can see from Figure 34

transfer curves for OFETs with the other four dielectrics are shown in (Figure 35 to Figure 38).

Dielectrics	OSC	Pentacene	5FPE-NTCDI	P3HT[a)]	Quinacridone[b)]
PHPMA/PEI 1:1 [120 nm]	μ [$cm^2V^{-1}S^{-1}$]	(1.71±0.37) E-01	(1.94±0.15) E-02	(2.0±0.34)E-01	(4.8±2.4)E-02
	V_{th} [V]	-2.59±0.193	-0.41±0.14	-4.04±1.32	-4.77±0.76
	On/off ratio	(8±4)*10^3 at -4 V	(2.3±1)*10^1 at 3 V	5*10^1 to 10^3 at -10 V	(1±0.12)10^2 at -10 V
	Leakage current [A]	(4.24±1.48) E-7	(1.22±0.33) E-6	(7.18±0.99) E-6	(1.95±0.35)E-7

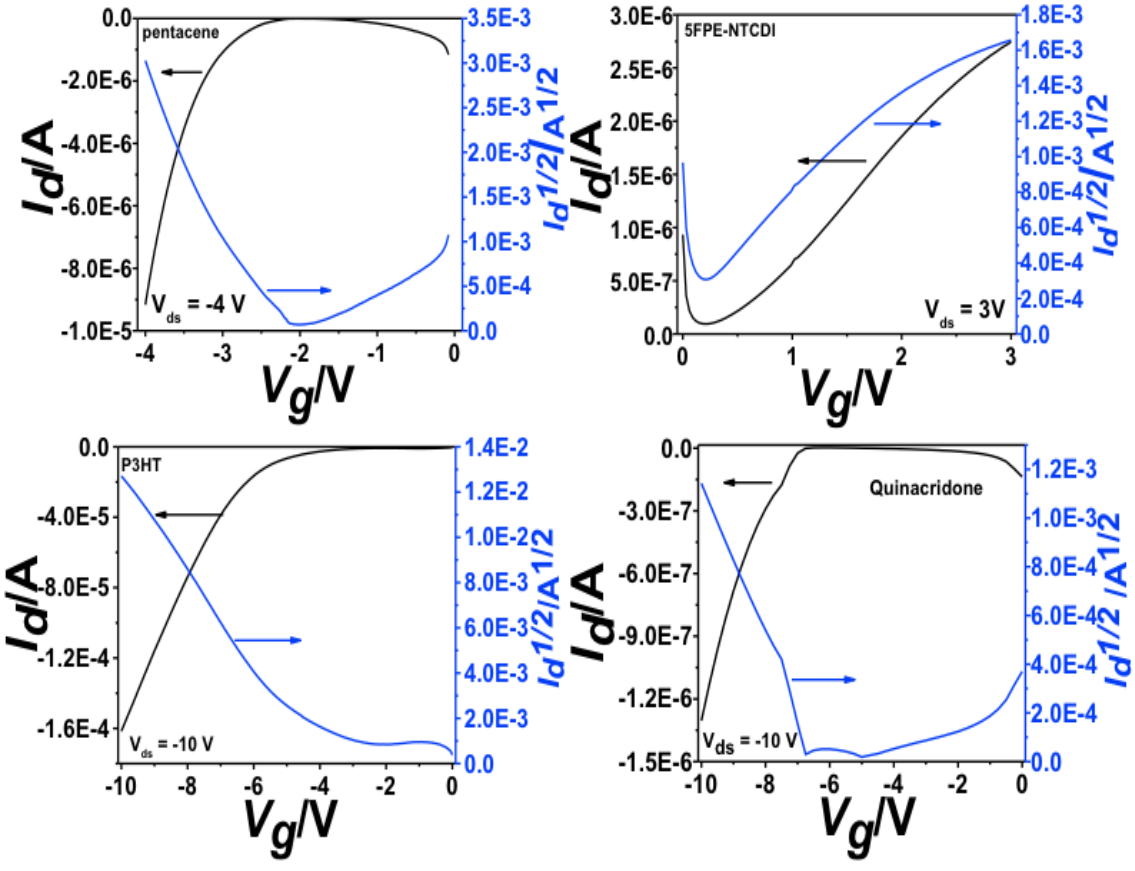

Figure 34 Performance of self-healing polymer in organic field effect transistor as dielectrics. I-V characteristics of SHP-OFETs, the devices have channel lengths of 250 **μ**m and channel widths of 8000 **μ**m. The gate voltage was swept at a rate of 50 mV S^{-1}.

Additionally, the mobilities of SHP (self-healing polymer)-OFETs and PHPMA-OFETs are usually higher than for OFETs using the other dielectric layers. It is believed that larger charge carrier mobilities are observed from high charge density induced in the OFET channel[61–66].

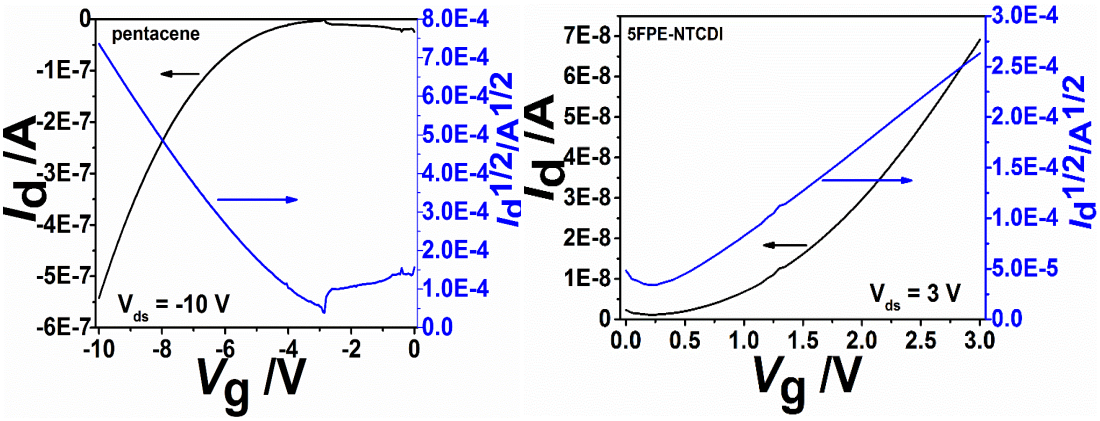

Figure 35 Transfer curves of pentacene and 5FPE-NTCDI OFET, using 150 nm PMMA as dielectric layer.

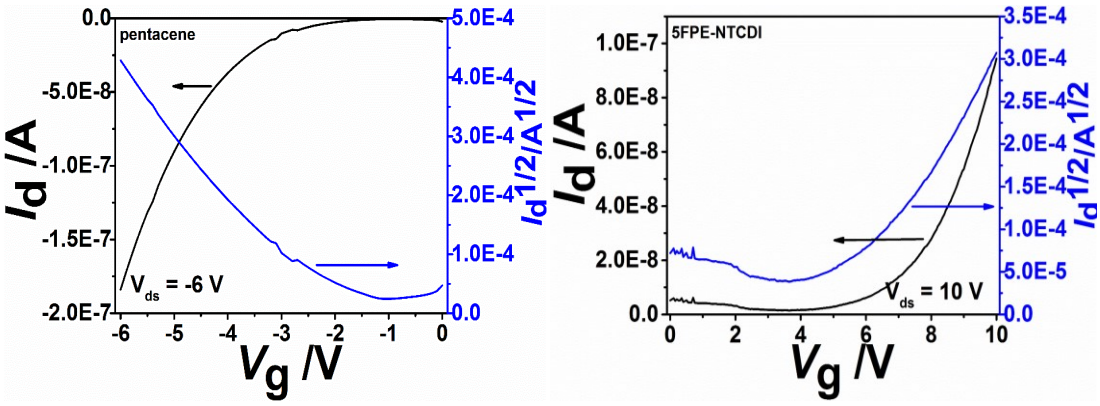

Figure 36 Transfer curves of pentacene and 5FPE-NTCDI OFET, using 100nm PS as dielectric layer.

Large carrier densities result in increased trap-filling and a general smoothing of electrostatic potential variations in the film due to trapped charge, and these combined effects may lead to higher carrier mobilities. Furthermore, SHP (self-

healing polymer) based OFETs show excellent stability during storage in ambient conditions.

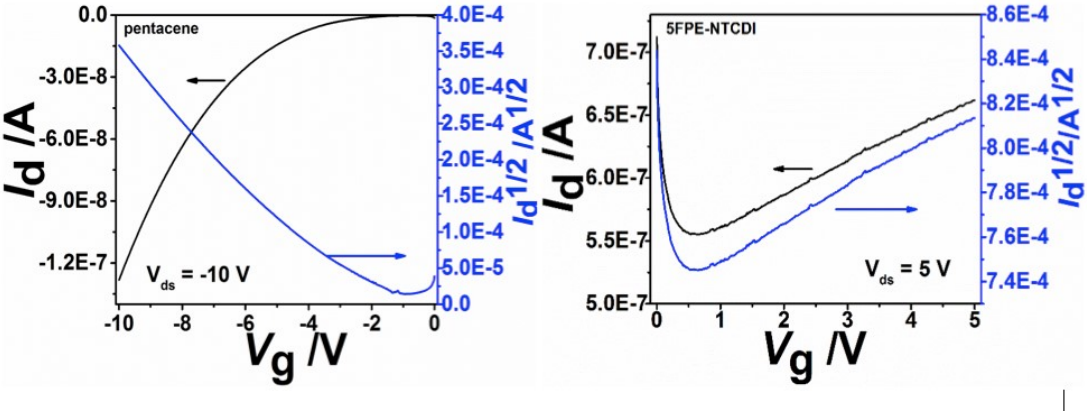

Figure 37 Transfer curves of pentacene and 5FPE-NTCDI OFET, using 300 nm SiO_2 as dielectric layer.

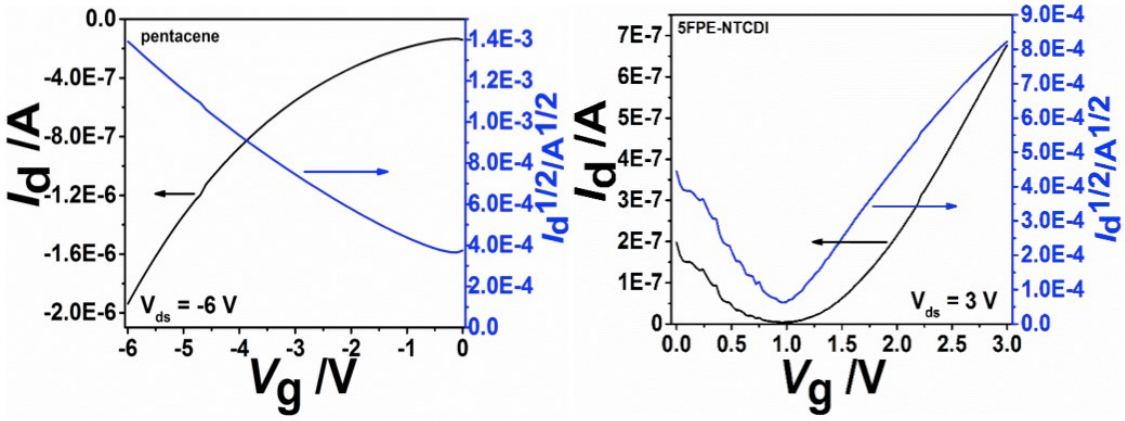

Figure 38 Transfer curves of pentacene and 5FPE-NTCDI OFET, using 120nm PHPMA as dielectric layer.

To demonstrate a self-healing OFET, we integrated both a self-healing polymer layer and a carbon paint layer into an OFET as dielectric layer and gate electrode respectively. Source and drain electrodes were patterned on a flexible PET substrate, then P3HT (10mg/mL in dichlorobenzene) solution was drop cast on Au electrodes

and annealed under low pressure N_2 at 90 ^oC for 3 hours to form a semiconductor layer; 200 mg/mL PHPMA/PEI (1:1) ethanol solution was drop cast on P3HT film and dried under vacuum to form a 16 μm thick dielectric layer; finally, carbon paint suspension was coated on the self-healing dielectric layer as gate electrode with a thickness of 18 ± 5 μm. The resulting top gate OFET shows excellent switching behavior at low operating gate voltage, before cutting, Drain current at -5 V is about -4.56 μA; A cut was made from the top cutting the dielectric layer and the gate electrode. Upon cutting (no damage on P3HT), drain current decreases to -2.15 μA due to the damage to the lower conductance of the carbon paint layer. After healing at room temperature in air for 10 hours, the carbon paint conductance was partially restored during the process of PHPMA/PEI dielectric healing itself; we see the transistor drain current increased to -3.63 μA. On cutting, the drain current and mobility decreased to 51% and 32.5%, the mobility decrease is probably due to the decrease of charge carrier density in the other half part of channel, which is less connected with gate probe. The threshold voltage also slightly shifts, on off ratio decreased due to drain current changed to a smaller value. After healed, the drain current increased to 75.8% of its original value, the mobility also increased to 63.7% of its original value, threshold voltage change towards its original value and on off ratio also increased as shown in Figure 39. This is the first report that multiple layers of an organic field effect transistor can automatically self-heal, achieving step toward fully self-healable electronic devices.

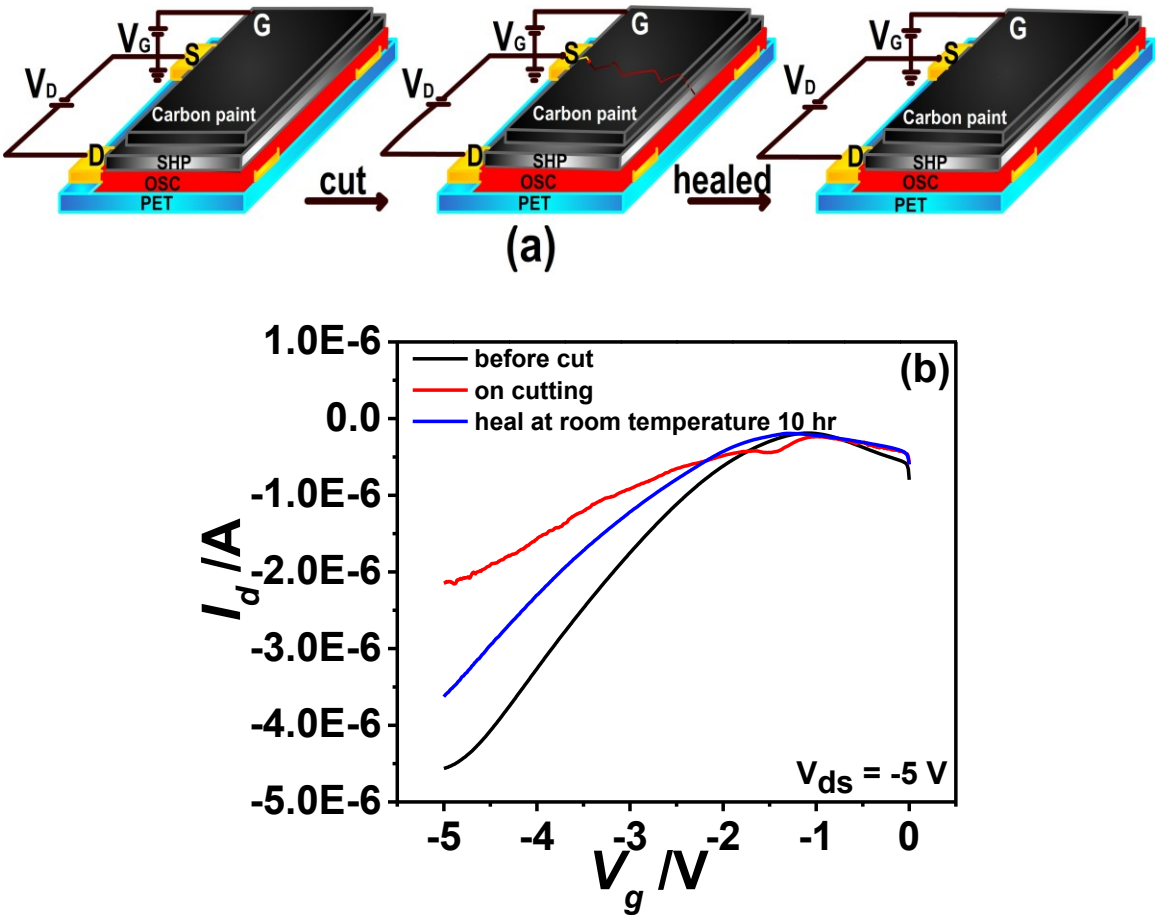

Figure 39 a) Schematic diagram of self healing organic field effect transistor, the damage in gate layer electrode layer can be partially healed together with the self-healing process of gate dielectric; b) Transistor characteristic during healing the test.

In order to establish these SHP OFETs as printable and low-voltage operable OFET sensors we exposed a flexible P3HT OFET device with PHPMA/PEI (1:1) blend as dielectric layer to 0.5ppm NH_3, with operating voltage of -5 V. After 5 minutes' exposure, the drain current decreased 23%, showing greater sensitivity than most reported P3HT NH_3 sensors.[71]The estimated limit of detection is much lower than 0.5 ppm. The possible reason for the higher sensitivity to NH_3 could be that this highly polar self-healing dielectric layer has significant affinity for NH_3, so the uptake of NH_3 by the sensor is increased, and more NH_3 can be adsorbed at the

interface between the dielectric layer and semiconductor layer (transistor channel), leading to a higher change of drain current.

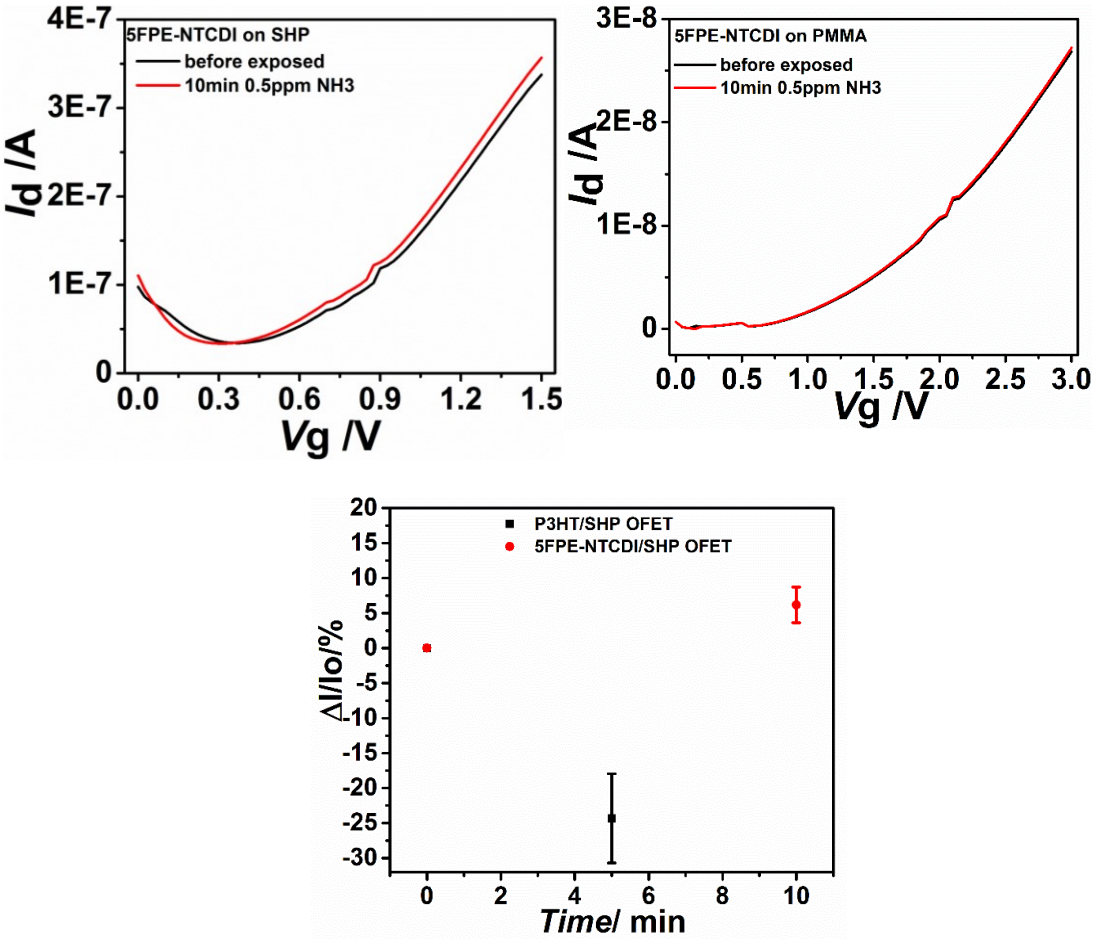

Figure 40 The sensing behaviour of PHPMA/PEI (1:1) and PMMA based OFET device. Responses of 5FPE-NTCDI OFETs to NH3; left, PHPMA/PEI (1:1) as dielectric; right, PMMA as dielectric; bottom, responses of P3HT/SHP-OFET and 5FPE-NTCDI/SHP-OFET device to 0.5 ppm NH3.

In order to verify this proposed mechanism, we use another semiconductor, 5FPE-NTCDI, instead of P3HT as sensing layer. 5FPE-NTCDI is a highly stable semiconductor, and it shows negligible response to NH_3, except at higher concentrations (above 10 ppm[72]as a control, 5FPE-NTCDI with PMMA as dielectric layer was also exposed to 0.5 ppm NH_3. After 5minutes' exposure, the 5FPE-

NTCDI/PMMA devices only gave 1% current increase, while 5FPE-NTCDI/SHP device give more than 5% current increase, a much higher response (Figure 40). This result clearly demonstrated this SHP-OFET is very promising for highly sensitive, flexible, printable and low-voltage operable OFET sensors.

2.4.5 Conclusion

In conclusion we have developed a self-healing dielectric polymer, which can aid in the healing any damage to the conductive gate layer. Additional demonstration of the enhanced ammonia sensing capabilities of self-healing OFETs brings us a step closer to our ultimate goal of developing a bistable circuit.

Acknowledgements

We would like to acknowledge primary funding from the Flextech Alliance. The dielectric property study was supported by the National Science Foundation, Division of Materials Research, Grant Number 1005398.

We would specially like to thank Dr. Wieguo Huang for polymer mixture design, which made it possible to conduct this study.

References

1. Brautbar, N., Wu, M. P. & Richter, E. D. Chronic ammonia inhalation and interstitial pulmonary fibrosis: a case report and review of the literature. *Arch. Environ. Health* **58,** 592–596 (2003).

2. Timmer, B., Olthuis, W. & Berg, A. Van Den. Ammonia sensors and their applications—a review. *Sensors Actuators B Chem.* **107,** 666–677 (2005).

3. Markovics, A. & Kovacs, B. Fabrication of optical chemical ammonia sensors using anodized alumina supports and sol-gel method. *Talanta* **109,** 101–106 (2013).

4. Li, L. *et al.* High performance field-effect ammonia sensors based on a structured ultrathin organic semiconductor film. *Adv. Mater.* **25,** 3419–3425 (2013).

5. Huang, W., Yu, J., Yu, X. & Shi, W. Polymer dielectric layer functionality in organic field-effect transistor based ammonia gas sensor. *Org. Electron. physics, Mater. Appl.* **14,** 3453–3459 (2013).

6. Yu, X. *et al.* Flexible spray-coated TIPS-pentacene organic thin-film transistors as ammonia gas sensors. *J. Mater. Chem. C* **1,** 6532–6535 (2013).

7. Tiwari, S. *et al.* Poly-3-hexylthiophene based organic field-effect transistor: Detection of low concentration of ammonia. *Sensors Actuators B Chem.* **171-172,** 962–968 (2012).

8. Torsi, L. *et al.* A sensitivity-enhanced field-effect chiral sensor. *Nat. Mater.* **7,** 412–417 (2008).

9. Huang, Y., Fu, L., Zou, W., Zhang, F. & Wei, Z. Ammonia sensory properties based on single-crystalline micro/nanostructures of perylenediimide derivatives: Core-substituted effect. *J. Phys. Chem. C* **115,** 10399–10404 (2011).

10. Bouvet, M., Xiong, H. & Parra, V. Molecular semiconductor-doped insulator (MSDI) heterojunctions: Oligothiophene/bisphtalocyanine (LuPc2) and perylene/bisphthalocyanine as new structures for gas sensing. *Sensors Actuators, B Chem.* **145,** 501–506 (2010).

11. Chen, Y. *et al.* Enhanced chemosensing of ammonia based on the novel molecular semiconductor-doped insulator (MSDI) heterojunctions. *Sensors Actuators, B Chem.* **155,** 165–173 (2011).

12. Zan, H.-W. *et al.* Room-temperature-operated sensitive hybrid gas sensor based on amorphous indium gallium zinc oxide thin-film transistors. *Appl. Phys. Lett.* **98,** 253503 (2011).

13. Reetz, M. T., Huff, J. & Goddard, R. Borylated lyxofuranosides as selective host molecules for amines. *Tetrahedron Lett.* **35,** 2521–2524 (1994).

14. Nozaki, K., Tsutsumi, T. & Takaya, H. Selective Binding of Diamines to a Chiral Lewis Acid with Two Boron Centers. *J. Org. Chem.* **60,** 6668–6669 (1995).

15. Ziessel, R. Convenient Synthesis of Green Diisoindolodithienylpyrromethene – Dialkynyl Borane Dyes Se. *Org. Lett.* 8–11 (2007). doi:10.1021/ol0627404

16. Zhang, X. F., Liu, X. L., Lu, R., Zhang, H. J. & Gong, P. Fast detection of organic amine vapors based on fluorescent nanofibrils fabricated from triphenylamine functionalized beta-diketone-boron difluoride. *J. Mater. Chem.* **22,** 1167–1172 (2012).

17. Wanglee, Y. J. *et al.* Borane-induced dehydration of silica and the ensuing water-catalyzed grafting of $B(C_6F_5)_3$ to give a supported, single-site lewis acid, $\equiv SiOB(C_6F_5)_2$. *J. Am. Chem. Soc.* **134,** 355–366 (2012).

18. Watson, I. D. G., Styler, S. A. & Yudin, A. K. Unusual Selectivity of Unprotected Aziridines in Palladium-Catalyzed Allylic Amination Enables Facile Preparation of Branched Aziridines. *J. Am. Chem. Soc.* **126,** 5086–5087 (2004).

19. Kawabe, M., Murata, M. & Soga, K. Syndiospecific living polymerization of 4-methylstyrene with tris-(pentafluorophenyl)borane / trioctylaluminium catalytic system. *Macromol. Rapid Commun* **20,** 569–572 (1999).

20. Mountford, A. J. *et al.* Intra- and intermolecular N-H...F-C hydrogen-bonding interactions in amine adducts of tris(pentafluorophenyl)borane and -alane. *Inorg. Chem.* **44,** 5921–5933 (2005).

21. Park, J. *et al.* Ambient induced degradation and chemically activated recovery in copper phthalocyanine thin film transistors. *J. Appl. Phys.* **106,** 2–10 (2009).

22. Bohrer, F. I. *et al.* Comparative gas sensing in cobalt, nickel, copper, zinc, and metal-free phthalocyanine chemiresistors. *J. Am. Chem. Soc.* **131,** 478–485 (2009).

23. Bohrer, F. I. *et al.* Selective detection of vapor phase hydrogen peroxide with phthalocyanine chemiresistors. *J. Am. Chem. Soc.* **130,** 3712–3713 (2008).

24. Saverio, A. Di *et al.* Oxygen-Bridged Borate Anions from Tris(pentafluorophenyl) borane : **44,** 5030–5041 (2005).

25. Baum E A, Lewis T J, T. R. The lateral motion of charge on thin films of polyethylene terephthalate. *J.Phys.D* **11,** 963–977 (1978).

26. Baum. E A, Lewis T J, T. . Decay of electrical charge on polyethylene f i l m s. *J.Phys.D* **10,** 487–497 (1977).

27. Herous, L., Remadnia, M., Kachi, M. & Nemamcha, M. Decay of Electrical Charges on Polyethylene Terephthalate Surface. **2,** 87–90 (2009).

28. Herous, L., Nemamcha, M., Remadnia, M. & Dascalescu, L. Factors that influence the surface potential decay on a thin film of polyethylene terephthalate (PET). *J. Electrostat.* **67,** 198–202 (2009).

29. Mizutani. T, OoMura.T, I. M. Surface Potential Decay in Polyethylene. *Jpn. J. Appl. Phys.* **20,** 855–859 (1981).

30. Tai, L. S., Wong, Y. W., Poon, Y. M. & Shin, F. G. Characteristics of Corona-Charged PET Sandwich Electrets. *Mater. Sci. Forum* **480-481,** 123–128

(2005).

31. Viraneva, a., Yovcheva, T., Hristov, M. & Mekishev, G. Influence of gas media on the stability of corona charged polyethylenterephtalate films stored at low pressure. *IEEE Trans. Dielectr. Electr. Insul.* **19,** 1132–1136 (2012).

32. Xu, Z., Zhang, L. & Chen, G. Decay of electric charge on corona charged polyethylene. *J. Phys. D. Appl. Phys.* **40,** 7085–7089 (2007).

33. Zhong-fu, X. & Guo-mao, Y. Charge Dynamics in Mylar Films Corona-charged at Various Temper at ures. **2,** 702–707 (1992).

34. Akinwande, A. I., Member, S., Wang, A., Kymissis, I. & Bulovic, V. Engineering Density of Semiconductor-Dielectric Interface States to Modulate Threshold Voltage in OFETs. **53,** 9–13 (2006).

35. Zhong, H. *et al.* Air-Stable and High-Mobility n-Channel Organic Transistors Based on Small-Molecule / Polymer Semiconducting Blends. 3205–3211 (2012). doi:10.1002/adma.201200859

36. Takahashi, M., Masui, K., Sekiguchi, H. & Kobayashi, N. Palladium-Catalyzed C - H Homocoupling of Bromothiophene Derivatives and Synthetic Application to Well-Defined Oligothiophenes. 10930–10933 (2006).

37. Guo, X., Puniredd, S. R., Baumgarten, M., Pisula, W. & Müllen, K. Benzotrithiophene-based donor-acceptor copolymers with distinct supramolecular organizations. *J. Am. Chem. Soc.* **134,** 8404–8407 (2012).

38. Deshmukh, K. D., Reuter, K., Kempa, H., West, J. E. & Katz, H. E. Tuning of threshold voltage in organic field-effect transistors with hydrophobic gate dielectric using monoenergetic low-energy electron beams and triode corona. *Appl. Phys. Lett.* **95,** 113307 (2009).

39. Wang, A., Kymissis, I., Bulović, V. & Akinwande, A. I. Tunable threshold voltage and flatband voltage in pentacene field effect transistors. *Appl. Phys. Lett.* **89,** 112109 (2006).

40. Molinie, P. Charge injection in corona-charged polymeric films : potential decay and current measurements. **45,** 265–273 (1999).

41. Batra, I. P. Discharge Characteristics of Photoconducting Insulators. *J. Appl. Phys.* **41,** 3416–3422 (1970).

42. Physique, L. De & Yvette, G.-. On the Natural Decay. *phys.stat.sol.* **94,** 289–298 (1986).

43. Molinie, P; Goldman,M; Gatellet, J. Surface potential decay on corona-charged epoxy samples due to polarization processes. *J.Phys.D* **28,** 1601–1610 (1995).

44. H, B. Von. Interpretation of surface potential kinetics in HDPE by a trapping model. *J.Phys.D:Appl.Phys* **18,** 1155–1170 (1985).

45. Qiu, X., Xia, Z. & Wang, F. The storage and its stability of space charge in poly(ethylene naphthalene-2,6-dicarboxylate). *Sci. China Ser. E Technol. Sci.* **49,** 621–628 (2006).

46. Tremblay, N. J., Jung, B. J., Breysse, P. & Katz, H. E. Digital Inverter Amine Sensing via Synergistic Responses by n and p Organic Semiconductors. *Adv. Funct. Mater.* **21,** 4314–4319 (2011).

47. Huang, W. *et al.* A High-Capacitance Salt-Free Dielectric for Self-Healable, Printable, and Flexible Organic Field Effect Transistors and Chemical Sensor. *Adv. Funct. Mater.* 3745–3755 (2015). doi:10.1002/adfm.201404228

48. Zheng, P. & McCarthy, T. J. A surprise from 1954: Siloxane equilibration is a simple, robust, and obvious polymer self-healing mechanism. *J. Am. Chem. Soc.* **134,** 2024–2027 (2012).

49. Tee, B. C.-K., Wang, C., Allen, R. & Bao, Z. An electrically and mechanically self-healing composite with pressure- and flexion-sensitive properties for electronic skin applications. *Nat. Nanotechnol.* **7,** 825–832 (2012).

50. Wang, C. *et al.* Self-healing chemistry enables the stable operation of silicon microparticle anodes for high-energy lithium-ion batteries. *Nat. Chem.* **5,** 1042–1048 (2013).

51. Toohey, K. S., Sottos, N. R., Lewis, J. A., Moore, J. S. & White, S. R. Self-healing materials with microvascular networks. *Nat. Mater.* **6,** 581–585 (2007).

52. Odom, S. A. *et al.* Restoration of conductivity with TTF-TCNQ charge-transfer salts. *Adv. Funct. Mater.* **20,** 1721–1727 (2010).

53. Blaiszik, B. J. *et al.* Autonomic restoration of electrical conductivity. *Adv.*

Mater. **24,** 398–401 (2012).

54. Odom, S. A. *et al.* A self-healing conductive ink. *Adv. Mater.* **24,** 2578–2581 (2012).

55. Lu, C.-C., Lin, Y.-C., Yeh, C.-H., Huang, J.-C. & Chiu, P.-W. High Mobility Flexible GrapheneField-Effect Transistors with Self-Healing Gate Dielectrics. *ACS Nano* **6,** 4469–4474 (2012).

56. Dumas, C., El Zein, R., Dallaporta, H. & Charrier, A. M. Autonomic self-healing lipid monolayer: A new class of ultrathin dielectric. *Langmuir* **27,** 13643–13647 (2011).

57. Li, J., Sun, Z. & Yan, F. Solution processable low-voltage organic thin film transistors with high-k relaxor ferroelectric polymer as gate insulator. *Adv. Mater.* **24,** 88–93 (2012).

58. Hwang, S. K. *et al.* High performance multi-level non-volatile polymer memory with solution-blended ferroelectric polymer/high-k insulators for low voltage operation. *Adv. Funct. Mater.* **23,** 5484–5493 (2013).

59. Baeg, K. J. *et al.* Remarkable enhancement of hole transport in top-Gated N-Type polymer field- Effect transistors by a high-K dielectric for ambipolar electronic circuits. *Adv. Mater.* **24,** 5433–5439 (2012).

60. Wang, C. *et al.* Thiol – ene Cross-Linked Polymer Gate Dielectrics for Low-Voltage Organic Thin-Film Transistors. **25,** 4806–4812 (2013).

61. Cho, J. H. *et al.* Printable ion-gel gate dielectrics for low-voltage polymer thin-film transistors on plastic. *Nat. Mater.* **7,** 900–906 (2008).

62. Pal, B. N., Dhar, B. M., See, K. C. & Katz, H. E. Solution-deposited sodium beta-alumina gate dielectrics for low-voltage and transparent field-effect transistors. *Nat. Mater.* **8,** 898–903 (2009).

63. Lee, K. H. *et al.* 'Cut and stick' rubbery ion gels as high capacitance gate dielectrics. *Adv. Mater.* **24,** 4457–4462 (2012).

64. Joshi, G. & Pawde, S. M. Effect of molecular weight on dielectric properties of polyvinyl alcohol films. *J. Appl. Polym. Sci.* **102,** 1014–1016 (2006).

65. Ortiz, P. *et al.* High- *k* Organic, Inorganic, and Hybrid Dielectrics for Low-Voltage Organic Field-Effect Transistors. *Chem. Rev.* **110,** 205–239 (2010).

66. Huang, W., Shi, W., Han, S. & Yu, J. Hysteresis mechanism and control in pentacene organic field-effect transistors with polymer dielectric. *AIP Adv.* **3,** 052122 (2013).

67. Huang, W. *et al.* Label-free brain injury biomarker detection based on highly sensitive large area organic thin film transistor with hybrid coupling layer. *Chem. Sci.* **5,** 416–426 (2014).

68. Glowacki, E. D. *et al.* Hydrogen-bonded semiconducting pigments for air-stable field-effect transistors. *Adv. Mater.* **25,** 1563–1569 (2013).

69. Salinas, M. *et al.* The relationship between threshold voltage and dipolar

character of self-assembled monolayers in organic thin-film transistors. *J. Am. Chem. Soc.* **134,** 12648–12652 (2012).

70. Hardigree, J. F. M. *et al.* Reducing Leakage Currents in n-Channel Organic Field-Effect Transistors Using Molecular Dipole Mono layers on Nanoscale Oxides. *ACS Appl. Mater. Interfaces* **5,** 7025–7032 (2013).

71. Jeong, J. W. *et al.* The response characteristics of a gas sensor based on poly-3-hexylithiophene thin-film transistors. *Sensors Actuators B Chem.* **146,** 40–45 (2010).

72. Huang, W. *et al.* Diverse organic field-effect transistor sensor responses from two functionalized naphthalenetetracarboxylic diimides and copper phthalocyanine semiconductors distinguishable over a wide analyte range. *Adv. Funct. Mater.* **23,** 4094–4104 (2013).

Chapter 3

Ethylene Detection Based on Organic Field Effect Transistor With Palladium Particles As Receptor

3.1 Introduction

Ethylene is a small hydrocarbon with no odor or color. It occurs naturally as a plant hormone[1], it regulates various physiologically important events like germination[2], development or growth of the plant[1,3,4], flowering[5] and most importantly the ripening and subsequently senescence of the fruits post harvesting, especially climacteric fruits[1].

Specific pathways and role of ethylene in a plant's life cycle have been thoroughly investigated[6–8] considering the huge losses to the horticulture industry (millions of dollars) due to premature deterioration or over ripening of fruits and flowers during transportation and storage[9]. Ethylene is produced as a product of biosynthesis in plants; it permeates cells and triggers the fruit-ripening gene resulting in change in texture, color and taste of the fruits. Ripened fruit produces more ethylene which in turn induces more ripening and ultimately rotting of the fruits, by measuring the concentration of ethylene in the vicinity of the fruits so at a particular time, we can get an idea about the stage of ripeness of the fruit. We can theoretically even control the whole process by monitoring the ambient condition maintained in the storage units and thus increasing the shelf life of the fruits. By maintaining the

storage unit temperature close to 0°C, oxygen levels to 1 to 2%, high humidity nearing 92% and carbon dioxide levels to 200 ppm, fruits and vegetables can be successfully stored for weeks or even months[10]. While maintaining all the other parameters like oxygen level, temperature, humidity and carbon dioxide can be easy; developing a suitable sensing platform for ethylene is still a challenge owing to its small size and very limited physiochemical reactivity.

Existing technologies for sensing ethylene include photoacoustic spectroscopy, gas chromatography, metal-oxide based sensor, electrochemical sensor, electro-catalytic sensor, gas chromatography and non-dispersive spectroscopy[10–13]. All these present techniques are either too expensive at present, too bulky, require high temperature or do not have high sensitivity. Very recently, Swager *et al.* developed a reversible chemiresistive sensor based on single walled carbon nanotubes modified by a copper(I) complex to enhance the selectivity. The sensor could detect ethylene concentration ranging from 0.5 to 50 ppm, which is very encouraging[14]. Following this work Kathirvelam *et al.* published a multiwalled carbon nanotube sensor for ethylene on a flexible substrate. They report a sensitivity of 20 ppm and the response to be 10 times higher than the earlier single wall carbon nanotube sensor report[14], however no selectivity studies were reported[15]. Selectivity is a major concern for the carbon nanotube based

sensor devices due to various vander-waals interactions on carbon nanotube surface. Although Swager *et al.* included a selectivity study but several gases like Acetonitrile (100 ppm), tetrahydrofuran (200 ppm) and acetaldehyde (75ppm) had much higher response than the reported lower limit of 1 ppm for ethylene and almost equal response to 20 ppm ethylene response, which can be a major problem for practical application of these devices where a high selectivity is of utmost importance. Another major hindrance for the commercialization of carbon nanotube based sensor is the cost of production and separation of semiconducting and conductive nanotubes. A huge effort is being made by the research community to make carbon nanotubes a more economical and practically viable option for commercialization but until then we need a platform that is cost, and time efficient, compact, highly sensitive and selective. Over the past couple of years organic field effect transistors received a lot of attention for their sensing application due to their easy processibility, which makes them both time and cost efficient.

Here we report an OFET based sensing platform for ethylene sensing using CDT-3 as semiconductor and palladium particles as ethylene receptor. Interaction between transition metals and hydrogen atom has been studied a lot in order to come with a feasible solution for hydrogen storage, to be used as an alternative and renewable fuel[16–21]. There are reports indicating that hydrocarbons like ethylene[16–18] have an affinity to bind with transition metals

and form complexes, which then can be used to successfully store hydrogen. Palladium, platinum, zirconium and titanium have been proposed for this application[16]. We are just interested in using these metals as a receptor for ethylene. Considering the availability, stability, toxicity and the ease of handling, palladium was selected as the viable choice for acting as the ethylene receptor for the discussed ethylene sensor.

3.2 Experimental

3.2.1 Materials

Highly doped n type silicon used for device fabrication was bought from Si Tech. Palladium particles, copper phthalocyanine (CuPc) and cobalt phthalocyanine (CoPc), poly alpha methyl styrene, Chloro[1,3-bis(2,6-diisopropylphenyl)imidazol-2-ylidene]copper(I) and Phenanthroline)bis(triphenylphosphine)copper(I) nitrate dichloromethane were purchased from Sigma Aldrich. CDT-3 was generously supplied by Cambridge display technology; XC1360 (CAS number 530116-60-0) was donated by plextronics; poly(3,3‴-didodecylquaterthiophene (PQT-12) was synthesized in our group using standard procedure[22]. Ethylene gas with a defined concentration of 50 ppm and 100 ppm in dry nitrogen was purchased from PRAXAIR.

3.2.2 Device Preparation

Highly doped n type <100> silicon wafers with 300 nm silicon dioxide were diced into 1 inch by 1 inch pieces. The wafers were then cleaned using piranha solution

(3:1 of sulfuric acid: hydrogen peroxide) followed by sonication in acetone and then in isopropanol for 30 minutes. The wafers were dried using nitrogen gas flow. Gold electrodes (50 nm) were deposited through a shadow mask (channel width/length ratio approximately 308 (77000 μm /250 μm)) at a rate of 0.3 Å/s using physical vapor deposition. The pressure of the deposition chamber was maintained at $<5\times10^{-6}$ torr. Organic semiconductors were either spin coated (from a solution, 4mg/ml in chorobenzene for poly (3,3‴-didodecylquaterthiophene) (PQT-12) at 60°C and 9mg/ml in o-xylene for CDT-3 at 90°C (heated at least an hour prior to deposition)) or thermally deposited using physical vapor deposition (copper phthalocyanine (CuPc) and cobalt phthalocyanine (CoPc))

3.2.3 Measurements

Organic field effect geometry was used as a sensing platform (Figure 41). All the OFETs were measured using an Agilent 4155C semiconductor analyzer. A home-built, well-sealed chamber with a volume of 1300 ml was used for exposure experiments.

3.3 Results and Discussion

As ethylene is not a very strongly interactive analyte and can only affect the sensing membrane via delocalized double bond electrons in the structure ($CH_2 = CH_2$), we chose the organic semiconductors which should react strongly to an analyte with electron donating tendencies, for preliminary filtering. The list of potential semiconductors includes PQT-12 poly(3,3‴-didodecylquaterthiophene), copper phthalocyanine (CuPc), cobalt phthalocyanine (CoPc)), XC1360 and CDT-3. PQT-12

was chosen as it has been well established for sensing ammonia[23], which also has a lone pair of electrons. Copper and cobalt ions are known to form coordination complexes with ligands like ammonia; we wanted to exploit the possibility of

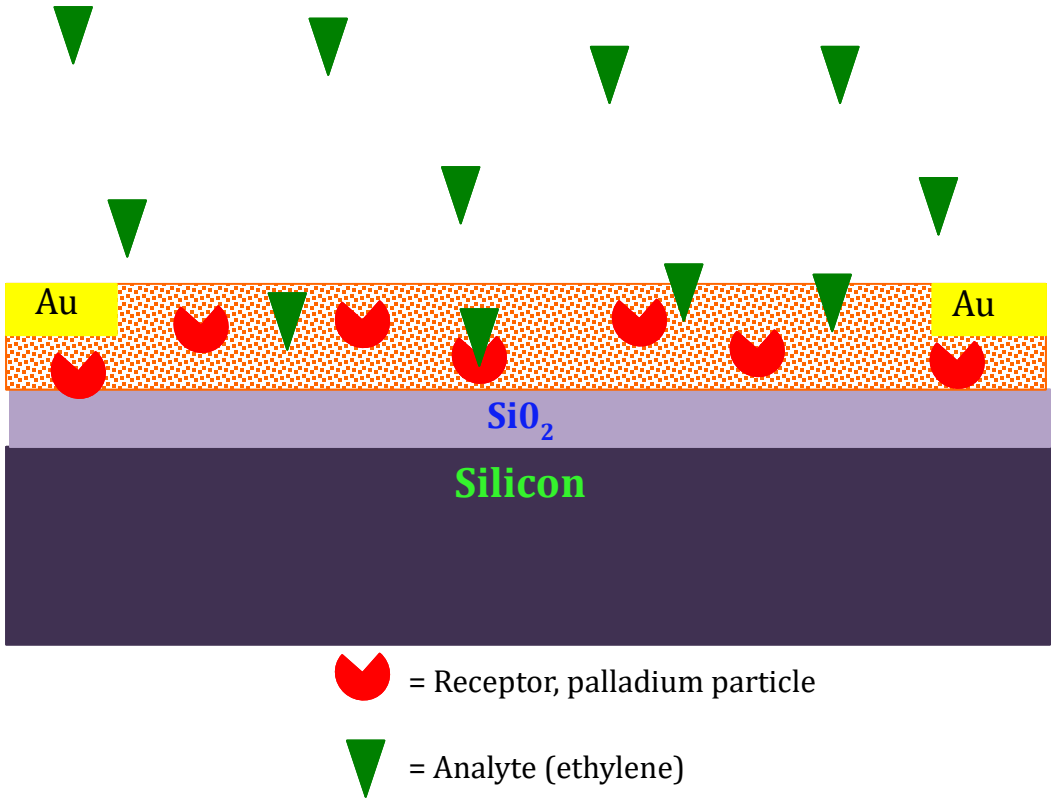

Figure 41 Schematic of an ethylene sensor.

ethylene being a potential ligand for these two metals by using copper phthalocyanine and cobalt phthalocyanine[24] (Figure 42) as active semiconductors. The transfer curves for PQT-12, CuPc, CoPc, CDT-3 are shown in Figure 43. The ethylene sensitivity was investigated by monitoring the percentage change in the drain current of the OFET devices. Table 3 summarizes the exposure experiments for 100 ppm of ethylene for 5 minutes.

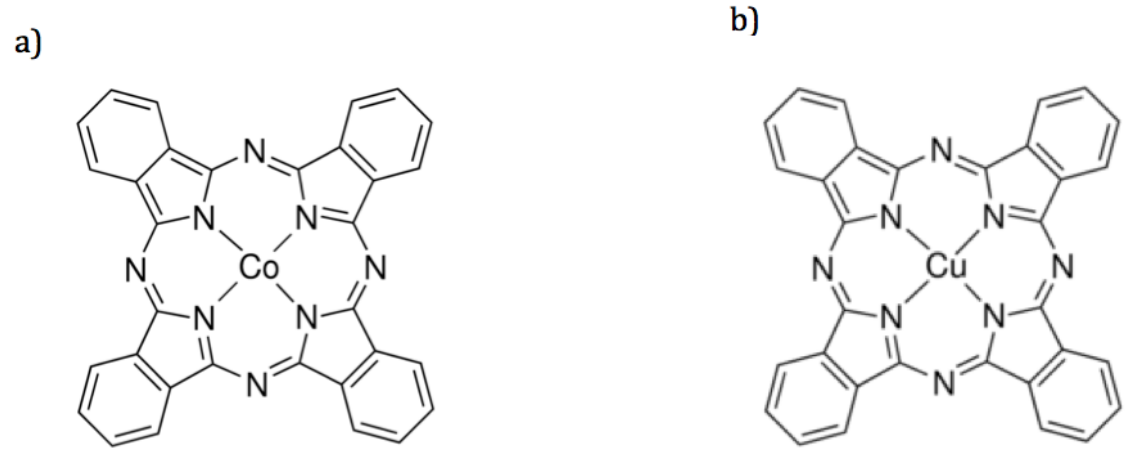

Figure 42 a) Chemical structure of cobalt phthalocyanine b) Chemical structure of copper phthalocyanine.

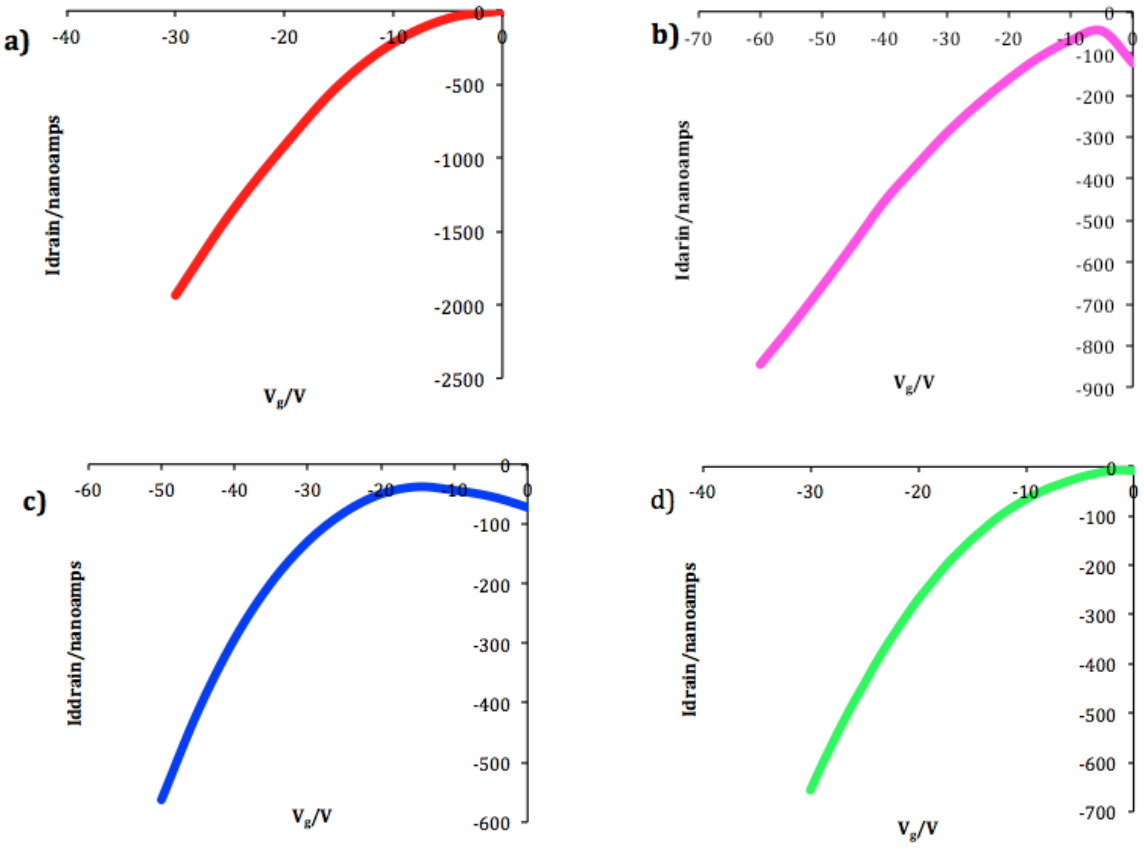

Figure 43 Transfer curve of a) CDT-3 b) PQT-12 c) CoPc d) CuPc.

Active material	% change in current after exposure to 100ppm ethylene for 5 minutes
PQT-12	15.31% decrease
PQT-12+Chloro[1,3-bis(2,6-diisopropylphenyl)imidazol-2-ylidene]copper(I) 10:1	19.6% decrease
CoPc	25.26% decrease
CuPc	21.17% decrease
XC1360	20.8% decrease
XC1360+(1,10-Phenanthroline)bis(triphenylphosphine)copper(I) nitrate dichloromethane adduct 95%, 10:1	13.48% decrease
CDT-3	22.46% decrease

Table 3 Summary of exposure experiments, 100 ppm ethylene exposure for 5 minutes.

CoPC gave the highest response of approximately 25.26% to 100ppm ethylene exposure for 5 min followed by 22.46% for CDT-3 and 21.17% for CuPC. PQT-12 gave a considerably low response of 15.31%. These responses can be attributed to the fact that cobalt and copper both have a tendency to form coordination complexes and so ethylene can interact with these compounds as a ligand. Ethylene acts as a trap for the positive charge carriers in the films and hence a decrease in the overall conductivity of the film was observed and this response was fully reversible. Ethylene is not a very strong ligand, so this interaction should be very temporary in nature leading to a reversible response. For PQT-12, the interaction must be only

physical adsorption, which justifies the lower responses.

As ethylene is known to have an affinity to form bond with Copper(1)complexes[14], Chloro[1,3-bis(2,6-diisopropylphenyl)imidazol-2-ylidene]copper(I) and Phenanthroline)bis(triphenylphosphine)copper(I) nitrate dichloromethane were added to PQT-12 and XC1360 films in order to introduce some kind of specific interaction between ethylene and the sensing membrane. While Chloro[1,3-bis(2,6-diisopropylphenyl)imidazol-2-ylidene]copper(I) increased the response of PQT-12 to 100 ppm Ethylene from 14% to 20%, Phenanthroline)bis(triphenylphosphine)copper(I) nitrate dichloromethane decreased the response of XC1360 from 20% to 13%. In case of the devices with a composite semiconductor film, interaction between the additive and the host film also plays a significant role along with the chemistry between the additive and the analyte in determining the affect of additive on the overall sensitivity of the device. For example in case of PQT-12 film the sensitivity of the device is increased due to the affinity of the additive for the analyte while for XC1360 films addition of Phenanthroline)bis(triphenylphosphine)copper(I) nitrate dichloromethane actually made the film more dense and as a result there was a decrease in the response.

We want to make a low cost ethylene sensor, which can be achieved by reducing the number of physical vapor deposited steps. Among the three highly sensitive organic semiconductor layers (Copc, CuPC and CDT-3), CDT-3 was the only solution prcocessible choice and hence it was selected for further development of this sensor platform. CDT-3 gave a 22% decrease in drain current upon exposure to 100-ppm ethylene for 5 minutes and 10% decrease in drain current on exposure to 50-ppm

ethylene for 5 minutes (Figure 44). Thus decreasing the ethylene concentration directly affects the % decrease in response.

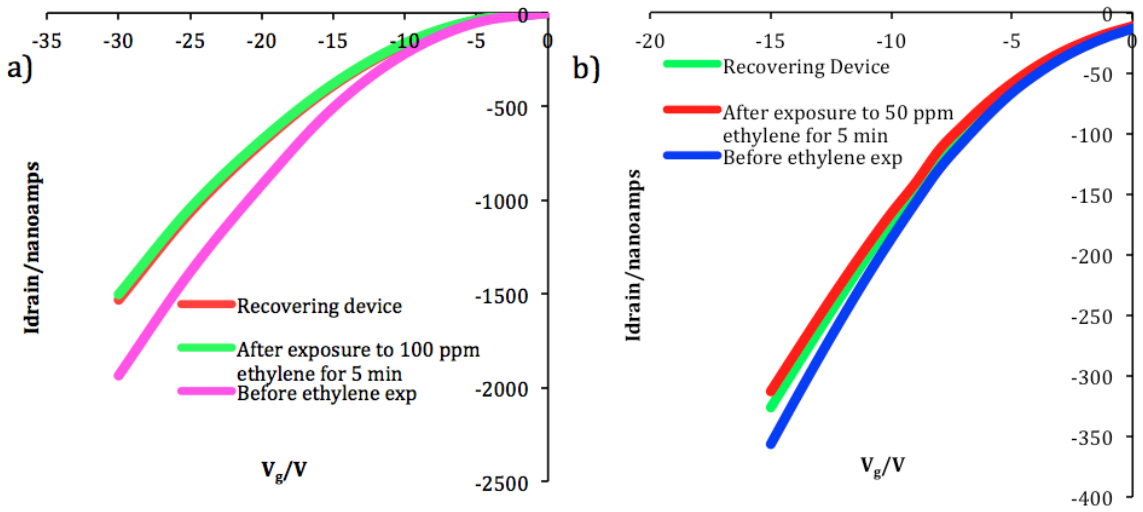

Figure 44 a) CDT-3, 100 ppm ethylene exposure, 22% decrease in current b) CDT-3, 50 ppm ethylene exposure, 10% decrease in current.

The sensor should be sensitive to sub-ppm level concentrations of ethylene in order to be useful at cold storages for fruits and vegetables. The simplest approach to increase the response of any gas sensor is to increase the interaction area of the sensitive film, which could be achieved by increasing the overall permeation of the gas molecules into the films, hence by changing the porosity and film morphology. There are reports stating that adding polystyrene increases the adsorption of ethylene molecules and thus results in an overall increase in the response to ethylene[14]. In order to investigate the influence of the film density and polystyrene for CDT-3 film, we reduced the solution concentration from 9nmg/ml to 4mg/ml and added 10% polystyrene to 9mg/ml CDT-3. The results are summarized Table 4.

Film	Processing	Effect of 50 ppm ethylene
CDT-3	4mg/ml, 2000 rpm	No change (<1%)
CDT-3+polystyrene (10%)	9mg/ml, 2000 rpm	Change <3%

Table 4 Summary of exposure experiments with different film morphologies.

These results suggest that on decreasing the concentration of the film solution, we decreased the over all reactive centers for ethylene in the film, which in turn decreased the overall sensitivity of the device. Polystyrene might increase the adsorption of ethylene on its surface but it appeared to have made the CDT-3 film very dense for permeation of ethylene molecule, which translated into decrease of response to ethylene (from 10% decrease to <3% decrease in drain current).

Thus a very strong additive receptor is needed to trap the ethylene molecules successfully without compromising the porosity of the CDT-3 films. Researchers have shown that ethylene molecule attached to transition materials like palladium, titanium, nickel can be used for hydrogen storage[16–19,21] and ethylene forms a strong bond with these transition metals[16]. In a report by Durgun et.al binding between titanium and ethylene had been studied thoroughly[16]. The paper stated that a single Ti-atom could bond to an ethylene molecule to form $C_2 H_4$ Ti complex without any reaction energy. It was shown that it is in fact possible to attach two Ti atoms to a single ethylene molecule without any potential barrier. Both Ti atoms were closer to one of the carbon atom resulting in two different bonds. Bonding occurs due to hybridization of LUMO of ethylene and d orbital of Ti according to Dewar

cooardination[25]. The stability of this $C_2H_4Ti_2$ complex was investigated using normal mode analysis. They also reported a similar interaction between ethylene and other transition metals including Scandium, Titanium, Zirconium palladium and platinum.

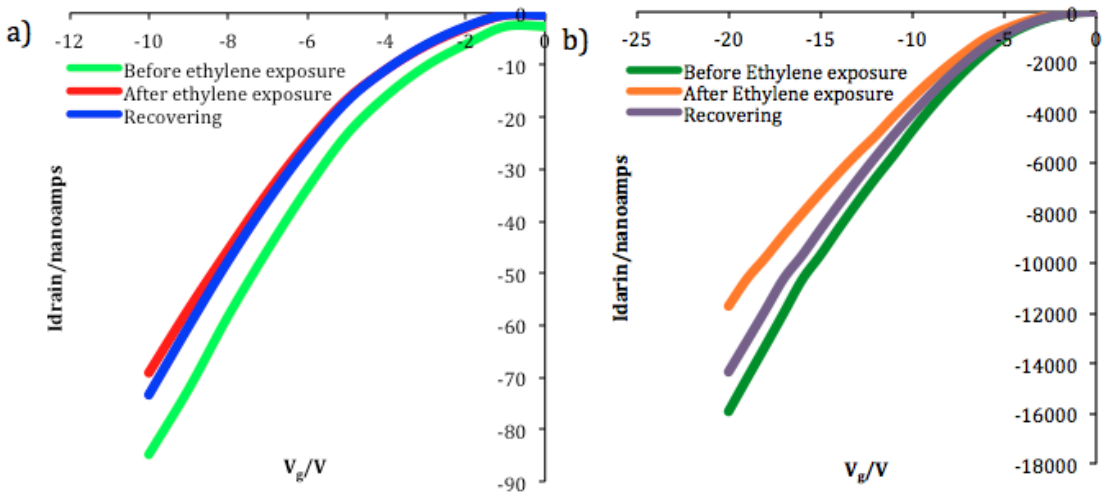

Figure 45 a) CDT-3 with 40% palladium particles, 18% decrease in drain current, 50 ppm ethylene exposure b) CDT-3 with 50% palladium particles, 27% decrease in drain current, 50 ppm ethylene.

Considering the practical limitations like stability under ambient condition and handling, palladium was chosen as the potential receptor for ethylene. Palladium particles (<1 micron diameter) were added to the semiconductor solution in the glove box. The mixture was then spin coated on the silicon substrates (with gold source and drain electrodes already patterned). Semiconductor films with 40 wt% palladium particles gave 18% decrease in drain current on exposure to 50 ppm ethylene for 5 minutes. Increasing the Wt% of palladium to 50% increased the response to 27%, Figure 45. On further increasing the wt% of palladium particles to 70% the semiconductor characteristics were lost completely. Increasing the wt% of

palladium particles beyond 50% led to a very high density of palladium particles resulting in formation of conductive pathways in the film.

Thus palladium can be successful incorporated as a receptor for ethylene and 50wt% of palladium in a CDT-3 film can increase the sensitivity of the film by170 %.

3.4 Future Work

The end goal of this project is to increase the sensitivity of this platform to sub ppm level. Assuming that the response has almost a linear dependence on the gas concentration (considering that 50 ppm gave almost half the response of 100ppm) we can theoretically detect 10-25 ppm concentration of ethylene successfully using this ethylene sensor. Although we still need to confirm this experimentally.

To further increase the detection profile to the 1 ppm level concentration, we want to introduce porogenes in order to increase the porosity of the materials. Porogenes disintegrate into gaseous molecules and escape the film at a specific temperature, leaving behind pores in the film. We introduced Poly alpha methyl styrene as a potential porogene in the semiconductor film; sensitivity did not improve much (as the effective pore formation or dissociation of the polymer takes places between 160-200 ℃ and we were unable to heat the film to such a high temperature (considering the thermal stability of our organic semiconductor film)).

Tert-butyl phenyl carbonate and N-(tert-butoxy-carbonyloxy)-phthalimide, are two compounds which should disintegrate at temperature less than 100 ℃. We would like to use them as porogenes to increase the interactive surface area of the films.

Another important step for this sensor project is to conduct a selectivity study; although palladium chemistry with ethylene is fairly selective, validation is still required for our theory.

Acknowledgements

We would like to thank Cambridge Display Technology for supporting this work and for generously donating CDT-3 polymer.

Note: For more information about CDT-3, We would advise to contact Cambridge Display Technology directly. CDT-3 is a research polymer donated to JHU under a non-disclosure agreement.

References

1. Abeles, FB, Page W.Morgan, M. E. S. *Ethylene in plant biology.* (Academic Press, San Diego, 1973).
2. Kepczynski, J. & Kepczynska, E. Ethylene in seed dormancy and germination. *Physiol. Plant.* **101,** 720–726 (1997).
3. Jackson, M. B. & Osborne, D. J. Ethylene, the natural regulator of leaf abscission. *Nature* **225,** 1019–1022 (1970).
4. Burg, S. P. Ethylene in plant growth. *Proc. Natl. Acad. Sci. U. S. A.* **70,** 591–597 (1973).
5. Cooke, A. R. 2-Haloethanephosphonic acids as ethylene releasing agents for the induction of flowering in pineapples. *Nature* **218,** 974 – 975 (1968).
6. Guo, H. & Ecker, J. R. The ethylene signaling pathway: New insights. *Curr. Opin. Plant Biol.* **7,** 40–49 (2004).
7. Binder, B. M. The ethylene receptors: Complex perception for a simple gas. *Plant Sci.* **175,** 8–17 (2008).
8. Stepanova, A. N. & Alonso, J. M. Ethylene signaling and response: where different regulatory modules meet. *Curr. Opin. Plant Biol.* **12,** 548–555 (2009).
9. Galotto, M. & Ulloa, P. Effect of high-pressure food processing on the mass transfer properties of selected packaging materials. *Packag. Technol. Sci.* **23,** 253–266 (2010).
10. Ivanov, P. *et al.* Towards a micro-system for monitoring ethylene in warehouses. *Sensors Actuators, B Chem.* **111-112,** 63–70 (2005).
11. Santiago Cintrón, M., Green, O. & Burstyn, J. N. Ethylene sensing by silver(I)

salt-impregnated luminescent films. *Inorg. Chem.* **51,** 2737–2746 (2012).

12. Giberti, a. *et al.* Monitoring of ethylene for agro-alimentary applications and compensation of humidity effects. *Sensors Actuators, B Chem.* **103,** 272–276 (2004).
13. Janssen, S. *et al.* Ethylene detection in fruit supply chains. *Philos. Trans. R. Soc. A* **372,** 20130311, (2014).
14. Esser, B., Schnorr, J. M. & Swager, T. M. Selective detection of ethylene gas using carbon nanotube-based devices: Utility in determination of fruit ripeness. *Angew. Chemie - Int. Ed.* **51,** 5752–5756 (2012).
15. Kathirvelan, J. & Vijayaraghavan, R. Development of prototype laboratory setup for selective detection of ethylene based on multiwalled carbon nanotubes. *J. Sensors* **2014,** 1–6 (2014).
16. Durgun, E., Ciraci, S., Zhou, W. & Yildirim, T. Transition-metal-ethylene complexes as high-capacity hydrogen-storage media. *Phys. Rev. Lett.* **97,** 1–4 (2006).
17. Ma, L. J., Jia, J., Wu, H. S. & Ren, Y. Ti-η2-(C2H2) and HCC-TiH as high capacity hydrogen storage media. *Int. J. Hydrogen Energy* **38,** 16185–16192 (2013).
18. Ma, L.-J., Jia, J. & Wu, H.-S. Computational investigation of hydrogen storage on scandium–acetylene system. *Int. J. Hydrogen Energy* **40,** 420–428 (2015).
19. Valencia, H., Gil, A. & Frapper, G. Trends in the hydrogen activation and storage by adsorbed 3d transition metal atoms onto graphene and nanotube surfaces: A dft study and molecular orbital analysis. *J. Phys. Chem. C* **119,** 5506–5522 (2015).

20. Dong, H., Hou, T., Lee, S.-T. & Li, Y. New Ti-decorated B40 fullerene as a promising hydrogen storage material. *Sci. Rep.* **5,** 9952 (2015).

21. Meng, Y. *et al.* Two dimetallocenes with vanadium and chromium: Electronic structures and their promising application in hydrogen storage. *Int. J. Hydrogen Energy* **40,** 12047–12056 (2015).

22. Guo, X., Puniredd, S. R., Baumgarten, M., Pisula, W. & Müllen, K. Benzotrithiophene-based donor-acceptor copolymers with distinct supramolecular organizations. *J. Am. Chem. Soc.* **134,** 8404–8407 (2012).

23. Besar, K. *et al.* Printable ammonia sensor based on organic field effect transistor. *Org. Electron.* **15,** 3221–3230 (2014).

24. Huang, W. *et al.* Highly Sensitive NH 3 Detection Based on Organic Field-E ff ect Transistors with Tris(penta fl uorophenyl)borane as Receptor. **134,** 14650–14653 (2012).

25. Kubas, G. J. *Metal Dihydrogen and sigma-Bond Complexes*. (Kluwer Academic/ Plenum Publishing, New York, 2001).

Section 2

Part 1

Chapter 4

Glial Fibrillary Acidic Protein Detection Based on Highly Sensitive Large Area Organic Thin Film Transistor Sensor

4.1 Introduction

Glial fibrillary acidic protein (GFAP) is an astrocyte cytoskeletal protein identified as a circulating acute brain injury biomarker in children with sickle cell disease (SCD)[1,2], birth asphyxia[3–5], and extracorporeal membrane oxygenation support[6], and in adults with traumatic brain injury and stroke[7–11]. A unique and large group of patients at risk of brain injury during care are those requiring cardiopulmonary bypass for cardiac surgery and those having invasive vascular procedures. At least 30% of neonates after surgical repair of congenital heart disease will have MRI indicating new injury, predominately stroke[12,13]. Similarly, adults after percutaneous intravascular procedures have an average 13-24% incidence of new MRI-evidenced injury resulting in a potential yearly rate of 321,000-628,000 new cases[12,13]. Although the clinical circumstances and high-risk patient groups are well known and brain-specific biomarkers are being tested clinically, development of an electronic biosensor platform for acute brain injury biomarkers would fill an important clinical void with the ability to detect acute injury biomarkers such as GFAP in real time and dramatically increasing their utility. The state of the art and

traditional immunoassay methods include ELISA (enzyme-linked immunosorbent assay)[14,15], SPR (surface plasmon resonance) and microcantilevers[14,15], all of which provide high sensitivity. However, they are expensive, labor intensive, not point of care, impose excessive time delays, lack portability or are not label-free.

Organic thin film transistors (OTFTs) have gained considerable attention as a sensor platform in the last two decades[16–27]. They have been shown to detect a wide range of analytes, including gases (such as NH_3, NO_2, O_3, and ethylene) and chemicals associated with explosives (such as DNT and TNT)[28–30]. OTFTs have evolved as low cost, low power consumption, biocompatible, and real-time biomolecule sensor platforms with the ability to detect a variety of biomolecules including DNA, glucose, protein and telomerase[31–46]. Analytes can be identified either through the immobilization of a specific receptor or by introducing a specific detection layer on the OTFT surfaces. However, these detectors are still at an early stage, limited by low sensitivity (the limit of detection is around several micrograms per milliliter), while higher sensitivities were instead achieved by using large surface-to-volume ratio nanostructured or low dimensional non-molecular materials such as silicon nanowires[34,44,47], SnO_2 nanobelts[48], single-crystalline silicon[35], carbon nanotubes[49–53], and graphene[54]. The limitations on these approaches can include their cost and relatively arduous fabrication procedures. Also, because of the small fraction of the active sensing area in nanowire or nanobelt TFT devices, nonspecific binding on the device can reduce the detection speed and sensitivity[48]. For carbon nanotubes and graphene, attention to this point is needed to differentiate protein covalent attachment from physical adsorption, as carbon nanotubes have a natural affinity

for diverse proteins through hydrophobic and electrostatic interactions[55,56]. Also, the small active area in nanostructure sensors can lead to transport-limited response rates.

Therefore, it remains highly desirable to develop biosensors based on alternative materials, such as organic or other macroscopic thin films, to overcome these restrictions. Despite significant progress[31,32,37,39,40], these reported OTFTs lacked sufficient sensitivity to be practically useful for detection, and the specificity and target protein recognition ability of these bioelectronic noses were not investigated in detail against preferred controls.

In this work, we describe the development of a highly sensitive OTFT sensor platform for detecting low-concentration protein analytes in solution with a sensing area as large as 7 mm by 7 mm. By using a larger area device, specific binding occurring anywhere in this area contributes to the response. Furthermore, a new antibody immobilization method is introduced, giving high immobilization yield and maximal surface coverage, resulting in good sensitivity. We employed p-channel (pentacene) and n-channel (8-3 NTCDI) organic molecules as semiconductors. The incorporation of both p- and n-channel transistors in a single sensor chip would enable discrimination of possible electrical cross-talk and/or false-positive signals by correlating the response versus time from the two types of device elements[34], and could also be utilized to make a synergistic inverter sensor. Using GFAP as a model protein analyte, this sensor platform demonstrated excellent selectivity and recognition of target protein even in much more concentrated non-target protein backgrounds. Additionally, we investigate the origin of analyte solution responses

by conducting a number of control experiments, including some without semiconductor at all. The dose-response relationship yielded a Langmuir isotherm from which a reasonable affinity constant was calculated for the protein and antibody. Finally, this platform can be reused, adding to material and process efficiency and reducing cost. To the best of our knowledge, this is the most sensitive OTFT protein sensor yet reported, and also the first demonstration of the expected opposite current responses by p- and n-channel semiconductors to the same protein.

4.2 Experimental Section

4.2.1 Materials and Device Design.

All materials were purchased from Sigma-Aldrich and used without further purification unless otherwise noted. 8-3 NTCDI was synthesized according to previous literature[57,58]. Glial Fibrillary Acidic Protein (GFAP) was purchased from EMD Biosciences, and anti-GFAP (SMI-26R) was purchased from Covance. Highly n-doped <100> silicon wafers with 75 nm thermally grown oxide were diced into 1 in. by 1 in. substrates, cleaned with piranha solution *(Caution--corrosive!)*, sonicated in acetone and isopropanol, and then dried by forced nitrogen gas. Substrates were further dried by 100 °C vacuum annealing for 20 minutes prior to a 2-hour exposure to hexamethyldisilazane (HMDS) vapor at 110 °C in a loosely sealed vessel. Pentacene (triple sublimed) or 8-3 NTCDI (triple sublimed) was then thermally evaporated directly onto HMDS- treated substrates with a thickness of 50 nm at a rate of 0.3 Å/s, substrate temperature during the deposition was held constant at 80

°C. The deposition chamber pressure was $<5\times10^{-6}$ Torr. Following this, gold electrodes (50 nm) were thermally vapor-deposited through an interdigitation mask (as show in Figure S1, channel width/length (77000 μm /250 μm)) at 0.3 Å/s. 20nm tetratetracontane was then thermally evaporated on Au electrodes to protect electrodes against any trace amount of buffer solution that may penetrate through the CYTOP layer. CYTOP (9% weight, Bellex International Corporation) was spin-coated on device surfaces with a thickness of 200 ± 20 nm, and annealed at 50 °C for 15 minutes under nitrogen atmosphere. 16 nm tetratetracontane was then thermally evaporated onto the CYTOP layer to fill any residual pinholes in the CYTOP film; furthermore, this tetratetracontane layer also functioned as an adhesive layer for the following N-Hydroxysuccinimide (NHS) treated PS-*block*-PAA (Poly(styrene)-*block*-poly(acrylic acid)) layer. The carboxylic acid groups of PS-*block*-PAA were activated by adding 20 mg N-(3-dimethylaminopropyl)-N′-ethylcarbodiimide hydrochloride (EDC) into the PS-*block*-PAA solution (10mg/mL in mix solvent of 0.6 mL anhydrous dichloromethane and 0.4 mL anhydrous N, N'-dimethylformamide), and after stirring at room temperature for 1 hour, 10 mg N-hydroxysuccinimide (NHS) was added to the mixture, with continued stirring at room temperature for another 6 hours. The resulting mixture was spin-coated on the tetratetracontane layer at a speed of 3000 rpm for 120 seconds. Then the device surface was dipped into DI water for 5 minutes to remove excess EDC and NHS, and dried with gentle nitrogen flow, repeating this dip-dry cycle 5 times to make sure all the excess EDC and NHS were completely removed. The resulting PS-block-PAA layer thickness was 20 ± 5 nm. All the OTFTs were characterized using an Agilent

4155C semiconductor analyzer. Perfluorodecalin was used to remove CYTOP at certain areas to access the gold electrodes for measurement[59]. Solutions to which responses were recorded, or which were used for rinsing, were introduced onto devices as 100 μL aliquots via a micropipette, and withdrawn either by micropipette or tissue paper absorption.

4.2.2 Antibody Immobilization

Anti-GFAP was covalently attached to the activated PS-*block*-PAA surface from a 6.6 μM anti-GFAP PBS solution for 6 hours at room temperature, and then gently rinsed with PBS to remove any non-covalently bound materials. Additionally, ethanolamine solution (5% volume in PBS) was then dropped on the device surface and allowed to react for another 6 hours to block any activated carboxylic groups that did not already react with the anti-GFAP. Finally, the device surface was gently rinsed 5 times to remove excess ethanolamine solution. As a control experiment, OFET devices without anti-GFAP were prepared by reacting ethanolamine solution (5% volume in PBS) with NHS treated PS-*block*-PAA surfaces for 6 hours at room temperature. To avoid water evaporation and contamination, the samples were maintained in a humid bacteria-free chamber during the reactions.

GFAP Information The molecular weight of GFAP is about 50 kDa, and its isoelectric point (PI point) is 5.4. The charge number at pH 7.4 is -13.

GFAP Sequence: MERRRITSAA RRSYVSSGEM MVGGLAPGRR LGPGTRLSLA RMPPPLPTRV DFSLAGALNA GFKETRASER AEMMELNDRF ASYIEKVRFL EQQNKALAAE LNQLRAKEPT KLADVYQAEL RELRLRLDQL TANSARLEVE

RDNLAQDLAT VRQKLQDETN LRLEAENNLA AYRQEADEAT LARLDLERKI ESLEEEIRFL RKIHEEEVRE LQEQLARQQV HVELDVAKPD LTAALKEIRT QYEAMASSNM HEAEEWYRSK FADLTDAAAR NAELLRQAKH EANDYRRQLQ SLTCDLESLR GTNESLERQM REQEERHVRE AASYQEALAR LEEEGQSLKD EMARHLQEYQ DLLNVKLALD IEIATYRKLL EGEENRITIP VQTFSNLQIR ETSLDTKSVS EGHLKRNIVV KTVEMRDGEV IKESKQEHKD VM

4.3 Results and Discussion

4.3.1 Device Architecture and Top Dielectric

Pentacene and 8-3 NTCDI (Figure 46) were selected as the semiconductors for sensor development due to their high mobility and stability, especially 8-3 NTCDI, which exhibits excellent stability and negligible bias stress in air compared to many other

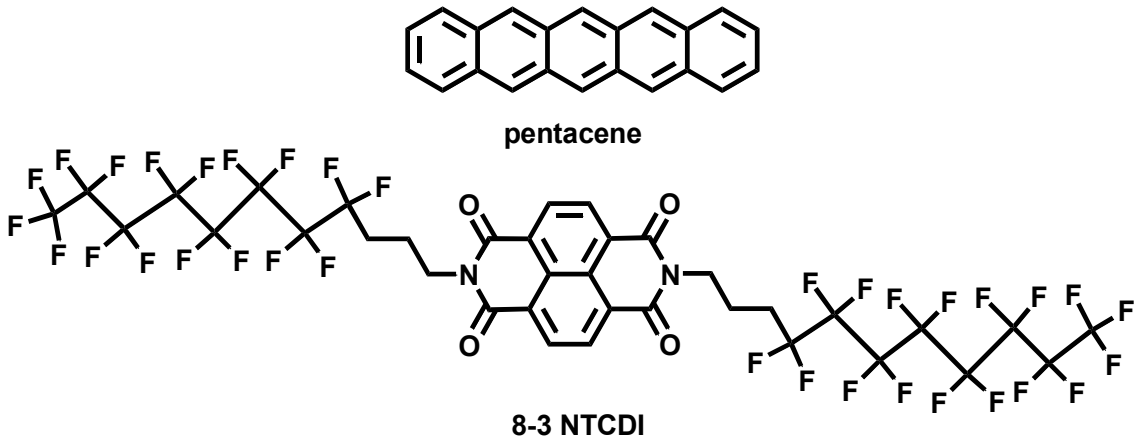

Figure 46 chemical structures of pentacene and 8-3 NTCDI

The device structures are shown inFigure 47; the interdigitated electrode mask for depositing Au source and drain electrodes is shown in Figure S1, of which the active

area is 7 mm by 7 mm. CYTOP was chosen as a passivation layer as well as top dielectric layer due to its excellent electrical and mechanical properties.

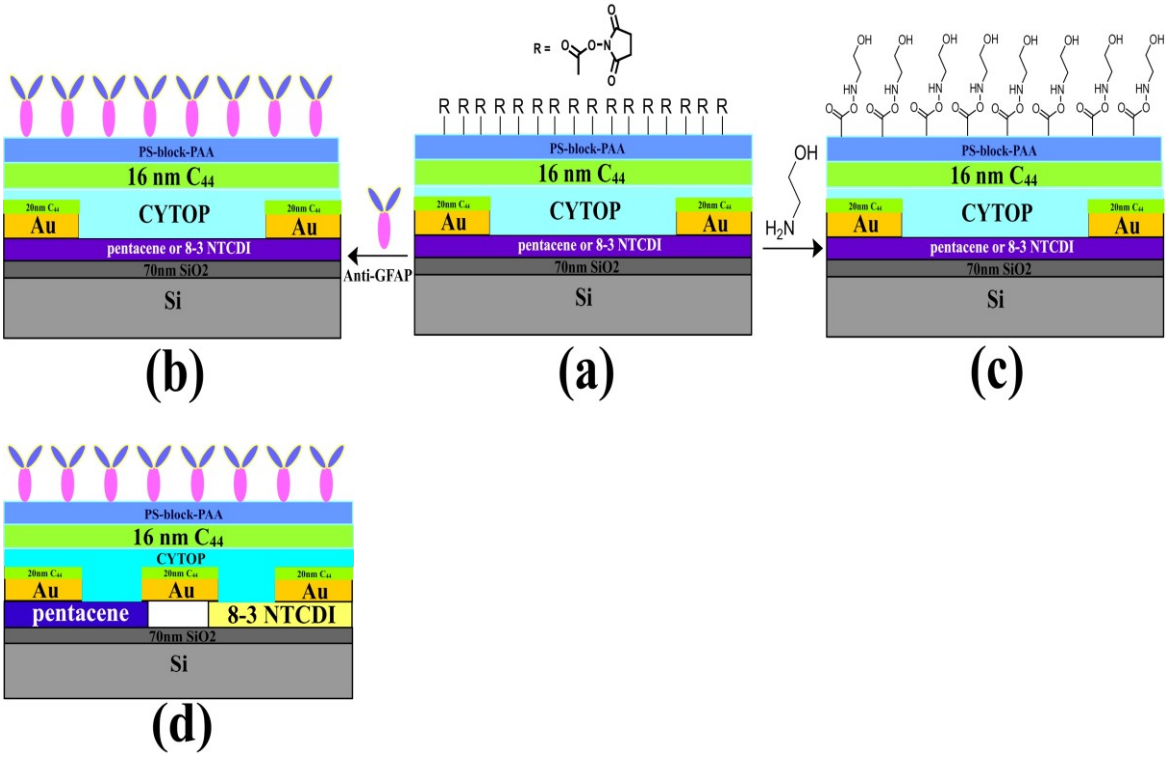

Figure 47 Device architecture of GFAP sensor: a) Activated carboxylate surface b) Anti-GFAP modified device; c) Hydroxyethylamide control device; d)Anti-GFAP modified inverter based on pentacene and 8-3 NTCDI.

Furthermore, it is easy to form a uniform thin layer by simple spin-coating and annealing at 50 °C for 15 minutes under nitrogen atmosphere. The electrical performances of the devices were not affected by spin-coating of the CYTOP layer as expected for fluoropolymers[59]. 16 nm tetratetracontane (C_{44}) was then deposited on the CYTOP.

We found multiple advantages to this fluoropolymer-hydrocarbon composite top dielectric layer. First, tetratetracontane can fill in the residual pinholes in the CYTOP

layer, reducing the penetration of buffer solution into semiconductor layers and decreasing leakage current[31]. The relative baseline current drift apparent from

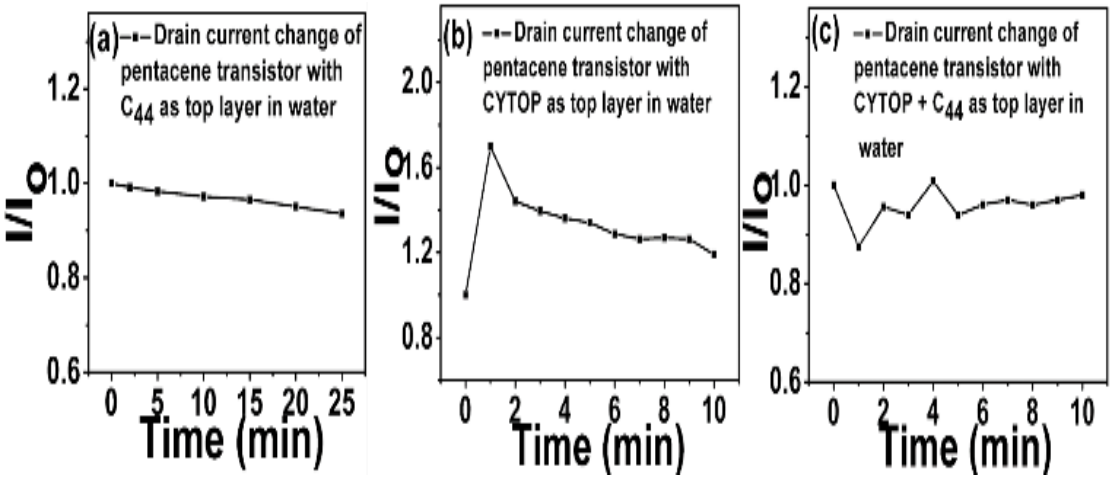

Figure 48 OTFT stability in water with different protective capacitive coupling layers**.**

the data of the control experiments is an order of magnitude less than what had been previously reported in a related example[37]. The performance is also better than that of dielectric films containing only CYTOP. In fact, $C_{44}H_{90}$ itself forms an outstanding barrier against water if it is thick enough. Figure 48 illustrates the excellent water stability conferred by 100 nm of sublimed $C_{44}H_{90}$ over 25 minutes However, the use of $C_{44}H_{90}$ as the only passive layer makes it difficult to spin coat the next overlying layer because $C_{44}H_{90}$ will be dissolved or delaminated during spin coating of activated PS-PAA, and cause damage to the layers (gold and semiconductors) under the $C_{44}H_{90}$. Figure 48 also shows the poorer stability conferred by CYTOP alone, which had the additional disadvantage of nonwettability of nonfluorous organic solutions, as discussed below.

Though nominally thicker, the CYTOP layer was apparently much more porous as

well. On the other hand, CYTOP prevents the dissolution of semiconductor and the delamination of electrodes during spin-coating of subsequent layers because of its solution orthogonality[59], while the spin-coating of a hydrocarbon directly on Au/pentacene caused this kind of degradation, and tetratetracontane alone did not prevent it. The combined top layer (CYTOP + $C_{44}H_{90}$) showed only slight drain current drift and excellent water stability (Figure 48) in the accumulation regime. Using atomic force microscopy (AFM), we could relate this to film morphology. As shown in Figure S2, the surface of the plain CYTOP film exhibits heterogeneous morphology, with a randomly arranged second phase embedded in the continuous amorphous film, which may lead to pinholes at the phase boundaries. After depositing a thin layer of $C_{44}H_{90}$, those randomly located features were filled and the surface morphology appears denser, leading to improved water stability. This composite layer is compatible with both the semiconductor layers below and the antibody coupling layer above, with no additional pretreatments needed before spin- coating steps. It is impossible to spin-coat NHS-treated PS-block- PAA on the highly fluorinated CYTOP layer alone.

We investigated the capacitance and coupling effect of the combined top layer. Figure S3 shows the relationship of the combined top layer capacitance with frequency; the capacitance value is stable over a wide frequency range, the value only starting to decrease when the frequency is above 10^5 Hz. There is a tradeoff between the capacitance and stability/leakage current in buffer solution, necessitating the optimization of the top layer thickness.

Finally, the anti-GFAP and PS-block-PAA layers can be effectively removed by rinsing the device surface with pure N,N'-dimethylformamide. Subsequent spin-coating of a new NHS treated PS-block-PAA layer would enable a different antibody to be attached to the device surface, making this sensor platform reusable. This cannot be done when the dielectric and receptor layers are covalently bound to the to the semiconductor.

4.3.2 Antibody Chemistry

Anti-GFAP was immobilized on the NHS-treated PS-*block*-PAA layer by EDC- and NHS-based bio-conjugation chemistry[31,32]. We introduce a different way to activate carboxylic acid groups on the device surface for subsequent antibody immobilizations. In previous literature, NHS activated surfaces were usually generated by in situ surface reaction of EDC–NHS with carboxylic acid in buffer solution. This method usually leads to low activation yield and low antibody immobilization yield[63]. Here, we first activated the carboxylic acid on PS-PAA copolymer (molar ratio of styrene: acrylic acid is about 2:1) by EDC–NHS in CH_2Cl_2–DMF mixed solvent, and then spin-coated activated PS-PAA on the device surface. This procedure gives 100% NHS activated surface, which leads high antibody immobilization yield and surface coverage. The successful immobilization of anti-GFAP on the device surface was confirmed by fluorescence experiments (Scheme S1), just as reported in previous literature[31,32,48]. The sensing experiments were conducted in 0.05x-diluted phosphate buffer solution (0.05 PBS) at room temperature. The isoelectric points (PI points) of anti-GFAP and GFAP are 5.7 and

5.4, respectively. The GFAP amino acid sequence is already shown in the Experimental section; both GFAP and the antibody are negatively charged at pH 7.4.

4.3.3 Transistor Characterization

The devices show excellent linear and saturation regime characteristics: for pentacene, a hole mobility of -0.07 ± 0.01 cm^2/Vs, an on/off ratio of 10^3 at V_g of -3 V and threshold voltage of -0.3± 0.1 V. Typical OTFT transfer and output curves are shown in Figure S4. In 0.05 PBS, both "on" and "off" current slightly increasd, indicating that the passive layer provides excellent protection for the semiconductor. For 8-3 NTCDI, an electron mobility of 0.03 ± 0.01 cm^2/Vs, an on/off ratio of 10^2 at V_g of 3 V and threshold voltage of 0± 0.1 V were obtained. In 0.05 PBS, "on" current decreased and "off" current increased but both stabilized rapidly (Figure S4). The different current change trends of pentacene and 8-3 NTCDI in 0.05 PBS would be consistent with opposite field effects of the buffer on p- and n-semiconductors. The sensor performance of the devices was evaluated under V_{ds} = -3 V and V_g = 0 to -3 V for pentacene and V_{ds} = 3 V and V_g = 0 to 3 V for 8-3 NTCDI; the drain current was recorded every 30 seconds. The fluoro-hydrocarbon protective layer acts as a second (top) gate dielectric; the final device is actually a dual-gate transistor. Thus, any selective binding of the target protein to surface-linked antibody occurring within the Debye screening length (double layer) should lead to charge density and distribution changes at the dielectric-electrolyte interface[35,64–67], thus changing the interfacial potential; all these changes will result in a corresponding change of the source-drain current. This is analogous to modulation of the channel current by changing the voltage applied to the top gate. For p-channel

transistors, binding of negatively charged species on the top gate will induce a net dipole pointing negative to positive toward the semiconductor, causing a drain current decrease, whereas opposite responses should be observed for an n-channel transistor[31,32]. A recent study pointed out that in some situations more sophisticated models rather than the classic electrochemical double layer would be required to assess the role of target position relative to the double layer, since large signals were observed even though the bound analyte was far from the surface. The new models should take into account the discreteness of the charges and the fundamentally three-dimensional nature of the double layer, as well as the conformational changes of the biomaterial layer upon interaction[35].

4.3.4 Responses to Proteins

The sensor performances of anti-GFAP modified OTFT devices were first determined by measuring drain current changes on exposure to varying concentrations of GFAP solution, as shown in Figure 49. There are several key features of this data. First, anti-GFAP-modified pentacene and 8-3 NTCDI devices exhibit opposite current change directions on exposure to GFAP solutions, consistent with the expectation that attached negatively charged species induce lower conductance in p-channel transistors and higher conductance in n-channel transistors. One possible mechanism is that negatively charged target proteins pull charge carriers (holes) away from the channel region for a p type transistor, and push charge carriers (electrons) toward the channel region for an n type transistor, as suggested in previous literature[31,68]. Another explanation, consistent with our data, is that the negatively charged protein drives positive counterions closer to the

coupling layer interface, creating a dipole projecting negative charge toward the medium and positive charge toward the OTFT.

Second, the responses show substantial signal dependence on protein concentration in a wide range (from 400ng/mL down to 0.8ng/mL), after reaching a stable current level at a certain concentration, further response is obtained by introducing a higher- GFAP-concentration solution. The magnitude and percentage of current changes at the same target protein concentration are higher than previous reported OTFT protein sensors[31,69,68], which indicates that this sensor platform shows higher sensitivity.

Third, the drain current changes only show slight reversibility on rinsing the device surface with pure 0.05 PBS, due to the strong specific antibody-antigen binding between anti-GFAP and GFAP[48], which makes GFAP very difficult to rinse off from device surfaces. Reversibility was greater at higher ionic strength. The recovered signal may indicate the part of the response generated by nonspecific adsorption and meta-stable binding between anti-GFAP and GFAP. From Figure 49 (b) and (d), by fitting the 0.05 PBS data with the Langmuir model (see Appendix A)[31,32], we can roughly estimate an affinity constant value for anti-GFAP and GFAP in this medium of $(1.2\pm0.5)*10^{10}$ (M^{-1}), a reasonable value for a protein and its antibody.

Fourth, according to the definition of limit of detection (LOD= R_{blank} + 3S, where R_{blank} is the blank response and S is the standard deviation of the response)[67,70], we obtained an estimated value of 1ng/mL (about 20 pM) for the LOD, the highest sensitivity ever reported for OTFT protein sensing to date. We further investigated

the selectivity using bovine serum albumin (BSA) as a representative non-target protein, for three reasons.

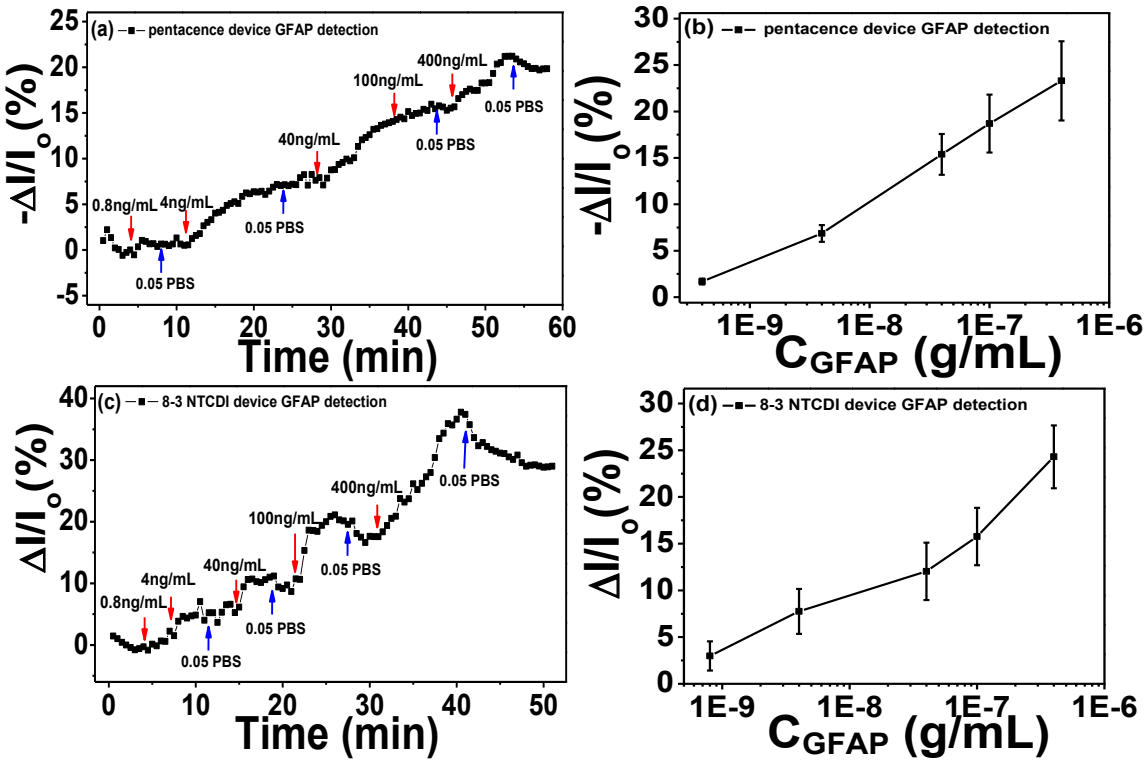

Figure 49 Drain current changes of anti-GFAP modified a) pentacene c) 8-3 NTCDI,devices vs time at different GFAP concentration. Drain current changes of anti-GFAP modified pentacene b) pentacene d) 8-3 NTCDI, devices versus GFAP concentrations.

First, BSA shares many similarities with human serum albumin (HSA) in bio-function and bio-chemical properties, making it a good model for a clinical interferent. Second, BSA is also negatively charged at pH 7.4, the charge number being -13, the same as the charge number of GFAP at pH 7.4. Third, the molecular weight difference between BSA and GFAP is small. Note that BSA was used as the analyte in a previous study[31]. As shown in Figure 50, for both anti-GFAP modified pentacene and 8-3 NTCDI devices, BSA buffer solution only generates random and inconsequential signals (comparable to device noise) when the concentration of BSA

is lower than 0.1mg/mL, far higher than the GFAP concentrations. Some reversible signal can be detected in 0.05 PBS by further increasing BSA concentration, though the signals generated by high concentration BSA can be completely recovered while GFAP signals only show slight recovery. This is the key difference between the GFAP signal and BSA signal in this medium; because the BSA signal is only generated by weak non-specific adsorption, it can be fully recovered by rinsing device surfaces with pure 0.05 PBS, whereas the GFAP signal is generated by strong specific binding between anti-GFAP and GFAP, which makes recovery difficult.

Moreover, the data in Figure 50 also indicate that anti-GFAP attached on the device surface not only provides binding sites for GFAP, but also prevents non-target protein from diffusing into the double layer (Debye screening length range). The Debye screening lengths λ_D at 0.05 PBS is about 3.3 nm[64], which is smaller than the size of anti-GFAP. As a result, anti-GFAP occupies most of the space of the double layer, inhibiting BSA diffusion except at very high BSA concentration gradients. This is also verified by the data in Figure 51, where all the responses were recorded using devices that were not functionalized with the anti-GFAP layer. As shown in Figure 47(c), ethanolamine instead of anti-GFAP was used to react with an NHS treated PS-*block*-PAA surface for 6 hours. The resulting -OH rich surface should not be able to specifically bind with any protein nor exhibit any selectivity. Furthermore, most of the volume that would be taken by a double layer is unoccupied, and any protein that moves into that volume would cause a reversible current change. As expected, in Figure 51, both GFAP and BSA are shown to generate reversible signals. BSA signals in Figure 51 are much higher than those in

Figure 50 at the same BSA concentrations, indicated that BSA could freely diffuse into the double layer region without being hindered by an anti-GFAP layer.

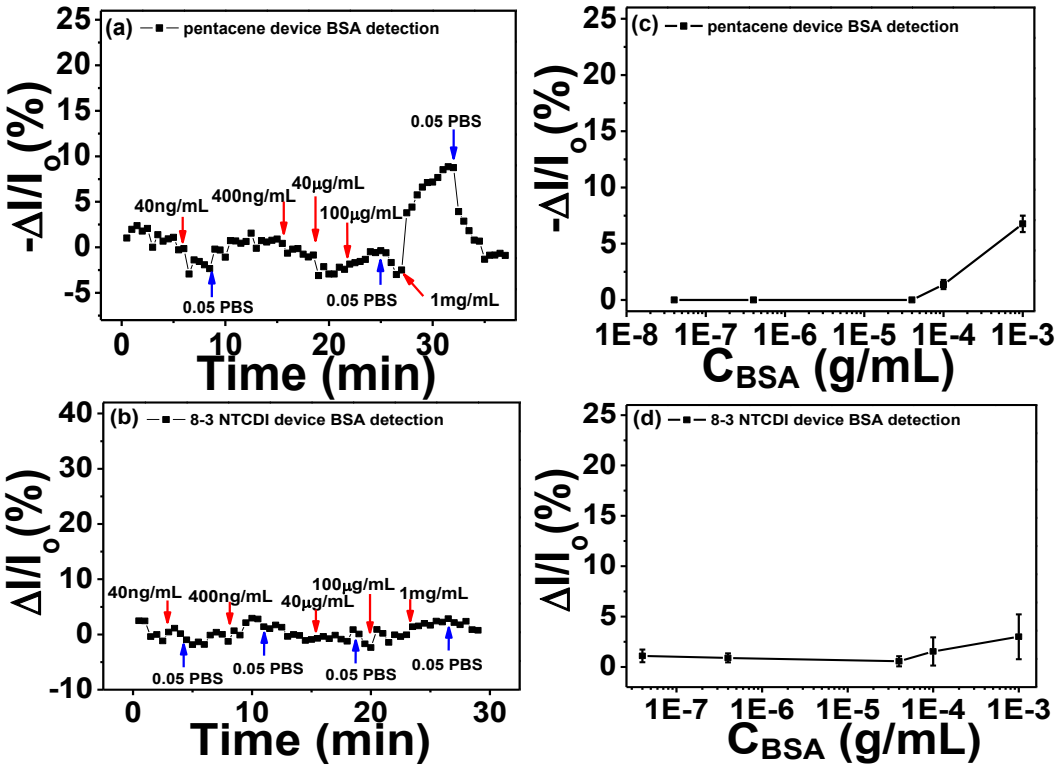

Figure 50 Drain current changes of anti-GFAP modified a) pentacene c) 8-3 NTCDI, device versus time at different BSA concentrations. Drain current changes of anti-GFAP modified b) pentacene d) 8-3 NTCDI, devices versus BSA concentrations.

At the higher BSA concentration, even more BSA diffuses into the double layer region and gives higher reversible responses. GFAP also shows non-specific adsorption responses; the signals of GFAP in Figure 49 are much higher than those in Figure 51 at the same GFAP concentrations because the strong affinity between anti-GFAP and GFAP drives more GFAP into the double layer region. All these results unambiguously illustrated that the anti-GFAP layer plays a critical role in generating the desired specific signals and reducing non-specific adsorption signals. In the

fourth set of experiments, we further investigated the sensor responses to GFAP in a mixture with highly concentrated non-target protein, to simulate a clinical situation where GFAP would exist in a mixture with other, more concentrated human serum albumin (HSA) and other proteins. The ability for sensors to recognize and bind highly diluted target protein from highly concentrated non-target protein is significantly important. As shown in Figure 52, a mixture of 1mg/mL BSA and 20ng/mL GFAP was used.

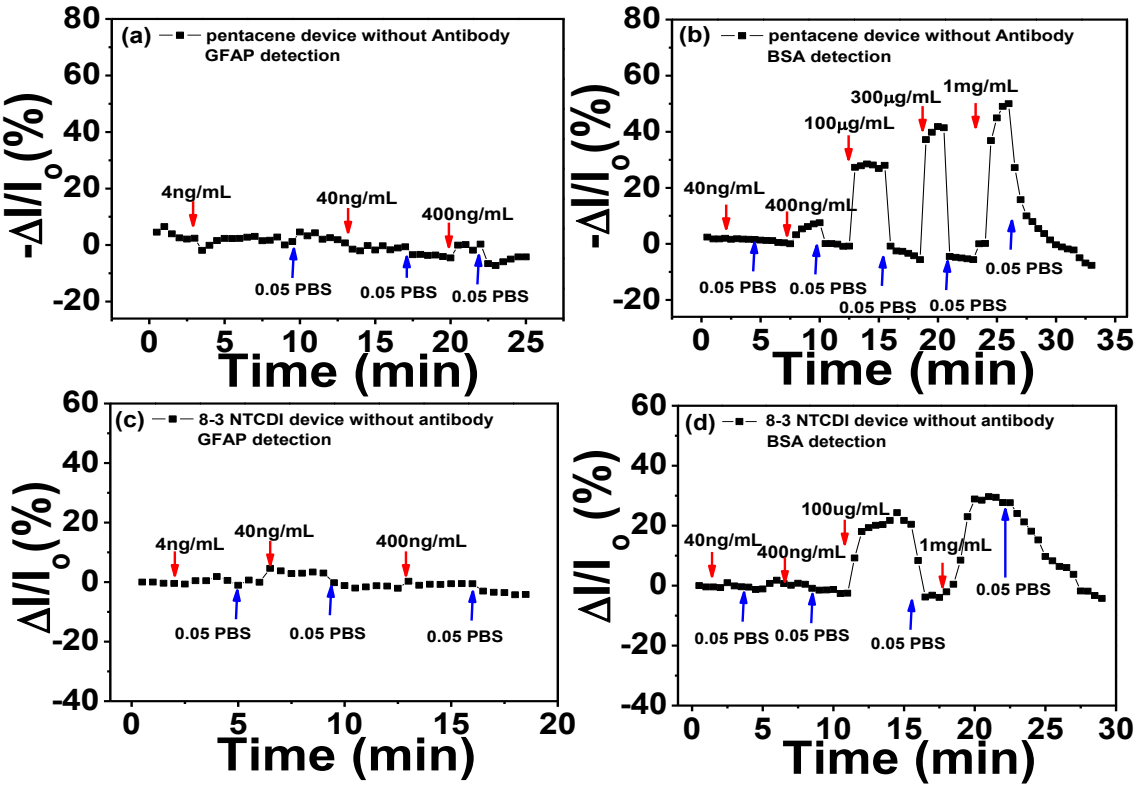

Figure 51 Drain current changes of pentacene (a,b) and 8-3 NTCDI (c,d) devices versus time at different GFAP and BSA concentrations, without anti-GFAP functionalized.

For pentacene, the drain current decreased then saturated, while for 8-3 NTCDI, the drain current increased then saturated. After rinsing with pure 0.05 PBS, both devices recovered but not completely back to the original current levels, with the

irreversible part of the responses attributed to GFAP according to the previous sensing results. Although the irreversible response magnitude is smaller than the responses to the same concentration of pure GFAP, the results are still very promising for real clinical application.

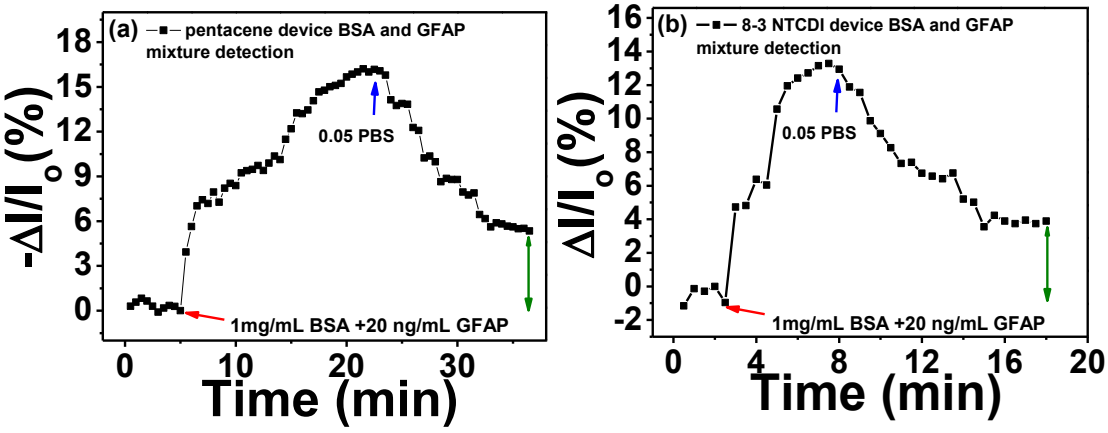

Figure 52 Drain current changes of anti-GFAP modified a) pentacene b) 8-3 NTCDI, devices versus time in 1mg/ml BSA and 20ng/ml GFAP mixture.

The net signal of anti-GFAP-GFAP specific binding can be preserved and identified after 0.05 PBS rinsing to reverse other non-specific and meta-stable signals. Furthermore, in a preliminary experiment, the response to 1% beef blood (in undiluted PBS) was less than the response to 50 nM GFAP in PBS.

Having complementary responses from pentacene and 8-3-NTCDI, we made a first attempt to obtain a voltage response from an inverter incorporating the two semiconductors, the structure of which is shown in Figure 47(d)[71]. The inverter electrical performances in air and in 0.05 PBS are shown in Figure S4. This inverter shows the proper characteristics in air (Vg sweep from 0 V to 6 V, V_{dd} = 3 V, V_s = 0V) with sharp switching behavior. After exposure to 0.05 PBS, output voltage slightly decreased to 2.8 V at Vg = 0 V and slightly increased to 0.4 V at Vg = 6 V. When

400ng/mL GFAP 0.05 PBS solution was introduced, the output V-Vg curve gradually shifted to the left and then saturated while output voltage slightly decreased to 2.68 V at Vg = 0 V. After rinsing with pure 0.05 PBS, the curve only slightly shifted back to the right, indicating irreversible anti GFAP-GFAP binding (Figure 53). No obvious shift occurred on introducing 1mg/mL BSA 0.05 PBS solution. This is the first indication that an inverter, or certainly an organic inverter, can respond to a protein. While the magnitude of the voltage shift is modest, the observation provides further evidence for the opposite current responses of p- and n-OTFTs to the same protein solution, and opens the door for improvement of this device architecture so that digital responses can be obtained.

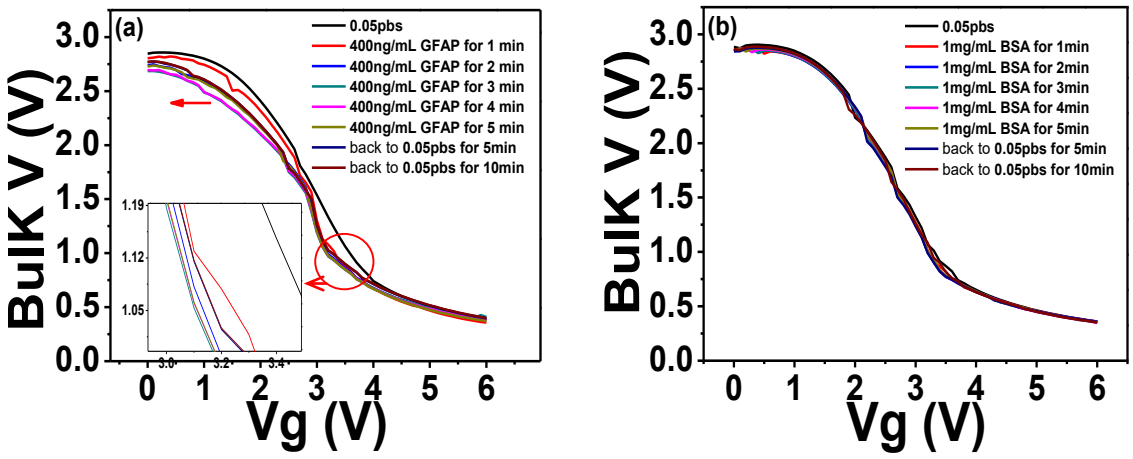

Figure 53 The sensing behavior of the anti-GFAP modified inverter (using pentacene and 8-3 NTCDI) on exposure to a) 400ng/ml (8nM) GFAP; b) 1mg/mL BSA.

4.4 Conclusions

We have successfully developed a highly sensitive (20 pM) and selective sensor platform for brain injury marker (GFAP) detection using both p- and n-type organic molecules as semiconductors. Control experiments also proved that this sensor

platform exhibits excellent selectivity and target protein recognition ability. P- and n-channel semiconductors gave opposite current responses, as expected. To the best of our knowledge, this is the most sensitive protein sensor based on OTFTs. We also report the first use of an n-channel organic film as a specific protein sensor semiconductor, opening up the possibility of sensitive complementary organic inverter biosensors.

The ability to define the p- and n-channels and the ease of processing are the main advantages of our use of organic semiconductors at this stage. While they presently provide a convenient demonstration vehicle, the semiconducting and transduction activities could ultimately be obtained with inorganic alternatives as well, while continuing to take advantage of the top dielectric and coupling chemistries. This platform should be generalizable to other clinically relevant biomarker complexation and detection needs.

Acknowledgements

We would like to thank Weiguo Huang for the fruitful discussions, guidance and for the new modified Procedure to activate NHS on the device surface. We are grateful to the Cove Point Foundation for primary support of this work. We also thank the JHU Environment, Energy, Sustainability and Health Institute for support of water-stable OFET development.

References

1. Savage, W. J. *et al.* Plasma glial fibrillary acidic protein levels in children with sickle cell disease. *Am. J. Hematol.* **86,** 427–429 (2011).
2. Savage, W. J., Everett, A. D. & Casella, J. F. Plasma Glial Fibrillary Acidic Protein Levels in a Child with Sickle Cell Disease and Stroke. *Acta Haematol* **125,** 103–106 (2010).
3. Bell, J. E., Becher, J. C., Wyatt, B., Keeling, J. W. & McIntosh, N. Brain damage and axonal injury in a Scottish cohort of neonatal deaths. *Brain* **128,** 1070–1081 (2005).
4. Blennow, M., Sävman, K., Ilves, P., Thoresen, M. & Rosengren, L. Brain-specific proteins in the cerebrospinal fluid of severely asphyxiated newborn infants. *Acta Paediatr.* **90,** 1171–1175 (2001).
5. Bernert, G., Hoeger, H., Mosgoeller, W., Stolzlechner, D. & Lubec, B. Neurodegeneration, neuronal loss, and neurotransmitter changes in the adult guinea pig with perinatal asphyxia. *Pediatr. Res.* **54,** 523–528 (2003).
6. Bembea, M. M. *et al.* Glial fibrillary acidic protein as a brain injury biomarker in children undergoing extracorporeal membrane oxygenation. *Pediatr. Crit. Care Med.* **12,** 572–579 (2011).
7. Pelinka, L. E. *et al.* Glial fibrillary acidic protein in serum after traumatic brain injury and multiple trauma. *J Trauma* **57,** 1006–1012 (2004).
8. Honda, M. *et al.* Serum glial fibrillary acidic protein is a highly specific biomarker for traumatic brain injury in humans compared with S-100B and

neuron-specific enolase. *J. Trauma* **69,** 104–109 (2010).

9. Wiesmann, M. *et al.* Outcome prediction in traumatic brain injury: Comparison of neurological status, CT findings, and blood levels of S100B and GFAP. *Acta Neurol. Scand.* **121,** 178–185 (2010).

10. Dvorak, F., Haberer, I., Sitzer, M. & Foerch, C. Characterisation of the diagnostic window of serum glial fibrillary acidic protein for the differentiation of intracerebral haemorrhage and ischaemic stroke. *Cerebrovasc. Dis.* **27,** 37–41 (2009).

11. Foerch, C. *et al.* Serum glial fibrillary acidic protein as a biomarker for intracerebral haemorrhage in patients with acute stroke. *J. Neurol. Neurosurg. Psychiatry* **77,** 181–184 (2006).

12. Andropoulos, D. B. *et al.* Brain immaturity is associated with brain injury before and after neonatal cardiac surgery with high-flow bypass and cerebral oxygenation monitoring. *J. Thorac. Cardiovasc. Surg.* **139,** 543–556 (2010).

13. Gress, D. R. The problem with asymptomatic cerebral embolic complications in vascular procedures: What if they are not asymptomatic? *J. Am. Coll. Cardiol.* **60,** 1614–1616 (2012).

14. Petzold, A., Keir, G., Green, A. J. E., Giovannoni, G. & Thompson, E. J. An ELISA for glial fibrillary acidic protein. *J. Immunol. Methods* **287,** 169–177 (2004).

15. Wu, G. *et al.* Bioassay of prostate-specific antigen (PSA) using microcantilevers. *Nat. Biotechnol.* **19,** 856–860 (2001).

16. Torsi, L., Dodabalapur, A., Sabbatini, L. & Zambonin, P. . Multi-parameter gas sensors based on organic thin-film-transistors. *Sensors Actuators B Chem.* **67,**

312–316 (2000).

17. Crone, B. *et al.* Electronic sensing of vapors with organic transistors. *Appl. Phys. Lett.* **78,** 2229–2231 (2001).

18. Potje-Kamloth, K. Semiconductor junction gas sensors. *Chem. Rev.* **108,** 367–399 (2008).

19. Someya, T., Dodabalapur, A., Huang, J., See, K. C. & Katz, H. E. Chemical and physical sensing by organic field-effect transistors and related devices. *Adv. Mater.* **22,** 3799–3811 (2010).

20. Huang, J., Miragliotta, J., Becknell, A. & Katz, H. E. Hydroxy-terminated organic semiconductor-based field-effect transistors for phosphonate vapor detection. *J. Am. Chem. Soc.* **129,** 9366–9376 (2007).

21. Hammock, M. L., Sokolov, A. N., Stoltenberg, R. M., Naab, B. D. & Bao, Z. Organic transistors with ordered nanoparticle arrays as a tailorable platform for selective, in situ detection. *ACS Nano* **6,** 3100–3108 (2012).

22. Torsi, L. *et al.* A sensitivity-enhanced field-effect chiral sensor. *Nat. Mater.* **7,** 412–417 (2008).

23. Royer, J. E., Zhang, C., Kummel, A. C. & Trogler, W. C. Air-stable spin-coated naphthalocyanine transistors for enhanced chemical vapor detection. *Langmuir* **28,** 6192–6200 (2012).

24. Bohrer, F. I. *et al.* Gas Sensing Mechanism in Chemiresistive Cobalt and Metal-Free Phthalocyanine Thin Films Gas Sensing Mechanism in Chemiresistive Cobalt and Metal-Free Phthalocyanine Thin Films. 5640–5646 (2007). doi:10.1021/ja0689379

25. Sekitani, T. & Someya, T. Stretchable, large-area organic electronics. *Adv. Mater.* **22,** 2228–2246 (2010).

26. Someya, T., Small, J., Kim, P., Nuckolls, C. & Yardley, J. T. Alcohol vapor sensors based on single-walled carbon nanotube field effect transistors. *Nano Lett.* **3,** 877–881 (2003).

27. Someya, T., Dodabalapur, A., Gelperin, A., Katz, H. E. & Bao, Z. Integration and response of organic electronics with aqueous microfluidics. *Langmuir* **18,** 5299–5302 (2002).

28. Bouvet, M., Xiong, H. & Parra, V. Molecular semiconductor-doped insulator (MSDI) heterojunctions: Oligothiophene/bisphtalocyanine (LuPc2) and perylene/bisphthalocyanine as new structures for gas sensing. *Sensors Actuators, B Chem.* **145,** 501–506 (2010).

29. Esser, B., Schnorr, J. M. & Swager, T. M. Selective detection of ethylene gas using carbon nanotube-based devices: Utility in determination of fruit ripeness. *Angew. Chemie - Int. Ed.* **51,** 5752–5756 (2012).

30. Das, A. *et al.* A nitrogen dioxide sensor based on an organic transistor constructed from amorphous semiconducting polymers. *Adv. Mater.* **19,** 4018–4023 (2007).

31. Khan, H. U., Jang, J., Kim, J. J. & Knoll, W. In situ antibody detection and charge discrimination using aqueous stable pentacene transistor biosensors. *J. Am. Chem. Soc.* **133,** 2170–2176 (2011).

32. Magliulo, M. *et al.* Electrolyte-gated organic field-effect transistor sensors based on supported biotinylated phospholipid bilayer. *Adv. Mater.* **25,** 2090–

2094 (2013).

33. Gonçalves, D., Prazeres, D. M. F., Chu, V. & Conde, J. P. Detection of DNA and proteins using amorphous silicon ion-sensitive thin-film field effect transistors. *Biosens. Bioelectron.* **24,** 545–551 (2008).

34. Zheng, G., Patolsky, F., Cui, Y., Wang, W. U. & Lieber, C. M. Multiplexed electrical detection of cancer markers with nanowire sensor arrays. *Nat. Biotechnol.* **23,** 1294–1301 (2005).

35. Estrela, P. *et al.* Label-free sub-picomolar protein detection with field-effect transistors. *Anal. Chem.* **82,** 3531–3536 (2010).

36. Kergoat, L. *et al.* A water-gate organic field-effect transistor. *Adv. Mater.* **22,** 2565–2569 (2010).

37. Buth, F., Donner, A., Sachsenhauser, M., Stutzmann, M. & Garrido, J. A. Biofunctional electrolyte-gated organic field-effect transistors. *Adv. Mater.* **24,** 4511–4517 (2012).

38. Kim, Z. S., Lim, S. C., Kim, S. H., Yang, Y. S. & Hwang, D. H. Biotin-functionalized semiconducting polymer in an organic field effect transistor and application as a biosensor. *Sensors (Switzerland)* **12,** 11238–11248 (2012).

39. Khan, H. U. *et al.* In situ, label-free DNA detection using organic transistor sensors. *Adv. Mater.* **22,** 4452–4456 (2010).

40. Lai, S. *et al.* Ultralow voltage, OTFT-based sensor for label-free DNA detection. *Adv. Mater.* **25,** 103–107 (2013).

41. Duan, X. *et al.* Intracellular recordings of action potentials by an extracellular nanoscale field-effect transistor. *Nat. Nanotechnol.* **7,** 174–179 (2011).

42. McAlpine, M. C., Ahmad, H., Wang, D. & Heath, J. R. Highly ordered nanowire arrays on plastic substrates for ultrasensitive flexible chemical sensors. *Nat. Mater.* **6,** 379–84 (2007).

43. Kergoat, L. *et al.* DNA detection with a water-gated organic field-effect transistor. *Org. Electron.* **13,** 1–6 (2012).

44. Lin, T.-W. *et al.* Label-free detection of protein-protein interactions using a calmodulin-modified nanowire transistor. *Proc. Natl. Acad. Sci. U. S. A.* **107,** 1047–1052 (2010).

45. Gruner, G. Carbon nanotube transistors for biosensing applications. *Anal. Bioanal. Chem.* **384,** 322–35 (2006).

46. Bobbert, P. A., Sharma, A., Mathijssen, S. G. J., Kemerink, M. & De Leeuw, D. M. Operational stability of organic field-effect transistors. *Adv. Mater.* **24,** 1146–1158 (2012).

47. Hakim, M. M. A. *et al.* Thin film polycrystalline silicon nanowire biosensors. *Nano Lett.* **12,** 1868–1872 (2012).

48. Cheng, Y. *et al.* Functionalized SnO_2 nanobelt field-effect transistor sensors for label-free detection of cardiac troponin. *Biosens. Bioelectron.* **26,** 4538–44 (2011).

49. Lerner, M. B. *et al.* Hybrids of a genetically engineered antibody and a carbon nanotube transistor for detection of prostate cancer biomarkers. *ACS Nano* **6,** 5143–5149 (2012).

50. Allen, B. L., Kichambare, P. D. & Star, A. Carbon nanotube field-effect-transistor-based biosensors. *Adv. Mater.* **19,** 1439–1451 (2007).

51. Heller, I. *et al.* Identifying the mechanism of biosensing with carbon nanotube transistors. *Nano Lett.* **8,** 591–595 (2008).

52. Kuang, Z., Kim, S. N., Crookes-Goodson, W. J., Farmer, B. L. & Naik, R. R. Biomimetic chemosensor: Designing peptide recognition elements for surface functionalization of carbon nanotube field effect transistors. *ACS Nano* **4,** 452–458 (2010).

53. Kim, S. N., Rusling, J. F. & Papadimitrakopoulos, F. Carbon nanotubes for electronic and electrochemical detection of biomolecules. *Adv. Mater.* **19,** 3214–3228 (2007).

54. Seon Joo Park, Oh Seok Kwon, Sang Hun Lee, Hyun Seok Song, Tai Hyun Park, and J. J. Ultrasensitive Flexible Graphene Based Field-E ff ect Transistor (FET)-Type Bioelectronic Nose. **12,** 5082–5090 (2012).

55. Gao, Y. & Kyratzis, I. Covalent immobilization of proteins on carbon nanotubes using the cross-linker 1-ethyl-3-(3-dimethylaminopropyl)carbodiimide--a critical assessment. *Bioconjug. Chem.* **19,** 1945–1950 (2008).

56. Ohno, Y., Maehashi, K., Yamashiro, Y. & Matsumoto, K. Electrolyte-gated graphene field-effect transistors for detecting ph and protein adsorption. *Nano Lett.* **9,** 3318–3322 (2009).

57. Katz, H. E. *et al.* A soluble and air-stable organic semiconductor with high electron mobility. *Nature* **404,** 478–481 (2000).

58. Katz, H. E., Johnson, J., Lovinger, A. J. & Li, W. Naphthalenetetracarboxylic diimide-based n-channel transistor semiconductors: Structural variation and thiol-enhanced gold contacts. *J. Am. Chem. Soc.* **122,** 7787–7792 (2000).

59. Fong, H. H. *et al.* Orthogonal processing and patterning enabled by highly fluorinated light-emitting polymers. *Adv. Mater.* **23,** 735–739 (2011).

60. Fujisaki, Y. *et al.* Air-stable n-type organic thin-film transistor array and high gain complementary inverter on flexible substrate. *Appl. Phys. Lett.* **97,** 133303 (2010).

61. Barra, M. *et al.* Transport property and charge trap comparison for N-channel perylene diimide transistors with different air-stability. *J. Phys. Chem. C* **114,** 20387–20393 (2010).

62. Ng, T. N. *et al.* Electrical stability of inkjet-patterned organic complementary inverters measured in ambient conditions. *Appl. Phys. Lett.* **94,** 233307 (2009).

63. Lahiri, J., Isaacs, L., Tien, J. & Whitesides, G. M. A strategy for the generation of surfaces presenting ligands for studies of binding based on an active ester as a common reactive intermediate: A surface plasmon resonance study. *Anal. Chem.* **71,** 777–790 (1999).

64. Stern, E. *et al.* Importance of the debye screening length on nanowire field effect transistor sensors. *Nano Lett.* **7,** 3405–3409 (2007).

65. Sorgenfrei, S., Chiu, C. Y., Johnston, M., Nuckolls, C. & Shepard, K. L. Debye screening in single-molecule carbon nanotube field-effect sensors. *Nano Lett.* **11,** 3739–3743 (2011).

66. Kulkarni, G. S. & Zhong, Z. Detection beyond the Debye screening length in a high-frequency nanoelectronic biosensor. *Nano Lett.* **12,** 719–723 (2012).

67. Bohrer, F. I. *et al.* Selective detection of vapor phase hydrogen peroxide with

phthalocyanine chemiresistors. *J. Am. Chem. Soc.* **130,** 3712–3713 (2008).

68. Park, Y. M. & Salleo, A. Dual-gate organic thin film transistors as chemical sensors. *Appl. Phys. Lett.* **95,** 1–4 (2009).

69. Hammock, M. L., Knopfmacher, O., Naab, B. D., Tok, J. B. H. & Bao, Z. Investigation of protein detection parameters using nanofunctionalized organic field-effect transistors. *ACS Nano* **7,** 3970–3980 (2013).

70. Khalil, O. S. Spectroscopic and clinical aspects of noninvasive glucose measurements. *Clin. Chem.* **45,** 165–177 (1999).

71. Tremblay, N. J., Jung, B. J., Breysse, P. & Katz, H. E. Digital Inverter Amine Sensing via Synergistic Responses by n and p Organic Semiconductors. *Adv. Funct. Mater.* **21,** 4314–4319 (2011).

Part 2

Chapter 5

Demonstration of Hole Transport and Voltage Equilibration in Self-Assembled Pi-Conjugated Peptide Nanostructures Using Field-Effect Transistor Architectures

5.1 Introduction

Pi-conjugated peptide materials are attractive for bioelectronics due to their unique photophysical characteristics, biofunctional interfaces, and processability under aqueous conditions. In order to be relevant for electrical applications, these types of materials must be able to support the passage of current and the transmission of applied voltages.

While biopolymers such as DNA[1], RNA[2] and or other biological scaffolds such as carbohydrates[3] and steroids[4] have been widely used as self-assembling systems for the construction of semiconducting and optoelectronic nanostructures, the vast majority of bio-inspired organic electronic research has utilized peptide-based architectures derived from natural amino acids[5–14], building blocks that are considered attractive for new materials design because of the scalability, ease of standard solid-phase peptide synthesis and the wide variety of side chains that can be used to alter molecular and supramolecular properties[15]. Oligopeptides have been attached to π-conjugated components in order to form one-dimensional (1D) nanostructures with photophysical and electronic properties that show promise for

functional materials, including materials for electronic stimulation of cells. Among the advantages of these types of platforms for organizing π-conjugated oligomers are allowance for a controlled assembly of heterogeneous mixtures of donor and acceptor containing materials[16–18] and addition of reactive groups for further functionality[19]. The general organic semiconductor field is rich with examples of solubilizing (and electrically insulating) alkyl side chains that also promote crystalline self-assembly in the solid-state thereby improving charge transport. Interestingly, attaching semiconducting units to self-assembling amide substituents that result in organogel formation has led to measurable charge mobilities upon incorporation in organic field-effect transistors (OFETs)[20,21]. However, utilizing longer oligopeptide assembling subunits limits the charge transport properties because of the large volume fraction of "insulating" peptide moieties, thus making it challenging to build electronic devices and directly characterize conductivity of more biologically relevant constructs[14,22].

In this work, we utilize tripeptide-π-tripeptide constructs as switchable semiconducting layers or alternatively as the gate electrodes of bottom-gate OFETs. This type of π-conjugated peptide presents the bioactive peptide segments at the termini with a semiconducting π-system unit embedded in the core. We chose quaterthiophene (4T), a hole-transporting organic semiconductor, as the central π-system[23]. For the tripeptide segment, we placed a negatively charged amino acid (aspartic acid, D, or glutamic acid, E) at the distal termini and aliphatic dipeptides (glycine, G; alanine, A; valine, V; isoleucine, I) near the π-core. This design allows for pH-triggered interconnected nanostructure assembly under acidic aqueous

conditions while basic conditions generally result in essentially molecular solutions. In earlier studies, these peptide-π-peptide constructs were incorporated as active layers of OFETs, with hole mobility values of 1.4×10^{-3} to 0.03 $cm^2\ V^{-1}\ s^{-1}$ for a 4T core with different macroscopic orientations[24]. The previous study with Glu-Ala-Ala peptides conjugated to a 4T core is the first report of gate field conductance modulation for nanostructured π-conjugated units embedded within insulating peptide moieties assembled under aqueous conditions. Here, we report the incorporation of various sequences of 4T-bound tripeptide nanomaterials as both the active semiconducting layers and for the first time, as gates in a bottom-gate top-contact OFET configuration. We investigate different peptide sequences attached to a 4T semiconductor and determine whether sequence variation is a feasible way to modulate field-effect electronic properties since this strategy has been previously shown to rationally modulate excited-state photophysics[25] and the sheet resistance of π-conjugated peptide films[26]. This study focuses on the electronic device properties of this hydrogel-forming material, building on the fundamental understanding of carrier transport and voltage equilibration of π-conjugated peptides for future biological applications.

5.2 Experimental Section

5.2.1 Peptide Synthesis

All π-conjugated peptides were synthesized using solid-phase peptide synthesis followed by Pd-catalyzed cross coupling, according to our previous reports[27,28]. Details can be found in the Supporting Information.

5.2.2 Transmission Electron Microscopy (TEM)

Nanostructures were prepared by acidifying 1 mg/mL (*ca.* 1 mM) solutions of peptides in Milli-Q water. Samples were adsorbed for 5 minutes (at 25°C) onto 300 mesh copper grids coated with Formvar in carbon film (Electron Microscopy Sciences). All samples were stained with a 2% uranyl acetate solution. The grids were allowed to dry prior to imaging. Images were acquired using a Philips EM 420 transmission electron microscope equipped with SIS Megaview III CCD digital camera, at an accelerating voltage of 100 kV. ImageJ 1.47 (National Institutes of Health, Bethesda, MD, USA) was used to approximate the widths of the nanostructures (at least n=25 per TEM image).

5.2.3 Atomic Force Microscopy (AFM)

Acidified peptide solutions (0.1 mg/ml, 0.1 mM) were dropcasted into SiO_2 substrates**.** Topography images were taken in tapping mode using a Dimensional 3100 AFM (Bruker Nano, Santa Barbara, CA). The images were visualized using the Nanoscope software (Bruker).

5.2.4 3D Laser Scanning Microscopy

In order to characterize the surface roughness and height profile of the dried, acid-assembled peptide films on glass, all samples were observed under a Keyence Color 3R Laser Microscope VK-X100K/X200K.

5.2.5 Device Fabrication and Measurements

The OFET devices with π-conjugated peptide nanostructure films used as the

semiconductor active layers were fabricated on silicon wafers (with 300 nm silicon dioxide; capacitance per area=11.5 nF/cm^2). The wafers were cut into 1-inch by 1-inch square samples, which were cleaned by keeping them in piranha solution (3:1 ratio of concentrated sulfuric acid to hydrogen peroxide) for 3-4 hours followed by sonication in acetone and isopropanol for 30 minutes. The samples were blown dry using dry nitrogen flow. To each Si/SiO_2 substrate, 5 μL of 1 wt% (*ca.* 10 mM) peptide solution was dropcast and then exposed to an acid chamber (closed chamber with concentrated HCl vapor) for 5 minutes prior to drying at ambient temperature and pressure. The gold source and drain electrodes (50 nm-thick) were deposited using a TEM grid as the shadow mask (W/L=10) by physical vapor deposition while keeping the chamber temperature below 60°C.

For the OFET devices with the π-conjugated peptide nanostructures used as the gate, microscopic glass slides were cut into 1-inch by 1-inch squares and then subsequently cleaned by sonication in acetone followed by sonication in isopropanol. The glass substrate was blown dry by using dry nitrogen flow. Then, 2-cm by 3-mm rectangle Novec wells were painted on the glass substrates. The 1 wt% peptide solutions were dropcast on these wells and acidified as described earlier. The dielectric layer was then vapor-deposited on top of the assembled peptide films. Two different compounds were used to function as dielectric material: tetratetracontane ($C_{44}H_{90}$, C_{44}), and pentaerythritol. They were chosen to observe the effects of varying polarites of groups present (with tetratetracontane being a wax and pentaerythritol having a large number of hydroxyl groups, approaching a solid form of "water"). The thickness of the dielectric was varied from 20 nm to 100

nm. For these devices with assembled peptides as the gates, 25 nm of pentacene was vapor-deposited as the active semiconductor layer as it has been widely studied and is a very reliable organic semiconductor. As the nanomaterial drop-cast films are hardly only ½ cm wide, TEM grid mask was used to deposit 50 nm-thick gold electrodes. All the OFET measurements were done using an Agilent 4155C semiconductor analyzer under ambient conditions.

5.3 Results and Discussion

The peptide-π-peptide triblock units (Figure 54) investigated in this study were all observed to have pH-triggered assembly behavior, wherein the protonation of carboxylates under acidic conditions mitigates Columbic repulsion thus allowing for more intermolecular hydrogen bonding among the peptide backbones and π-electron interactions among the embedded 4T units. The 4T system was selected as the π-electron core in this study because it is a well-established *p*-channel semiconductor subunit. The spectroscopic investigations from our previous report[26] for D*XX*-4T peptides along with our findings for E*XX*-4T peptides here show that these 4T bis(peptides) have maximum absorption at 418 nm under basic conditions (*ca.* pH 10) which blue-shifts under acidic conditions (*ca.* pH 2) ranging from ~360 nm to 410 nm as the amino acid bulk adjacent to the chromophore increases (Table S1, Figure S5 (a)). The emission profiles of these π-conjugated peptides under basic conditions have a maximum at 510 nm, which red shift to ~540 nm under acidic conditions (Figure S5 (b)). The circular dichroism (CD) spectra also shows varied bisignate exciton-coupled π-π* signals (*i.e.,* different intensities and signs of the

Cotton bands) among the peptides that have crossovers near the absorption maximum of each peptide, suggesting the differences in the extent of interactions between the 4T units held in local chiral environments (Figure S5 (c)). Varying the amino acid termini from glutamic acid residues to aspartic acid residues does not dramatically change the observed spectral profiles. These spectroscopic features support that these peptides form "H-like" aggregates upon assembly under acidic conditions.

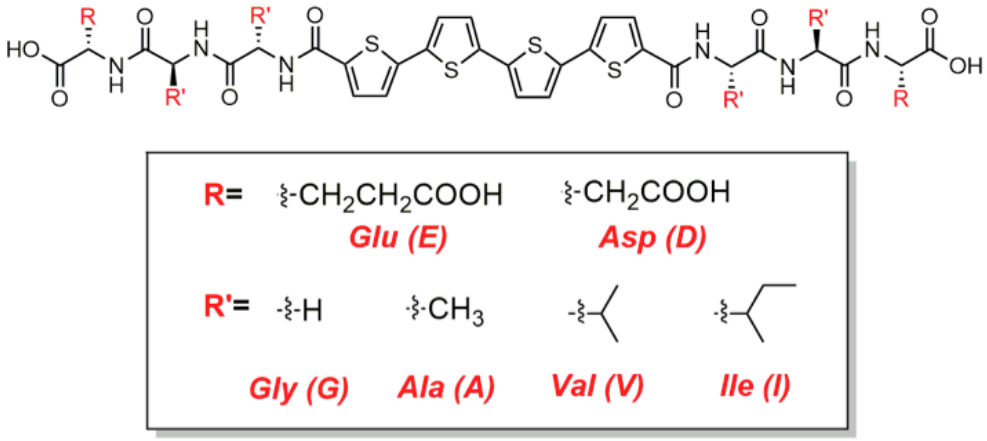

Figure 54 Molecular structure of the 4T bis(peptides) used for OFET devices .

5.3.1 Nanostructure and Film Morphology

The formation of 1D-nanostructures from 0.01 to 1 wt% peptide solutions under acidic conditions were consistently observed for all the eight 4T peptides studied in solution and in dropcast films, with the alanine-containing peptides having the largest nanostructure widths (Figure 55 (a-c)). The nanostructure lengths span up to micrometers, while the widths for 0.1 wt% acidified solutions of D*XX* peptides were previously reported to range from 3 nm to 12 nm (*i.e.,* DAA nanostructures have ~12 nm width, while DGG, DVV and DII are around 3-4 nm)[26]. All peptide

sequences show well connected nanostructures in the gel form, as shown in the TEM images (Figure S6-Figure S13). It is interesting to note that the VV- and II-containing peptide hydrogels seem to have regions with local alignment, which could be attributed to high beta-sheet propensities within the peptide backbones based upon these sequences (Figure S8-Figure S10, Figure S12-Figure S14). Even though nanostructure bundling is evident for these cases, the hydrogel fiber network seems to be less dense than for GG- and AA-containing peptides in the gel state. We investigated the dropcast film topography using AFM and measured the film roughness/thickness using a laser profilometer (Figure 55(a,b,d); Figure S14-Figure S16). The AFM images for EAA- and EVV-4T peptides show that the 1D-nanostructures are still microns in length in the dropcast films that were used for device fabrication. These are consistent with the solution-state morphological characterizations and nanostructural models reported previously for these tripeptide-quaterthiophenes[26]. The microscopic surface profiles show varied surface roughness among the peptides that can be attributed to the different nanostructure aggregation behaviors upon drying of dropcast films of the peptides with different hydrophobicities. These surface profiles for the dropcast films (< 10 μm-thick) support the network characteristics observed in hydrogel TEM, wherein GG- and AA-containing peptides show islands of dense networks of assembled nanostructures while VV- and II-containing peptides show more uniform films. Both AFM and surface profile characterizations were conducted on silicon surfaces and therefore can be reasonably extrapolated to the surfaces upon which these nanomaterials would be deposited for device fabrication. As thoroughly

investigated in our previous studies[25,26], which are also supported by the recorded absorption and emission profiles for the eight 4T-peptides studied herein, such systematic variations of the amino acid bulk adjacent to the π-electron core result in varied photophysical properties due to the differences in the local packing order and contact of π-electron units within each assembled nanostructure. The effects of sequence variation were also previously observed for macroscopic material properties such as mechanical properties, due to the differences in the "bundling" interactions between the 1D-nanostructures[26]. Due to the observed variations in the surface roughness and local aggregation patterns of the films of the sequence-varied peptides, we expect that this would have implications for the macroscopic connectivity of the semiconducting units, and thus for the currents passing through the films in device structures, as discussed below.

The organic field effect transistor is the foundational structure for technical applications like RFID (radio frequency detection), roll-up light emitting displays and different sensor platforms that possess attractive attributes such as printability, low cost production, and mechanical flexibility[29–31]. Film morphologies are closely related to device output currents[32–36]. Specific morphological factors include grain size, connectivity, orientation or packing disorder and traps (chemical or interfacial) in the films[37]. For the present self-assembling peptides, the nanostructure assembly and the macroscopic film morphology are both crucial features for determining electronic signal transmission. All the eight peptides studied herein form 1D-nanostructures that are microns in length, 3-12 nm in width, varied network connectivities in gel and solution state, and varied surface roughness in the

microscale (for dropcast films). Here, we are using the OFET architecture as an analytical tool to indicate effects of different nanostructure assembly morphologies on charge carrier mobility and electrical conductivity.

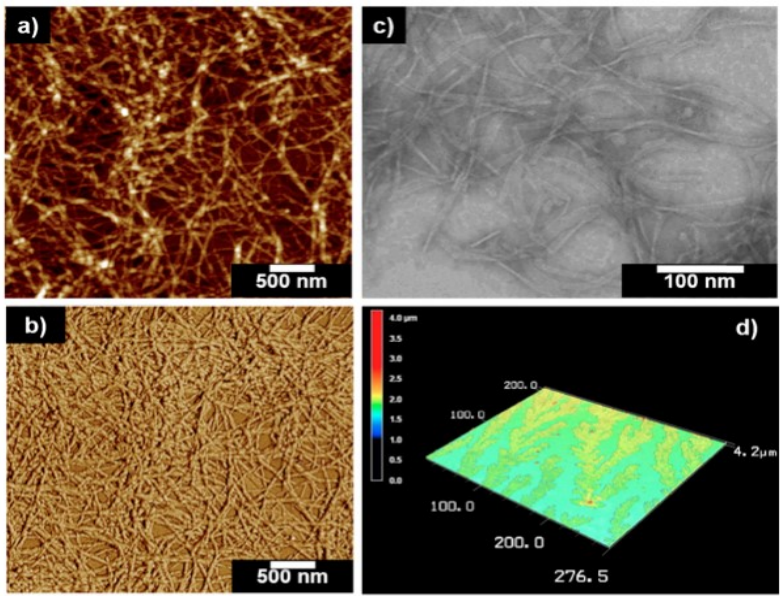

Figure 55 AFM image of 0.1 mg/mL dropcast film of assembled EAA-4T peptide, a) height b) phase profile; TEM image of 1mg/mL EAA-4T solution; d) surface profile of a 10mg/mL dropcast film EAA-4T under a laser microscope.

5.3.2 OFETs with π-Conjugated Peptides as the Semiconducting Layer

In order to characterize the semiconducting behavior of the 4T cores bound within peptide environments with different hydrophobicities, we deposited thin films of peptide nanomaterials as semiconducting layers in bottom-gate OFET configurations (Figure 56a). There have been a few isolated reports on the carrier mobilities of biomolecule-containing oligothiophene nanomaterials with π-electron function, revealing mobilities on the order of 10^{-8}-10^{-4} cm^2 V^{-1} s^{-1} [38–40]. One goal of the present work is to reveal how molecular variation impacts nanostructure-

dependent transport properties. We used controls without the semiconducting unit (Figure 56b-c)[41]. These two peptide nanomaterials were chosen as the control samples because they form similar one-dimensional nanostructures[41] (Figure S17) under aqueous conditions that would be geometrically relevant for the pi-conjugated peptides studied herein. Control sample **1** is a direct analog of peptide-4T-peptide, with the 4T substituted by $-(CH_2)_{10}$ units, while control sample **2** has an amphiphilic design with more charged residues in the peptide backbone than **1.** When the controls were used as the semiconducting layer, no apparent gating effects were observed. This supports the premise that the 4T-containing nanostructures in the film are providing charge transport pathways that do not merely rely on ionic effects and in fact require the presence of hole-transporting 4T subunits.

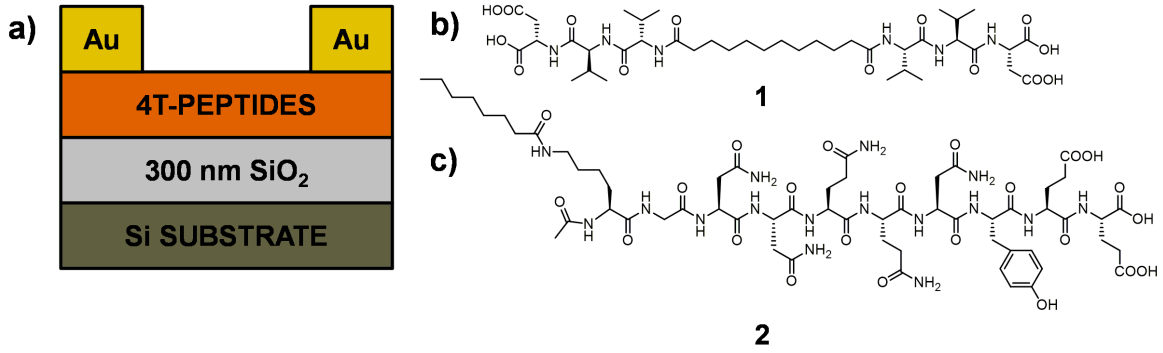

Figure 56 a) Schematic of the FET architecture used to measure the hole mobilities within the peptide nanostructure; b), c) control compound used as the active layer replacing 4T-peptides in the configuration shown in a).

All the peptide-4T nanowires gave semiconductor characteristics but the mobility values (Table 5) were observed to vary by three orders of magnitude upon varying

the amino acids adjacent to the 4T semiconductor. The corresponding output curves (Figure 57) show the gate-modulated field conductance for all the peptides. Although we cannot directly compare the mobility values between devices constructed using different protocols, it is worth noting that the better performing –G and –A based peptides are within the order of magnitude or higher than the mobility values reported for unsubstituted quaterthiophenes unbound to peptide moieties ($\sim 10^{-3}$ cm^2 V^{-1} s^{-1})[42,43]. Considering that the quaterthiophenes used in this study are bound to peptides *via* carboxamide electron-withdrawing groups, the comparable performance of these peptide-quaterthiophene conjugates to unmodified quaterthiophenes is remarkable. The peptides with the smallest –GG and –AA residues adjacent to 4T gave the highest mobility values. Those peptide nanostructures with the bulky –VV sequences, which have photophysical properties for the assembly that are least shifted from the dissolved π-conjugated peptide under basic conditions[26], showed the lowest mobility values. Apparently, even bulkier hydrophobic isoleucine residues perturb the assembly such that the charge-transporting properties within the assembly (as represented by hole mobilities) are inferior to the other peptides studied herein. This trend for the hole transport properties of these peptide nanostructures is a manifestation of the photophysical properties observed in solution state , wherein the –GG and –AA peptides that have the strongest intermolecular electronic couplings with the most blue-shifted absorption spectra and most quenched emission yielded higher mobility values. Such trend can also be correlated to the importance of local packing order (nanostructure helicity, packing homogeneity, propensity to form ordered

structures) and intermolecular distances of the semiconducting oligomers within the self-assembled nanostructures on the charge transport behavior of the resulting films; both of which affect intermolecular π-electron delocalization[25,26].

Peptide -4T	**μ_h / cm^2 V^{-1} s^{-1}**
DGG	0.017 ± 0.006
DAA	0.004 ± 0.003
DVV	$6.9 \times 10^{-5} \pm 2.1 \times 10^{-5}$
EGG	0.002 ± 0.0006
EAA	0.005 ± 0.004
EVV	$4.7 \times 10^{-5} \pm 6.2 \times 10^{-5}$

Table 5 Mobility values for different 4T-containing containig peptides.

The DAA and EAA peptides show ~three times greater nanostructure width than the six other peptides.[30] While this suggests a general correlation of nanostructure width and mobility, DGG is an exception, where the intermolecular interactions leading to the blue-shifted spectra are apparently dominant. The DVV and EVV samples, on the other hand, were observed to have more dispersed nanostructures within their dropcast films or in their gel state (Figure S8 andFigure S12). Considering the mobility data in Table 5 and the nanostructure characteristics that comprise the dropcast films, it could be deduced that nanostructure connectivity *(i.e.,* network formation) and the individual nanostructure morphology are the major factors to be considered for performance of these devices. Another factor that might be affecting the huge variations of mobility values between the devices of same peptide is the local alignment of nanowires within the device. It was previously reported that having the electrodes parallel to the alignment of the

nanostructures led to better charge transport as compared to when the electrodes are perpendicular to the direction of material alignment[24]. Ideally, the films reported here should have randomly aligned nanowires distributed within the layer. However, it is possible that there are areas with local alignment where the probes are directed, and hence leading to higher mobility values as compared to other area. Moreover, the different chemical and interfacial traps could also be unevenly distributed within the semiconducting film that is mainly comprised of non-conducting peptide moieties, leading to variations for the calculated mobility values per device. When these devices are tested over a period of time, a continuous increase in drain current was observed with or without light irradiation, which indicates that there are low-lying traps being filled. We did not observe any photoconductive response in this geometry, although there are reports about photoconductive effects for other semiconductor-containing peptide gels[26,44]. The two effects (field effect and photoconductivity) likely target the same energy level, so they are very closely intertwined and, in this particular device structure, we are not able to decouple these effects. It was also observed that there is a significant off-current—free ionic current in the material that is not related to gate leakage.

5.3.3 OFETs with π-Conjugated Peptides as the Gate Layer

Because the –AA sequences yielded the nanostructures with the largest widths and seemed to result in films with good connectivities between nanostructures, we chose these nanostructures to also function as gates for OFET devices (Figure 58) in order to assess the capability for these nanomaterials to support voltage

transmission from an electrode contact and thus serve as an electrical extension of this contact.

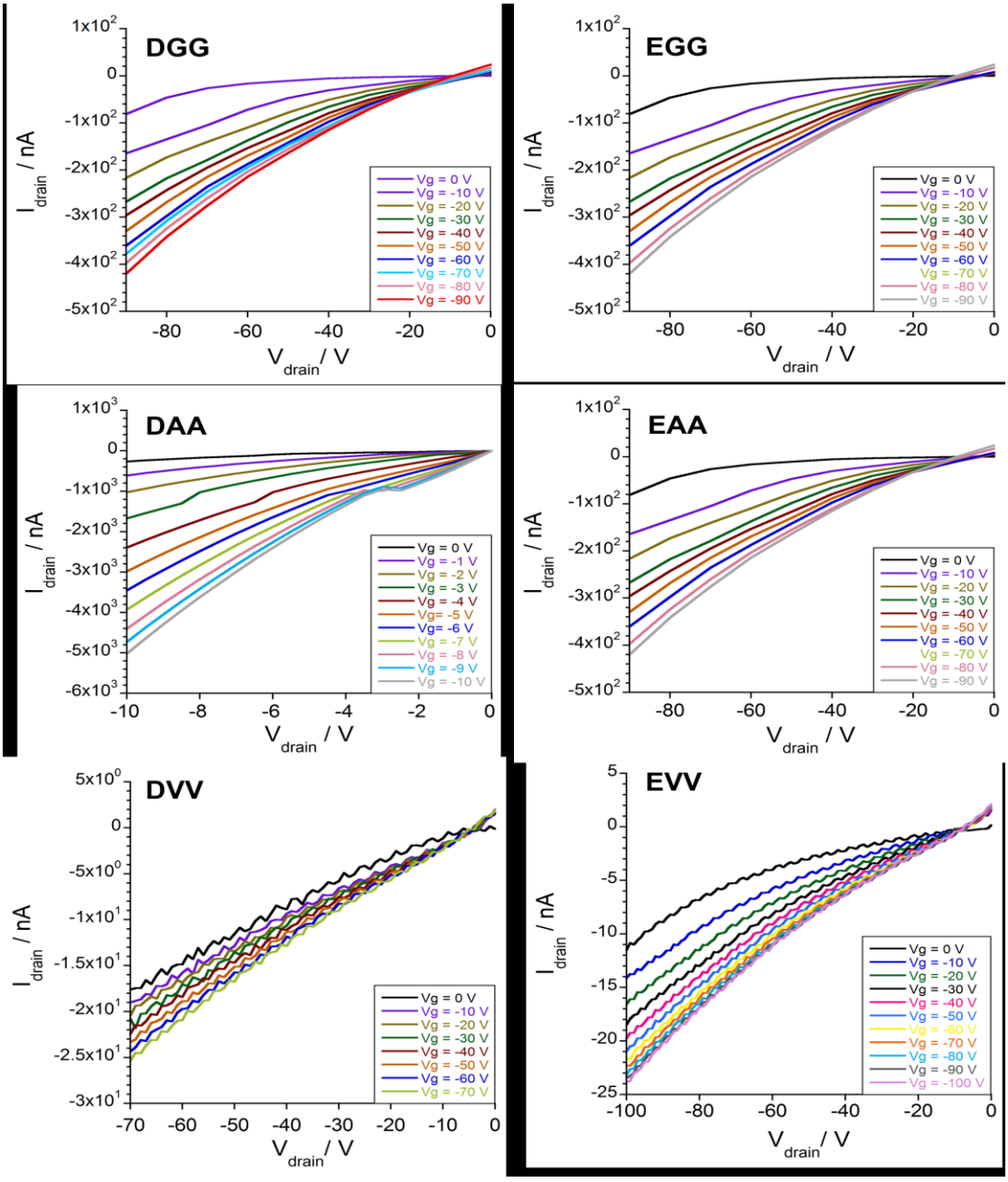

Figure 57 Output curves for OFET devices with the 4T bis(peptides) as the semiconductor active layers.

In this configuration, pentacene was used as the semiconductor while $C_{44}H_{90}$ (tetratetracontane) and pentaerythritol were chosen as the materials for gate dielectric layers because they form continuous films and bracket the extremes of hydrophobicity and hydrophilicity.

The hydrocarbon has a dielectric constant of about 2.5[45]. Pentaerythritol will have a dielectric constant on the order of 10, depending on the degree of hydration, by analogy to dextran, a solid with similar density of polar oxy- functional groups[46]. With its high density of OH groups, pentaerythritol begins to model the OH-rich environment around cells (Figure S18). To determine whether the conjugated core and the nanowire self-assembly were necessary for gate voltage equilibration, we also fabricated devices with control samples **1** and **2** (Figure 56b-c) as the gate material. Control sample **2** gave very similar results to the DAA sample, although the drain current in the pentacene channel was slightly lower **2** than for DAA, while **1** does not give any working OFET data. This indicates that the free ions present in the materials are partially responsible for the voltage transmission properties regardless of the composition of the internal cores (the hydrogels formed from peptides with and without π-electron cores are acidic). Moreover, the thickness of the dielectric layer was varied between 20 nm and 100 nm in order to establish the maximum thickness through which the nanowire materials can transmit modest voltage that could be needed to stimulate a bilipical structure (*e.g.,* cell membranes, < 10 nm). We would expect that by increasing the dielectric thickness over which the voltage has to be transmitted, the gating effect would be weaker as interfacial dipole could compensate the voltage applied through the dielectric. We noticed that

35-40 nm dielectric allows the maximum electric field to drop across the dielectric layer without undue leakage current (Figure 59).

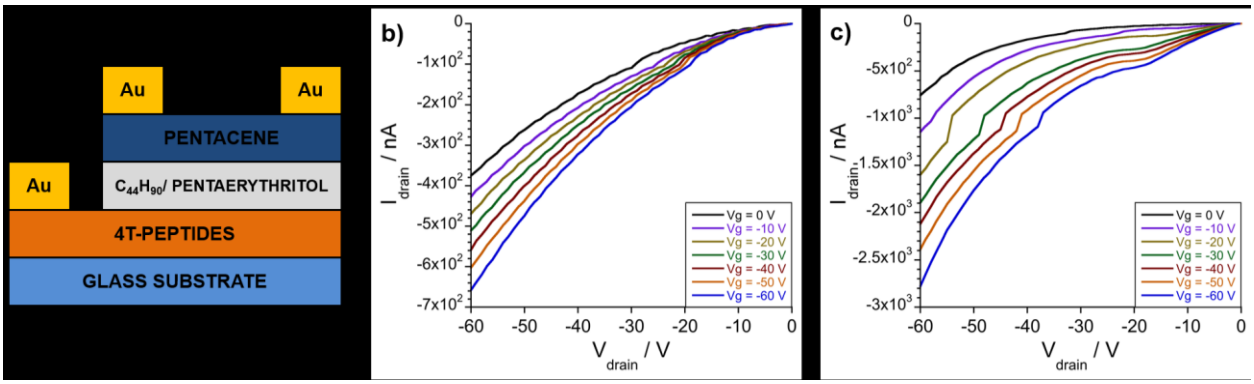

Figure 58 a) Schematic diagram of the FET devices with peptide nanostructures as the gate; output curves for b) control peptide 2 and c) DAA-4T used as a gate layer in the configuration shown in a) with $C_{44}H_{90}$ as the dielectric layer.

Consistent with previous observation we found that 20 nm was too low thickness for forming well connected films because of island growth morphology of tetratetracontane[45]. Related π-conjugated peptides have been previously found to have both protons and electrons as contributors to the conduction, with the dominating carrier being dependent on the humidity because of its effect on peptide folding[47]. Our results imply that the materials studied herein can impart an electrical field over approximately 35-40 nm effectively.

We noticed that DAA does demonstrate the expected trend with the increasing dielectric thickness but the gating behavior is still apparent, while in EAA, the gating behavior almost ceases to exist above 70 nm dielectric thickness. This strengthens our claim that terminal charged groups indeed have a contribution in the overall gating effect. It is interesting to note that upon testing control sample **1**, with less

charged residues and being mainly comprised of hydrophobic valine residues, no gating effect was observed for this geometry.

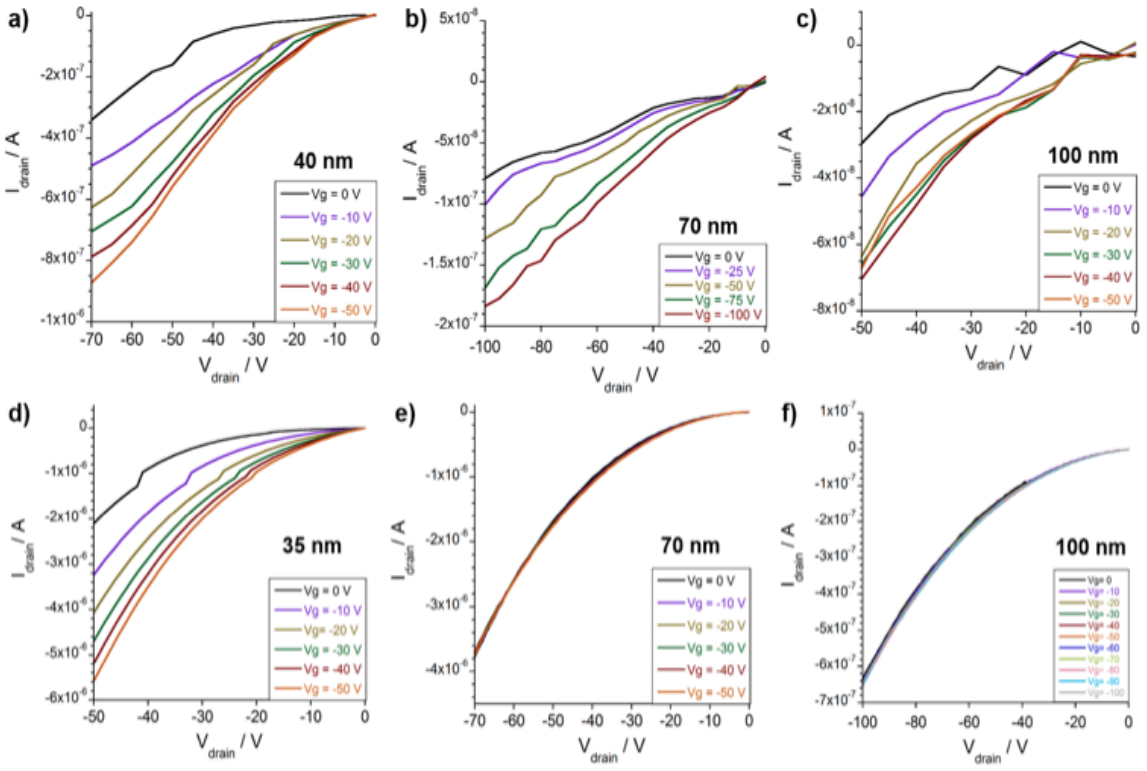

Figure 59 Output curves showing the effect of varying the dielectric thickness of an OFET configuration with (a-c) DAA-4T and (d-f) EAA-4T as the gate, pentacene as the semiconductor, and C44H90 as the dielectric layer.

5.4 Conclusions

In summary, we investigated the properties of 4T bis(tripeptide)-based nanostructure OFETs and found that this type of material can show mobility values as high as ~0.02 $cm^2\ V^{-1}\ s^{-1}$ and can be tuned within a range of three orders of magnitude by simply changing the amino acid sequence and keeping the same semiconducting unit. The materials were also sufficiently ionically conductive to serve as OFET gate electrodes. Our success in incorporating assembled

nanostructures in OFETs with clearly observable field-effect modulation when serving both as OFET semiconductors and gates for pentacene semiconductors is the key finding of this study. The modulation of nanostructures as semiconductors required the presence of the conjugated core, even though it was a small fraction of the total nanostructure mass. This demonstration of hole transport, above and beyond ionic conductivity, is crucial for our ultimate goal of electronically or photonically stimulating these materials to influence cell growth and behavior. Experiments are underway investigating the effect of Nano scale electric field propagation on the cellular behavior within these materials.

Acknowledgements

We would like to thank our collaborator Herdeline Ann Ardona for designing and supplying the nanowire solution. We also need to thank her for the TEM, SEM and the spectroscopic characterizations for the nanowire solution. We thank Johns Hopkins University (JHU), the Department of Energy Office of the Basic Energy Sciences (DE-SC0004857, J.D.T and H.E.K., synthesis and electrical characterization of peptide nanomaterials), and the National Science Foundation (DMR-1407493, J.D.T. and H.E.K., field creation in biomaterials) for the generous support. We thank Prof. Honggang Cui of the Department of Chemical and Biological Engineering (JHU) for supplying the control molecule shown in Figure 56 c[43].

References

1. Seeman, N. C. DNA in a material world. *Nature* **421,** 427–431 (2003).
2. Chworos, A. *et al.* Building programmable jigsaw puzzles with RNA. *Science (80-.).* **306,** 2068–2072 (2004).
3. Schmid, S., Mena-Osteritz, E., Kopyshev, A. & Bauerle, P. Self-assembling carbohydrate-functionalized oligothiophenes. *Org. Lett.* **11,** 5098–5101 (2009).
4. Kawano, S. I., Fujita, N. & Shinkai, S. Quater-, quinque-, and sexithiophene organogelators: Unique thermochromism and heating-free sol-gel phase transition. *Chem. - A Eur. J.* **11,** 4735–4742 (2005).
5. Reches, M. Casting Metal Nanowires Within Discrete Self-Assembled Peptide Nanotubes. *Science (80-.).* **300,** 625–627 (2003).
6. Ashkenasy, N., Horne, W. S. & Ghadiri, M. R. Design of self-assembling peptide nanotubes with delocalized electronic states. *Small* **2,** 99–102 (2006).
7. Ghadiri, M. R., Granja, J. R., Milligan, R. a, McRee, D. E. & Khazanovich, N. Self-assembling organic nanotubes based on a cyclic peptide architecture. *Nature* **366,** 324–327 (1993).
8. Diegelmann, S. R., Gorham, J. M. & Tovar, J. D. One-dimensional optoelectronic nanostructures derived from the aqueous self-assembly of π-conjugated oligopeptides. *J. Am. Chem. Soc.* **130,** 13840–13841 (2008).
9. Shao, H., Nguyen, T., Romano, N. C., Modarelli, D. A. & Parquette, J. R. Self-assembly of 1-D n-type nanostructures based on naphthalene diimide-appended dipeptides. *J. Am. Chem. Soc.* **131,** 16374–16376 (2009).

10. Matmour, R. & Cat, I. De. Oligo (p-phenylenevinylene)– Peptide Conjugates: Synthesis and Self-Assembly in Solution and at the Solid– Liquid Interface. *J. Am. Chem. Soc.* **130,** 14576–14583 (2008).

11. Jahnke, E., Lieberwirth, I., Severin, N., Rabe, J. P. & Frauenrath, H. Topochemical polymerization in supramolecular polymers of oligopeptide-functionalized diacetylenes. *Angew. Chemie - Int. Ed.* **45,** 5383–5386 (2006).

12. Stone, D. a, Tayi, A. S., Goldberger, J. E., Palmer, L. C. & Stupp, S. I. Self-assembly and conductivity of hydrogen-bonded oligothiophene nanofiber networks. *Chem. Commun. (Camb).* **47,** 5702–5704 (2011).

13. Kim, S. H. & Parquette, J. R. A model for the controlled assembly of semiconductor peptides. *Nanoscale* **4,** 6940–6947 (2012).

14. Kumar, R. J., MacDonald, J. M., Singh, T. B., Waddington, L. J. & Holmes, A. B. Hierarchical self-assembly of semiconductor functionalized peptide a-helices and optoelectronic properties. *J. Am. Chem. Soc.* **133,** 8564–8573 (2011).

15. Cipriano, T. *et al.* Bioinspired peptide nanostructures for organic field-effect transistors. *ACS Appl. Mater. Interfaces* **6,** 21408–21415 (2014).

16. Ardoña, H. A. M. & Tovar, J. D. Energy transfer within responsive pi-conjugated coassembled peptide-based nanostructures in aqueous environments. *Chem. Sci.* **6,** 1474–1484 (2015).

17. Channon, K. J., Devlin, G. L. & MacPhee, C. E. Efficient energy transfer within self-assembling peptide fibers: A route to light-harvesting nanomaterials. *J. Am. Chem. Soc.* **131,** 12520–12521 (2009).

18. Nalluri, S. K. M. & Ulijn, R. V. Discovery of energy transfer nanostructures

using gelation-driven dynamic combinatorial libraries. *Chem. Sci.* **4,** 3699–3705 (2013).

19. Diegelmann, S. R., Hartman, N., Markovic, N. & Tovar, J. D. Synthesis and alignment of discrete polydiacetylene-peptide nanostructures. *J. Am. Chem. Soc.* **134,** 2028–2031 (2012).
20. Jurchescu, O. D. *et al.* Correlation between microstructure, electronic properties and flicker noise in organic thin film transistors. *Appl. Phys. Lett.* **92,** 132103 (2008).
21. Prasanthkumar, S., Gopal, A. & Ajayaghosh, A. Self-assembly of thienylenevinylene molecular wires to semiconducting gels with doped metallic conductivity. *J. Am. Chem. Soc.* **132,** 13206–13207 (2010).
22. Sun, Y. *et al.* Semiconductive, one-dimensional, self-assembled nanostructures based on oligopeptides with ??-conjugated segments. *Chem. - A Eur. J.* **17,** 4746–4749 (2011).
23. Horowitz, G. Organic field-effect transistors. *Adv. Mater.* **10,** 365–377 (1998).
24. Wall, B. D. *et al.* Aligned macroscopic domains of optoelectronic nanostructures prepared via shear-flow assembly of peptide hydrogels. *Adv. Mater.* **23,** 5009–5014 (2011).
25. Wall, B. D. *et al.* Supramolecular polymorphism: Tunable electronic interactions within π-conjugated peptide nanostructures dictated by primary amino acid sequence. *Langmuir* **30,** 5946–5956 (2014).
26. Ardoña, H. A. M., Besar, K., Togninalli, M., Katz, H. E. & Tovar, J. D. Sequence-dependent mechanical, photophysical and electrical properties of pi-

conjugated peptide hydrogelators. *J. Mater. Chem. C* 6505–6514 (2015). doi:10.1039/C5TC00100E

27. Sanders, A. M., Dawidczyk, T. J., Katz, H. E. & Tovar, J. D. Peptide-based supramolecular semiconductor nanomaterials via pd-catalyzed solid-phase 'dimerizations'. *ACS Macro Lett.* **1,** 1326–1329 (2012).

28. Sanders, A. M. & Tovar, J. D. Solid-phase Pd-catalysed cross-coupling methods for the construction of π-conjugated peptide nanomaterials. *Supramol. Chem.* **26,** 259–266 (2014).

29. Martínez Hardigree, J. F. & Katz, H. E. Through thick and thin: Tuning the threshold voltage in organic field-effect transistors. *Acc. Chem. Res.* **47,** 1369–1377 (2014).

30. Małachowski, M. J. & Żmija, J. Organic field-effect transistors. **18,** 121–136 (2010).

31. Braga, D. & Horowitz, G. High-Performance Organic Field-Effect Transistors. *Adv. Mater.* **21,** 1473–1486 (2009).

32. Generali, G. *et al.* Correlation among morphology, crystallinity, and charge mobility in OFETs made of quaterthiophene alkyl derivatives on a transparent substrate platform. *J. Phys. Chem. C* **115,** 23164–23169 (2011).

33. Kline, R. J. *et al.* Dependence of regioregular poly(3-hexylthiophene) film morphology and field-effect mobility on molecular weight. *Macromolecules* **38,** 3312–3319 (2005).

34. Kwiatkowski, J. J., Frost, J. M. & Nelson, J. The effect of morphology on electron field-effect mobility in disordered C60 thin films. *Nano Lett.* **9,** 1085–1090

(2009).

35. Wong, L. Y. *et al.* Interplay of processing, morphological order, and charge-carrier mobility in polythiophene thin films deposited by different methods: Comparison of spin-cast, drop-cast, and inkjet-printed films. *Langmuir* **26,** 15494–15507 (2010).

36. Fei, Z. *et al.* Influence of side-chain regiochemistry on the transistor performance of high-mobility, all-donor polymers. *J. Am. Chem. Soc.* **136,** 15154–15157 (2014).

37. Noriega, R. *et al.* A general relationship between disorder, aggregation and charge transport in conjugated polymers. *Nat. Mater.* **12,** 1038–1044 (2013).

38. Tsai, W. W., Tevis, I. D., Tayi, A. S., Cui, H. & Stupp, S. I. Semiconducting nanowires from hairpin-shaped self-assembling sexithiophenes. *J. Phys. Chem. B* **114,** 14778–14786 (2010).

39. Bonetti, S. *et al.* A lysinated thiophene-based semiconductor as a multifunctional neural bioorganic interface. *Adv. Healthc. Mater.* **4,** 1190–1202 (2015).

40. Alesi, S. *et al.* Water-Soluble, Electroactive, and Photoluminescent Quaterthiophene–Dinucleotide Conjugates. *Chem. - A Eur. J.* **14,** 513–521 (2008).

41. Lin, Y. A.; Ou, Y. C.; Cheetham, A. G.; Cui, H. G. Supramolecular Polymers Formed by ABC Miktoarm Star Peptides. *ACS Macro Lett.* 1088–1094 (2013). doi:10.1016/j.surg.2006.10.010.Use

42. Unni, K. N. N., Dabos-Seignon, S. & Nunzi, J.-M. Influence of the polymer

dielectric characteristics on the performance of a quaterthiophene organic field-effect transistor. *J. Mater. Sci.* **41,** 1865–1871 (2006).

43. Hajlaoui, R. *et al.* Improved field-effect mobility in short oligothiophenes. Quaterthiophene and quinquethiophene. *Adv. Mater. (Weinheim, Ger.)* **9,** 389–391 (1997).

44. Draper, E. R. *et al.* Air-stable photoconductive films formed from perylene bisimide gelators. *J. Mater. Chem. C* **2,** 5570–5575 (2014).

45. Kraus, M. *et al.* High-mobility copper-phthalocyanine field-effect transistors with tetratetracontane passivation layer and organic metal contacts. *J. Appl. Phys.* **107,** 1–7 (2010).

46. Nishinari, K., Shibuya, N. & Kainuma, K. Dielectric relaxation in solid dextran and pullulan Temperature in " C. *New York* **438,** 433 – 438 (1985).

47. Amit, M. *et al.* Hybrid proton and electron transport in peptide fibrils. *Adv. Funct. Mater.* **24,** 5873–5880 (2014).

Chapter 6

Conclusion and Future Outlook

In our studies we have investigated unique application challenges and have successfully developed solutions based on organic electronics. The applications focused on capabilities of organic semiconducting materials that are not as readily available using Si based technology. The important message here is that these materials have huge range of untapped potential applications, which don't have to be in the area of traditional semiconducting applications.

The scope of our work is to establish organic field effect transistors as a viable platform for sensing and for interfacing between biological and electronic materials. The strategies and the results discussed here open new pathways for the future development of these areas

In our ammonia sensor project, we succeeded in increasing organic field-effect transistor (OFET) NH_3 response using tris- (pentafluorophenyl)borane (TPFB) as a receptor. OFETs with this additive could detect concentrations of 450 ppb v/v, with a limit of detection of 350 ppb, the highest sensitivity reported to date for semiconductor films. Taking this project further, we developed a fully printable ammonia sensor, simplified by replacing the gate electrode and dielectric deposition steps with the introduction of static charges on the back surface of the PET substrate by corona charging, a procedure that is adaptable to roll-to-roll processing. This technique considerably decreased the time and cost of production. After cost and sensitivity, the next big challenge for these sensors is retention of

response. To address that, we propose a bistable circuit using two inverter devices with DPP-CN as the N arm and PQT-12 as the P arm. Integration of such sensors in a wearable platform and interfacing them with an electronic log and alarm system to announce any critical concentration will make them more user friendly and should be the next step for achieving our goal of establishing this technology as a viable NH_3 sensing platform.

We successfully developed an ethylene sensor by using palladium particles as a receptor for ethylene. Using this strategy, we could detect 50 ppm of ethylene gas. In order to achieve the required sub ppm level detection, we propose to introduce pores in the semiconductor films using thermal porogenes like Tert-butyl phenyl carbonate and N-(tert-butoxy-carbonyloxy)-phthalimide. Considering the need for viable ethylene detection in the horticulture industry and the lack of any suitable practical options, OFET sensing platform appears to be a suitable choice for resolving this challenge.

For the biosensor project, we designed a new receptor–antibody-functionalized top dielectric layer. This layer, incorporating both a fluorinated polymer and vapor-deposited hydrocarbon, provided maximum capacitive coupling and minimal interference from the aqueous analyte solution, and allowed convenient solvent processing of the antibody-coupling layer. Additionally, a new antibody immobilization method was introduced, which led to high immobilization yield and surface coverage. Using glial fibrillary acidic protein (GFAP) as a model protein analyte, this sensor platform demonstrated significant selectivity and recognition of target protein even in much more concentrated non-target protein backgrounds. We

explicitly verified for the first time that the response is in fact predominantly from perturbations of TFT channel current. To the best of our knowledge, this is the most sensitive organic TFT (OTFT) protein sensor yet reported, and also the first demonstration of the expected opposite current responses by p- and n-channel semiconductors to the same protein. Although a significant sensitivity was achieved, there are considerable challenges remaining. To make this technology more viable, we still need to increase the sensitivity by three orders of magnitude, perhaps by increasing the interaction area by forming pores in the active layer, further optimizing the capacitive coupling layer, or leveraging a floating gate approach that keeps the sensing and signaling functions spatially apart.

Finally, we electrically functionalized self-assembling nanowires and established a bio-interface between electrically active cores and bio-compatible amino acid sheaths. We studied the effect of systematic changes in amino acid composition on the semiconducting/conducting functionality of the nanostructures. The study shows that these peptides that self-assemble in aqueous environments can be used successfully to transmit electronic signals over biologically relevant distances. This library of nanowires should be instrumental in electrically manipulating and stimulating cells for bioengineering purposes, and could also ultimately act as sensing elements in their own right.

Appendix A

Supporting Information for Chapter 4

A.1 Interdigitated Shadow Mask

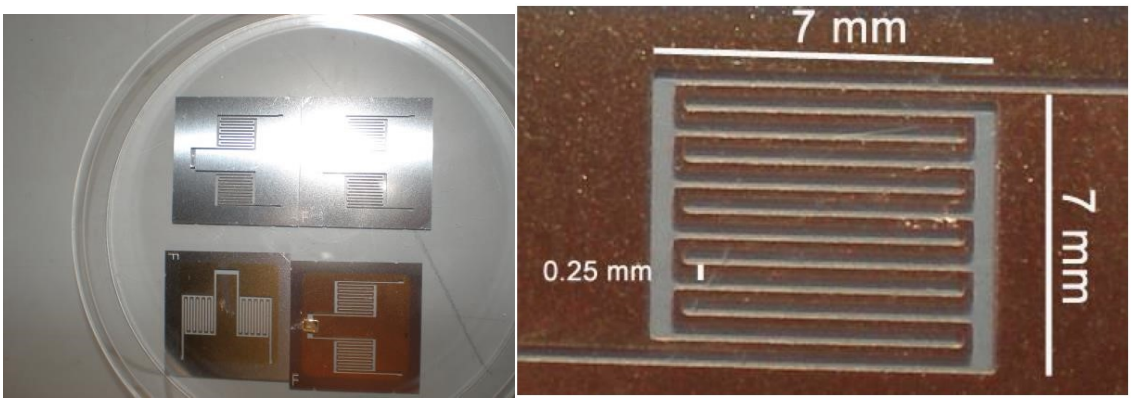

Figure S1 Interdigitated shadow mask used for depositing source and drain electrodes.

A.2 AFM Study of Top Capacitive Coupling Dielectric Surface

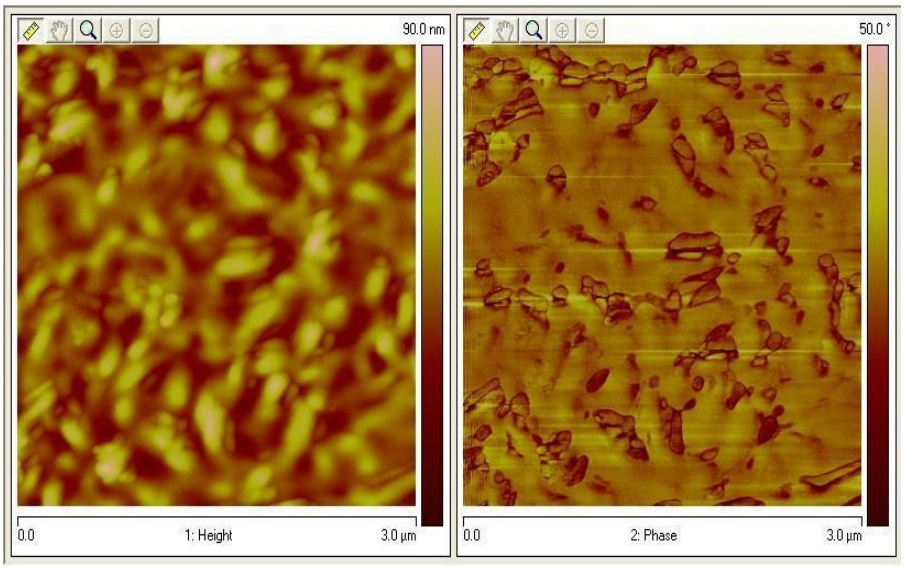

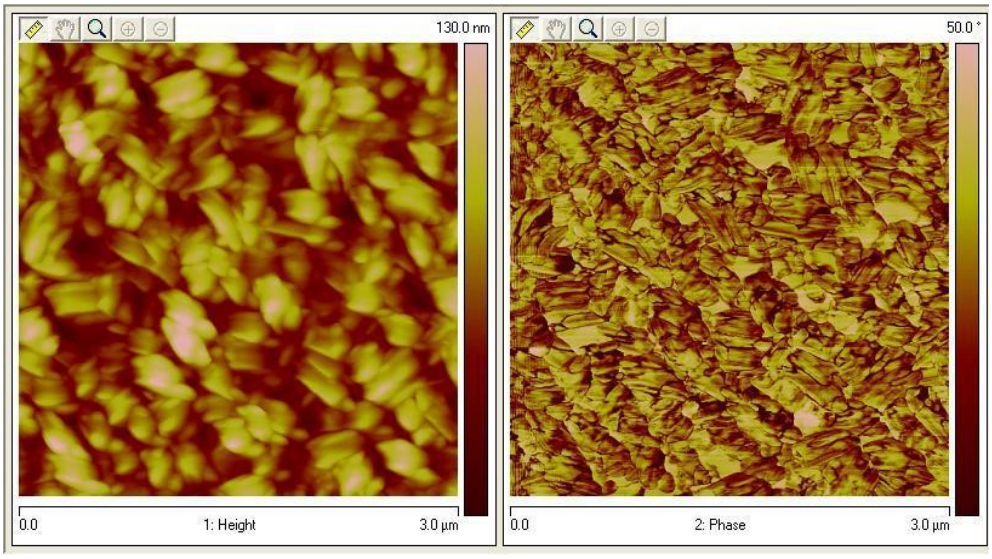

Figure S2 AFM image of CYTOP (above) and CYTOP+C44 combined film (below).

A.3 Capacitance Study of Top Capacitive Coupling Dielectric Layer

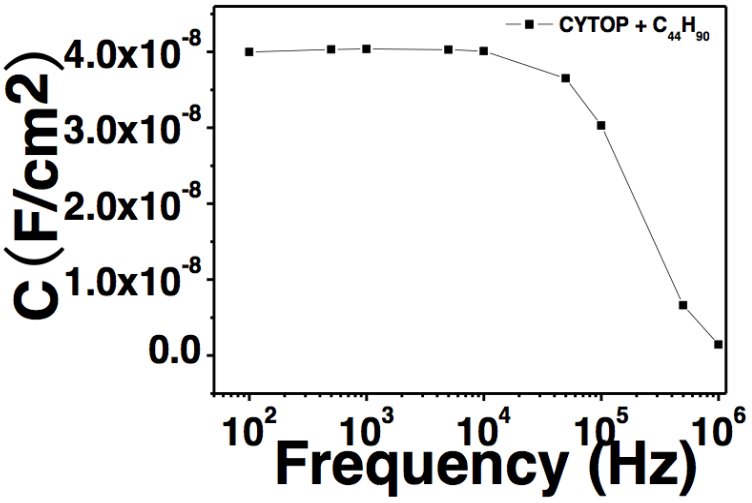

Figure S3 Capacitance of CYTOP+C44 layer at different frequency.

A.4 Electrical Properties of Pentacene and 8-3 NTCDI Transistor and Inverter Under Different Conditions.

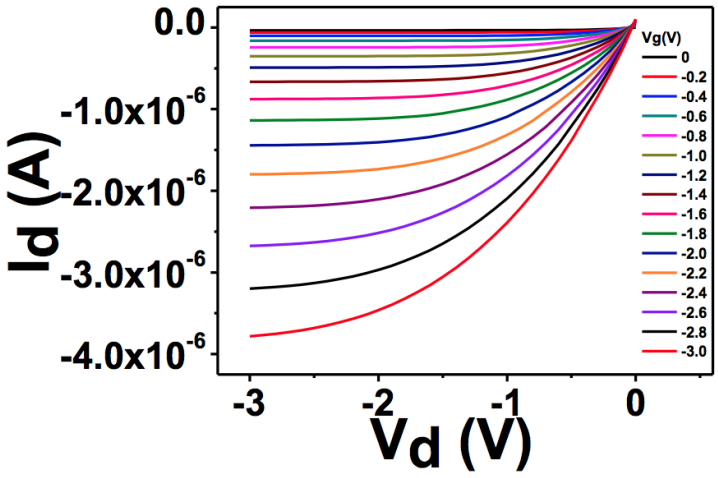

a) Typical output curve for pentacene OTFT (tested in air) without CYTOP.

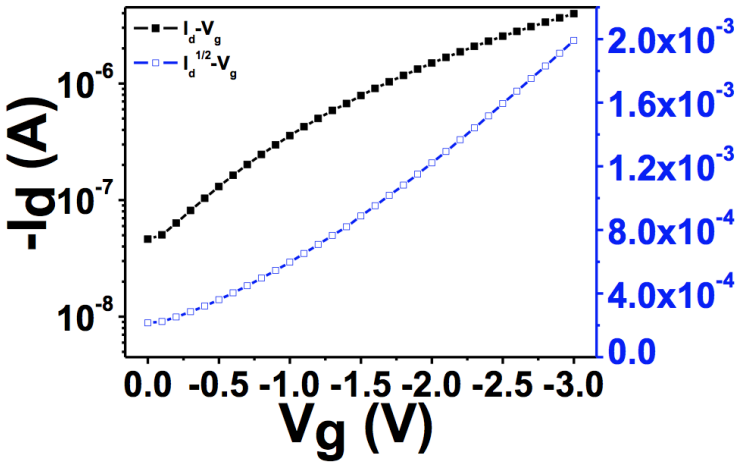

b) Typical transfer curve for pentacene OTFT (tested in air) without CYTOP.

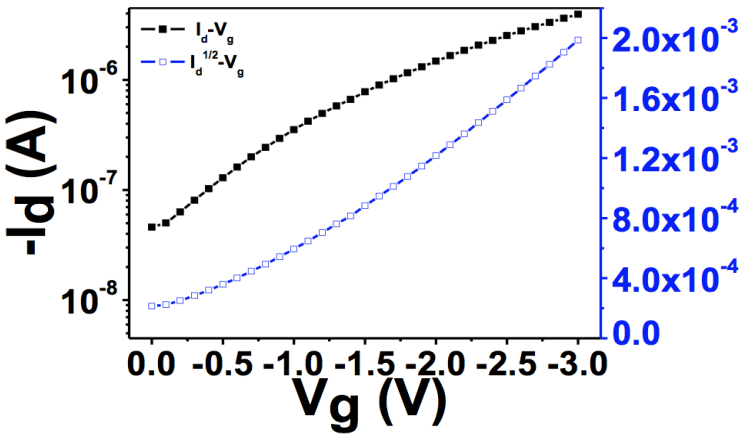

c) Typical transfer curve for pentacene OTFT (tested in air) with CYTOP.

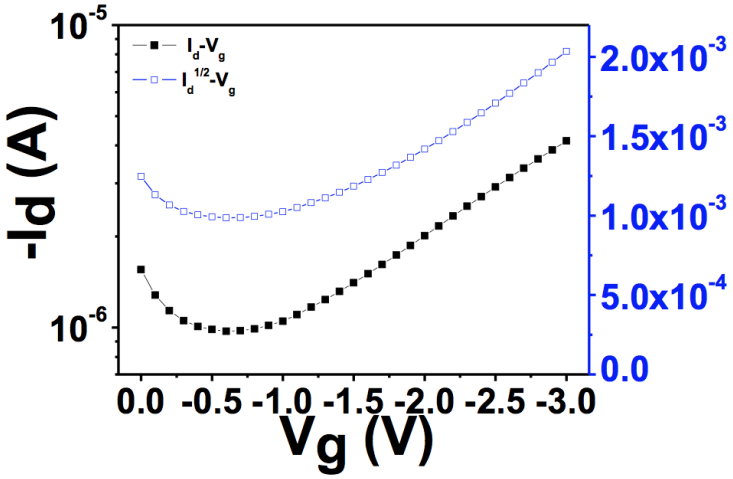

d) Typical transfer curve for pentacene (tested after 20 minutes in 0.05 pbs) with CYTOP and all the following layers (C_{44}, PS-block-PAA, antibody).

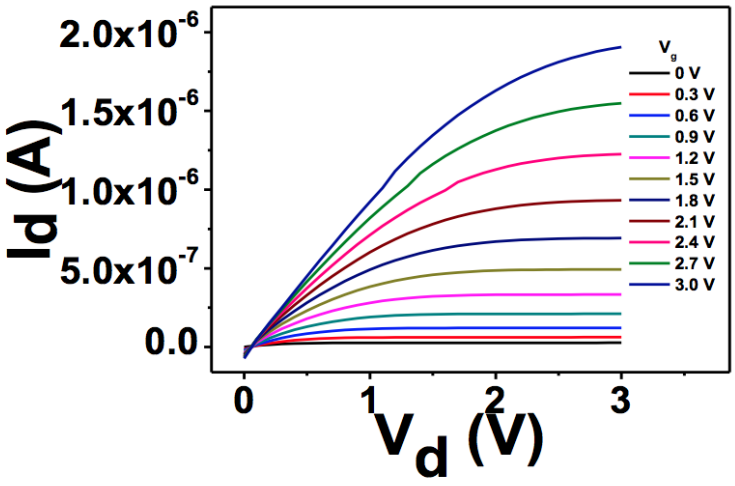

e) Typical output curve for 8-3 NTCDI (tested in air) without CYTOP**.**

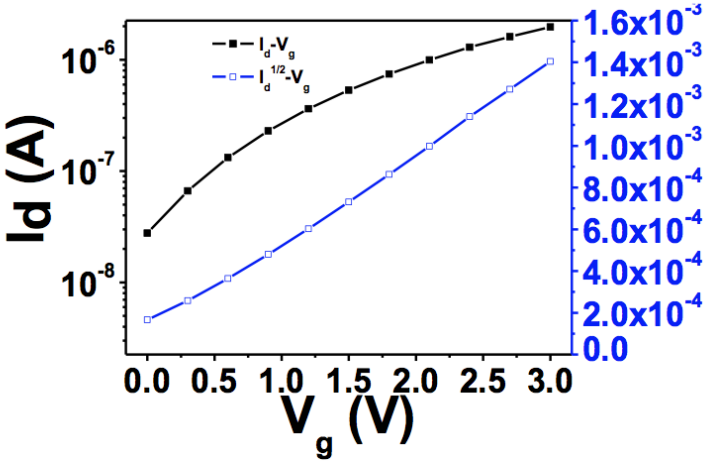

f) Typical transfer curve for 8-3 NTCDI (tested in air) without CYTOP.

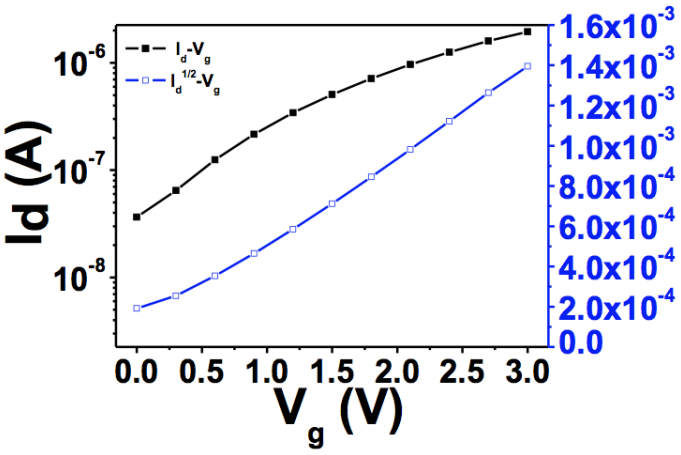

g) Typical transfer curve for 8-3 NTCDI (tested in air) with CYTOP.

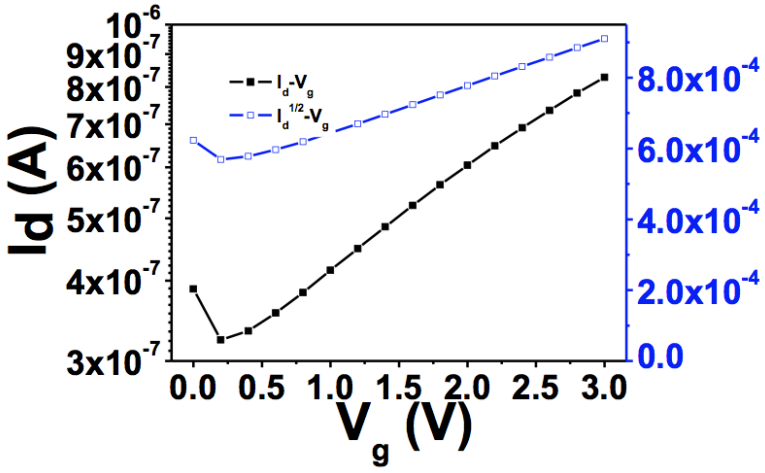

h) Typical transfer curve of 8-3 NTCDI (tested after 20 minutes in 0.5 pbs) with CYTOP and all the following layers (C_{44}, PS-block-PAA, antibody).

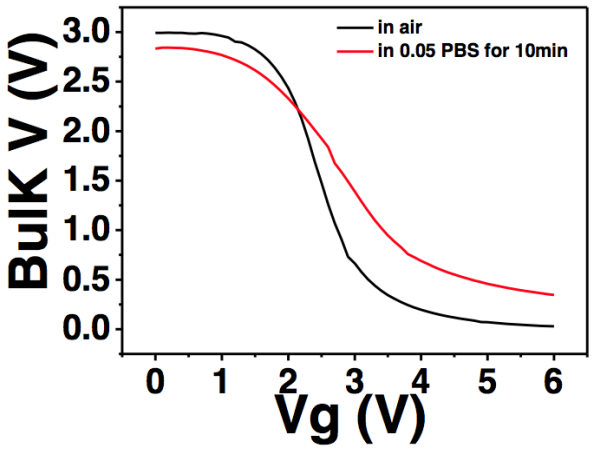

i) Typical bulk V/Vg for pentacene/8-3 NTCDI under different conditions.

Figure S4 (a-i) Electrical properties of pentacene and 8-3 NTCDI transistor and inverter under diffrent conditions.

A.5 Confirming the Attachment of Anti-GFAP

In order to confirm that the antibody is successfully attached to the device surface by EDC/NHS- based bioconjugation chemistry, we labeled the antibody with rhodamine B, and then attached the labeled antibody on the device surface, using the detailed procedure shown in Scheme S1. First, we activate the carboxyl group on rhodamine B with EDC and NHS, then attach the activated rhodamine B to the antibody by the reaction of N-hydroxysuccinimide on the dye and amine groups on the antibody. Finally, the labeled antibodies were attached to the device surface by EDC/NHS based bioconjugation chemistry. The surface was then gently rinsed with PBS to remove any non-covalently unattached antibody. In Scheme S1 we can see orange fluorescence on sample A and B (both are after the reaction of rhodamine B labeled antibody with EDC/NHS-activated device surface), while no fluorescence on

sample C (applying EDC/NHS activated rhodamine B on a control hydroxyethylated device surface).

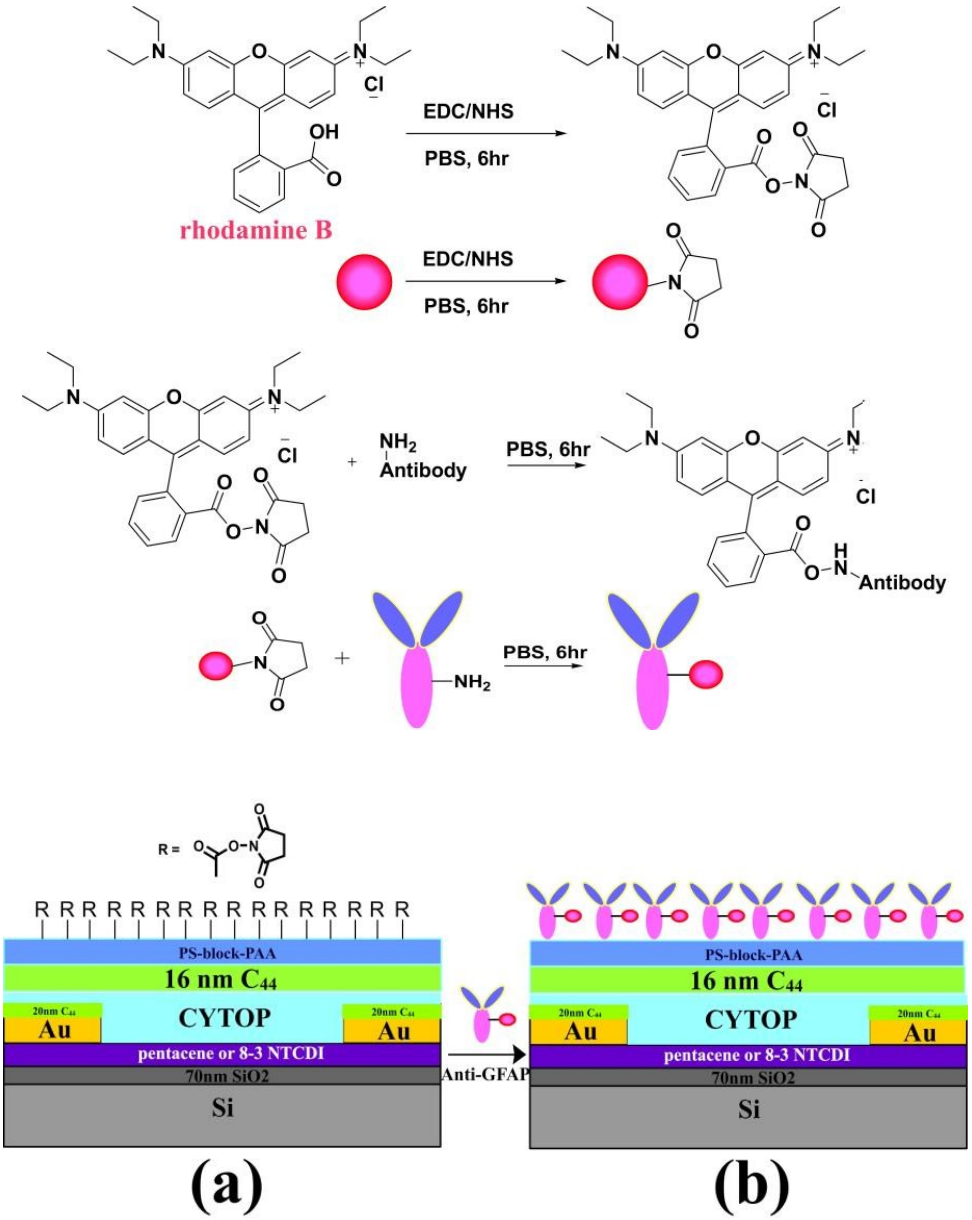

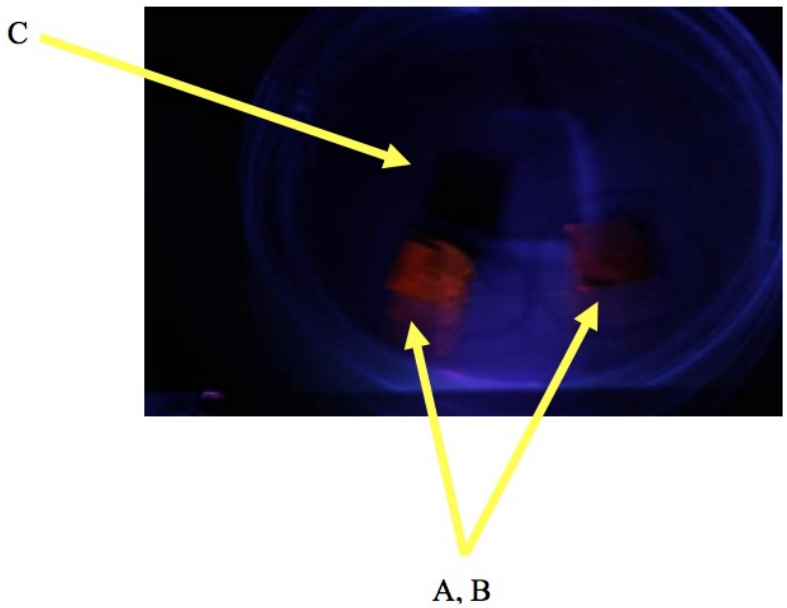

Scheme S1 The synthesis route for Rhodamine-labeled antibody and image of fluorescent-labeled antibody attachment on the NHS-treated PS-block-PAA surface (sample and B), with no attachment on control sample C.

A.6 Langmuir Model for calculating the affinity constant of Anti-GFAP and GFAP

$$\theta = x/x_o$$

Where θ is fractional surface coverage, x_o is total available binding sites on the device surface, x is occupied binding sites;

$$\nu_a = k_a c(1-\theta)$$

ν_a is adsorption rate, k_a is the rate constant for adsorption;

$$\nu_d = k_d \theta$$

ν_d is desorption rate, k_d is the rate constant for desorption;

After reach equilibrium statement, $v_a = v_d$, then we can get:

$$\theta = Kc/(1+Kc);\ (K= k_a/k_d)$$

$$1/x = (1/x_mK)\ 1/c+1/x_m \text{ ---------- } \textbf{equation S1}$$

By fitting Figure 4 (b) and (d) into equation S1, then we can get a rough affinity constant value.

Appendix B

Supporting information for chapter 5

B.1 Peptide Synthesis

B.1.1 General Considerations

The chemicals used for 9fluorenylmethoxycarbonyl (Fmoc)-based solid phase peptide synthesis (*N*-methylpyrrolidone (NMP), *O*-(benzotriazol-1-yl)-*N,N,N',N'*-tetramethyluronium hexafluorophosphate (HBTU), benzotriazol-1-yl-oxytripyrrolidinophosphonium hexafluorophosphate (PyBOP), *N,N*-diisopropylethylamine (DIPEA), Wang resin, and Fmoc-protected amino acids) were obtained from Oakwood Products, Inc. or Advanced ChemTech. Tetrahydrofuran (THF) was obtained from an Innovative Technologies PureSolv solvent purification system and stored over 4Å molecular sieves (Sigma-Aldrich). *N,N*-dimethylformamide (DMF) was obtained from either Sigma-Aldrich or EMD Millipore Chemicals. DIPEA, THF and DMF were degassed by sparging with nitrogen (N_2) gas for one hour prior to use. Tetrakis(triphenylphosphine)palladium ($Pd(PPh_3)_4$) was obtained from Strem Chemicals. The Biotech-grade cellulose ester dialysis tubings (MWCO 500-1000), with flat widths of either 16-mm or 31-mm were obtained from Spectrum Labs. All other reagents and starting materials were obtained from Sigma-Aldrich and were used as received. 5-bromothiophene-2-carboxylic acid and 5,5'-bis-tributylstannyl-[2,2']-bithiophene were prepared using literature procedures[1]. The ^{1}H-NMR spectra were obtained using a Bruker Avance 400 MHz (unless otherwise stated) and the data was processed using Bruker Topsin

1.3. Chemical shifts are reported in parts per million relative to residual protio solvent [d_6-DMSO δ: 2.50, D_2O δ: 4.79 (^{1}H NMR)]. The tabulated values for NMR peaks may not reflect the theoretical number of protons expected due to some aggregation previously observed for these materials under basic to neutral conditions[2].

B.1.2 General Solid Phase Peptide Synthesis (SPPS)

All peptides were synthesized using the standard Fmoc solid-phase technique with Wang resin pre-loaded with the terminal amino acid (Wang-Asp= 0.6 mmol/g). To the resin in a peptide chamber, Fmoc-deprotection was accomplished by adding a (1:4) piperidine/DMF solution twice (successive 5- and 10-minute treatment) and then washing with NMP, methanol and dichloromethane (DCM). For the amino acid couplings, 3.0 eq. of the Fmoc-protected amino acid (1.0 eq of the Fmoc-deprotected peptide bound to the resin) underwent external activation with 2.9 eq. of HBTU and 10 eq. DIPEA. The activated amino acid mixture was mixed for one minute prior to addition in the peptide chamber. The reaction mixture was allowed to mix for 60-120 minutes, after which was rinsed with NMP, methanol and DCM. The completion of all couplings was monitored using a Kaiser test on a few dry resin beads, repeating same amino acid coupling as needed. The general procedure for amino acid coupling was repeated until the desired peptide sequence was obtained.

B.1.3 General N-Acylation Procedure for Peptides

Following a procedure reported in the literature[1], a solution containing 2.1 eq. of 5-bromothiophene-2-carboxylic acid that was activated by HBTU (2.0 eq.) with DIPEA

(10 eq.) was mixed for 180 minutes with the resin containing the completed peptide sequence. The resin was rinsed with NMP, methanol and DCM. The resin was treated again with 1.1 eq. of 5-bromothiophene-2-carboxylic acid that was activated by HBTU (1.0 eq.) with DIPEA (10 eq.) for 60 minutes. After rinsing the resin with the standard wash cycle (NMP-methanol-DCM), completion was assessed using a Kaiser test on a few dry resin beads. Treatment with 1.1 eq. of the activated 5-bromothiophene-2-carboxylic acid was repeated as needed.

B.1.4General On-Resin Stille Coupling Procedure

Following a procedure reported in the literature[1], the *N*-acylated peptide made by following the general procedures described above were transferred to a Schlenk flask topped with a reflux condenser. The dried resin with $Pd(PPh_3)_4$ (4.0 mol % relative to the amino acid loading in the resin) was kept in the Schlenk flask under a nitrogen (N_2) atmosphere (~10-20 mTorr). In a separate vessel, a ~15 mM solution of 5,5'-bis-tributylstannyl-[2,2']-bithiophene was prepared in DMF. This was then added to the reaction flask via syringe. The reaction mixture was heated up to 80°C while agitating by constantly bubbling nitrogen (N_2) gas in the solution. The said conditions were maintained for 16 hours, and then the reaction mixture was allowed to cool to room temperature. The resin was washed with DMF (3×) in a peptide chamber, followed by the standard wash cycle. The synthesized π-conjugated peptides were then subjected to cleavage procedure.

B.1.5 General Cleavage Procedure for Peptides

The cleavage cocktail was prepared with 9.5 mL of trifluoroacetic acid, 250 µL Milli-Q water, and 250 µL of triisopropylsilane. The resin was treated with 10 mL of cleavage cocktail in a peptide chamber for 3 hours. The filtrate was drained and the resin was washed with DCM (3×). The filtrate was concentrated under reduced pressure. The crude peptide was precipitated out of the filtrate by adding 90 mL of cold Et_2O, allowing the suspension to sit for 5 minutes at 4°C. The pellet formed was isolated by centrifugation, followed by decanting the solvent and drying the solid formed. The pellet was redissolved in Milli-Q water with a few drops of ammonium hydroxide (to completely dissolve the solid) and was subjected to lyophilization. All peptides (both crude and purified) were stored as lyophilized solids at 4°C.

DGG-4T Peptide (HO-DGG-4T-GGD-OH). Prepared according to literature procedure;[3] characterization matched that of literature.

DAA-4T Peptide (HO-DAA-4T-AAD-OH). Prepared according to literature procedure;[3] characterization matched that of literature.

DVV-4T Peptide (HO-DVV-4T-VVD-OH). Prepared according to literature procedure;[3] characterization matched that of literature.

DII-4T Peptide (HO-DII-4T-IID-OH). Prepared according to literature procedure[3]; characterization matched that of literature.

EGG-4T Peptide (HO-EGG-4T-GGE-OH). Solid-supported Wang-EGG-NH_2 peptide *N*-acylated with 5-bromothiophene-2-carboxylic acid was prepared (0.5 mmol). The peptide was coupled with 5,5'-bis-tributylstannyl-[2,2']-bithiophene (0.25 mmol,

0.186 g) in the presence of $Pd(PPh_3)_4$ (0.02 mmol, 0.023 g) using the general on-resin Stille coupling procedure for 14 hours. Resin was then subjected to the general cleavage procedure. Crude peptide obtained was observed as an orange powder (0.077 g, 34%). MS (ESI-) *m/z* 925.3 ($M-2H^+ + Na^+$) (calc. 925.1), *m/z* 903.3 ($M-H^+$) (calc. 903.1), *m/z* 451.3 ($M-2H^+$) (calc. 451.1). ^1H NMR (600 MHz, D_2O) δ, ppm: 8.37 (d, 1H, *J*= 3.6 Hz), 7.53 (s, 1H), 7.21 (s, 1H), 7.14 (d, 2H, *J*= 15.6 Hz), 4.11-4.08 (m, 1H), 4.05 (d, 1H, *J*= 3.0 Hz), 3.93 (d, 1H, *J*= 3.0 Hz), 2.20-2.17 (m, 1H), 2.05-2.00 (m, 1H), 1.89-1.84 (m, 1H).

EAA-4T Peptide (HO-EAA-4T-AAE-OH). The synthesis for **EAA-4T** peptide was adapted from ref. [4], with the exception that the resin was not washed with DMF, isopropanol, water, THF, acetonitrile, ether and hexanes prior to cleavage. Crude peptide obtained was observed as an orange powder; characterization matched that of literature.

EVV-4T Peptide (HO-EVV-4T-VVE-OH). Solid-supported Wang-EVV-NH_2 peptide *N*-acylated with 5-bromothiophene-2-carboxylic acid was prepared (0.5 mmol). The peptide was coupled with 5,5'-bis-tributylstannyl-[2,2']-bithiophene (0.25 mmol, 0.186 g) in the presence of $Pd(PPh_3)_4$ (0.02 mmol, 0.023 g) using the general on-resin Stille coupling procedure for 15 hours. Resin was then subjected to the general cleavage procedure. Crude peptide obtained was observed as an orange powder (0.102 g, 38%). MS (ESI-) *m/z* 1109.5 ($M-2H^+ + K^+$) (calc. 1109.3), *m/z* 1071.7 ($M-H^+$) (calc. 1071.3), *m/z* 535.5 ($M-2H^+$) (calc. 535.2). ^1H NMR (600 MHz, D_2O) δ, ppm: 8.37 (dd, 1H, *J*= 1.2 Hz), 7.59 (d, 1H, *J*= 3.6 Hz), 7.25 (s, 1H), 7.19 (m, 2H), 4.20 (dd, 2H, *J*= 8.4 Hz, 2.7 Hz), 4.13 (dd, 2H, *J*= 7.8 Hz, 2.7 Hz), 4.09-4.07 (m,

2H), 2.12 (t, 6H, *J*= 8.1 Hz), 2.07-2.03 (m, 5H), 1.96-1.94 (m, 3H), 1.84-1.80 (m, 3H), 0.95 (d, 8H, *J*= 3.0 Hz), 2.12 (t, 24H, *J*= 6.6 Hz).

EII-4T Peptide (HO-EII-4T-IIE-OH). Solid-supported Wang-EII-NH_2 peptide N-acylated with 5-bromothiophene-2-carboxylic acid was prepared (0.5 mmol). The peptide was coupled with 5,5'-bis-tributylstannyl-[2,2']-bithiophene (0.25 mmol, 0.186 g) in the presence of $Pd(PPh_3)_4$ (0.02 mmol, 0.023 g) using the general on-resin Stille coupling procedure for 16 hours. Resin was then subjected to the general cleavage procedure. Crude peptide obtained was observed as yellow/orange powder (0.055 g, 19%). MS (ESI-) *m/z* 1149.6 ($M-2H^+ + Na^+$) (calc. 1150.4), *m/z* 1127.7 ($M-H^+$) (calc. 1127.4), *m/z* 5-=63.5 ($M-2H^+$) (calc. 563.2). ^1H NMR (400 MHz, d_6-DMSO) δ, ppm: 8.48 (d, 1H, *J*= 8.8 Hz), 8.00 (d, 1H, *J*= 8.8 Hz), 7.96 (d, 1H, *J*= 7.2 Hz), 7.92 (d, 1H, *J*= 4.0 Hz), 7.42 (d, 1H, *J*= 4.0 Hz), 7.38 (dd, 2H, *J*= 4 Hz, 2.6 Hz), 4.35 (t, 1H, *J*= 9.00 Hz), 4.20-4.14 (m, 2H), 2.28-2.23 (m, 2H), 1.91-1.74 (m, 4H), 1.49-1.44 (m, 2H), 1.23-1.04 (m, 2H), 0.87-0.78 (m, 12H).

DVV-C10 Peptide (HO-DVV-$(CH_2)_{10}$-VVD-OH). 0.0288 g (0.125 mmol) of dodecanedioic acid and 0.0650 g (0.125 mmol) of PyBOP was dissolved in 10-mL of 2:1 NMP:DCM solution, after which 0.522 mL of DIPEA was gradually added then mixed for one minute. This solution was added to the solid-supported Wang-DVV-NH_2 (0.25 mmol) in a peptide chamber and mixed for 12 h. Resin was rinsed using the standard wash cycle. The general cleavage procedure was followed, only that the cleavage cocktail was diluted in a 1:1 ratio DCM and was mixed with the resin for 2 h. Crude peptide was obtained as a white powder (0.0565 g, 53%). MS (ESI-) *m/z* 893.5 ($M-2H^+ + K^+$) (calc. 893.6), *m/z* 427.2 ($M-2H^+$) (calc. 427.3). ^1H NMR (400 MHz,

d_6-DMSO) δ, ppm: 7.83 (m, 2H), 7.72 (br), 7.71 (br), 4.24-4.12 (ddd, 4H, *J*= 32. 4 Hz, 8.8 Hz, 7.2 Hz), 2.17-2.10 (m, 2H), 2.03-1.97 (m, 2H), 1.47 (t, 2H, *J*= 9.2 Hz), 1.22 (s, 6H), 0.85-0.81 (m, 12H).

B.2 Peptide Characterization

B.2.1 Spectroscopic Study of 4T-peptides

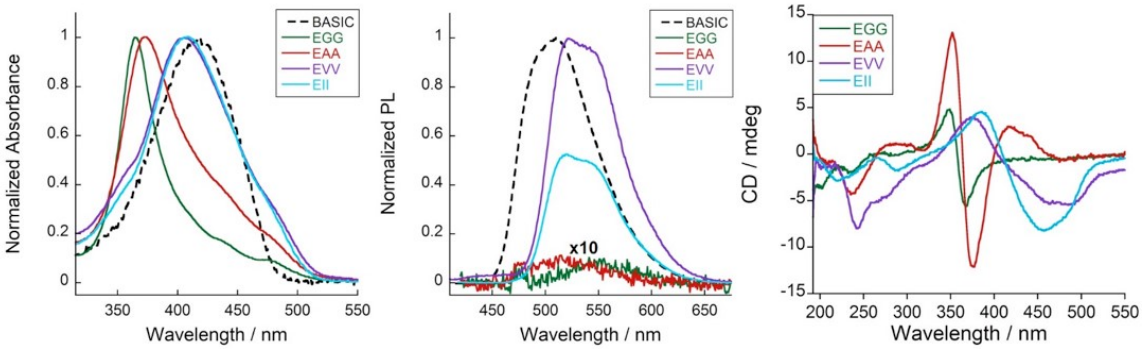

Figure S5 (a) Absorption, (b) emission (λ_{exc}= nm) (~14 μM), and (c) circular dichroism spectra (~6 μM) of 4T-peptides in basic (*ca.* pH 10, ---) and acidic (*ca.* pH 2,---).

Peptide-4T	λ_{max} / nm
DGG	362
DAA	366
DVV	403
DII	408
EGG	361
EAA	374
EVV	406
EII	409

Table S1 Absorption maxima of DXX-4T and EXX-4T peptides.

B.2.2 Transmission Electron Microscopy Images of 4T-peptides

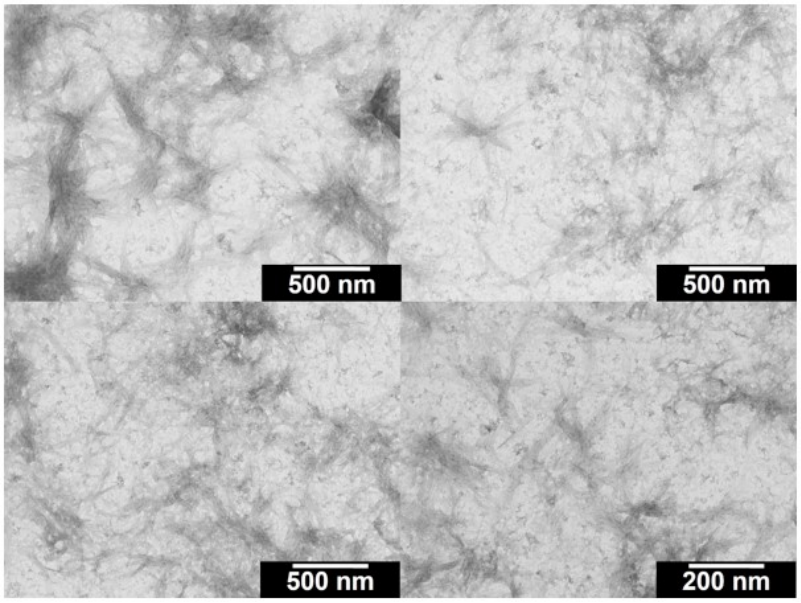

Figure S6 TEM images of 1 wt% DGG-4T peptide gel.

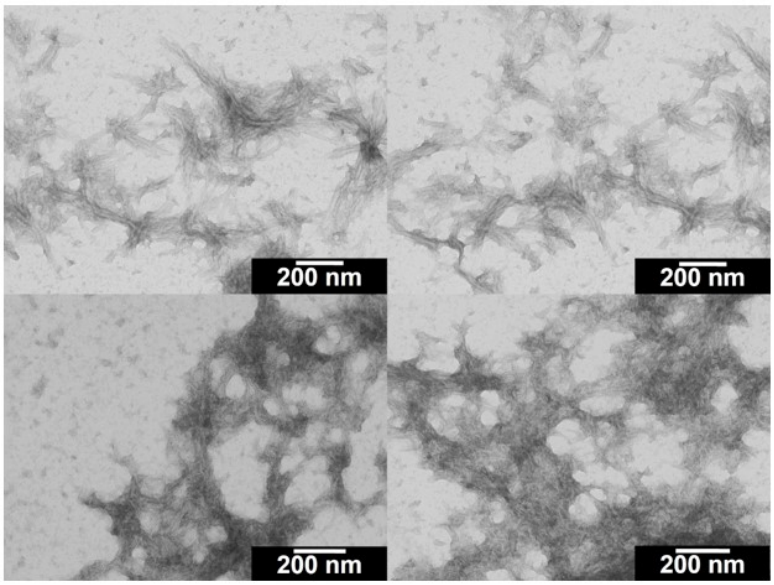

Figure S7 TEM images of 1 wt% DAA-4T peptide gel.

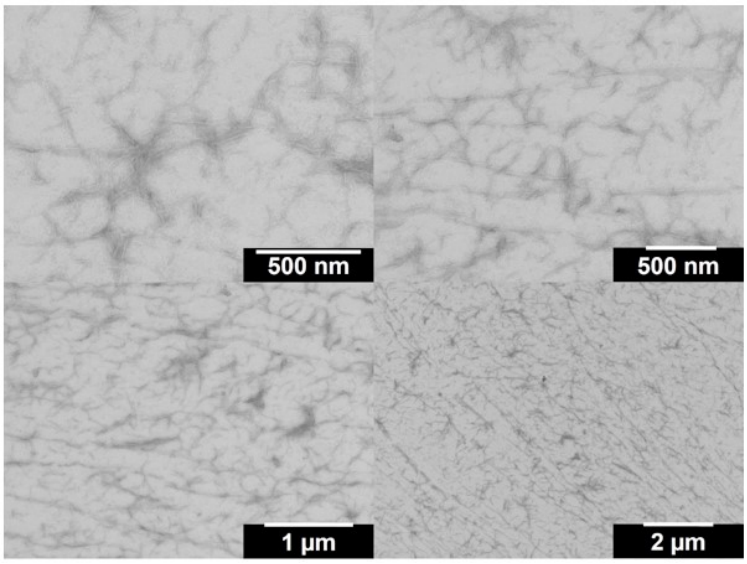

Figure S8 TEM images of 1wt% DVV-4T peptide gel.

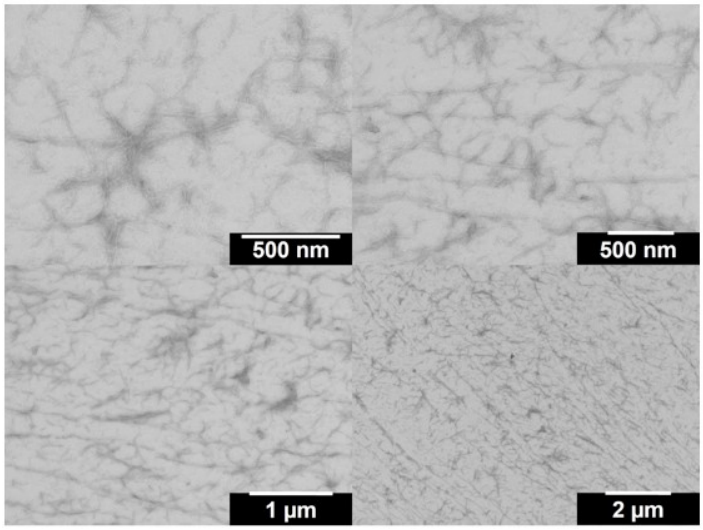

Figure S9 TEM images of 1 wt% DII-4T peptide gel.

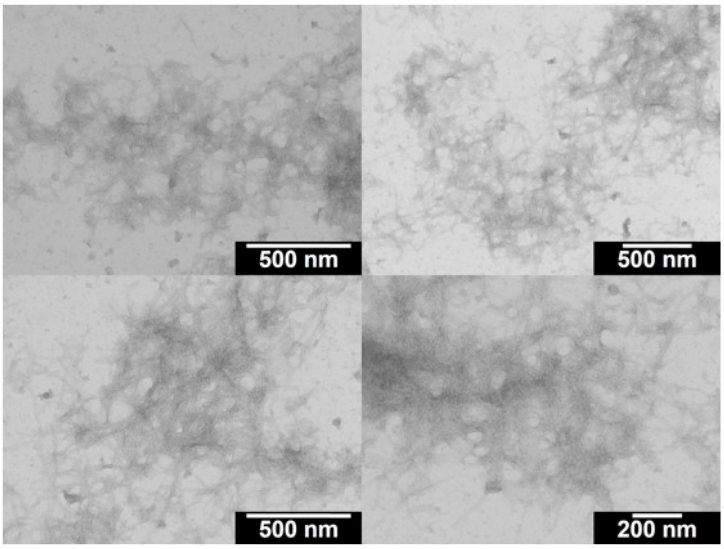

Figure S10 TEM images of 1 wt% EGG-4T peptide gel.

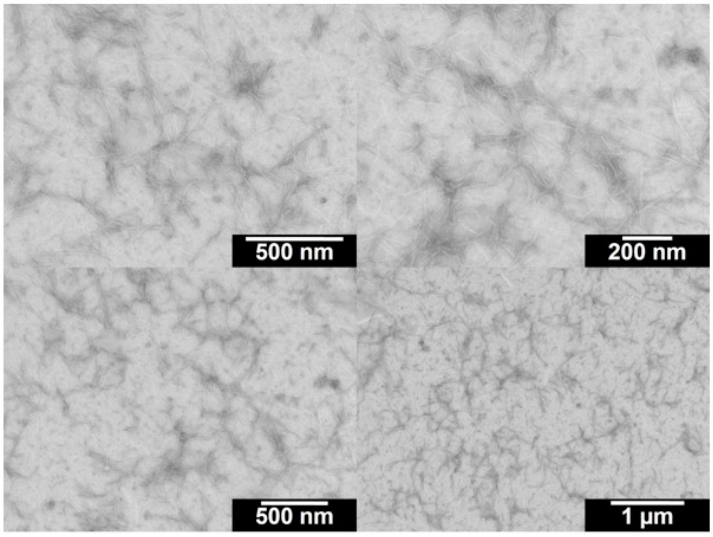

Figure S11 TEM images of 1 wt% EAA-4T peptide gel.

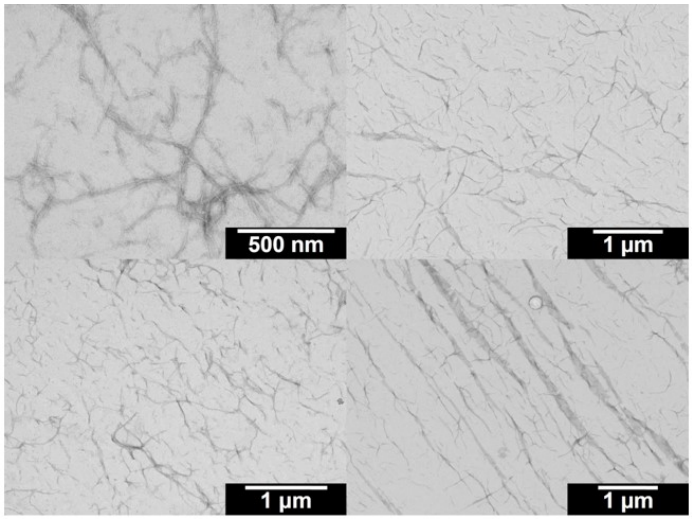

Figure S12 TEM images of 1 wt% EVV-4T peptide gel.

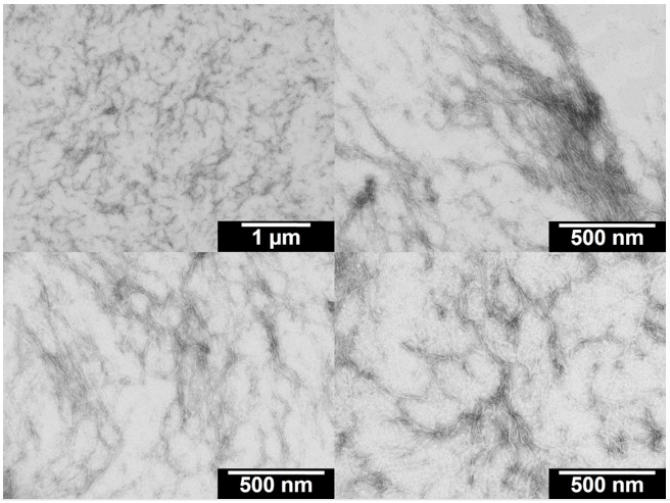

Figure S13 TEM images of 1 wt% EII-4T peptide gel

B.2.3 Atomic Force Microscopy

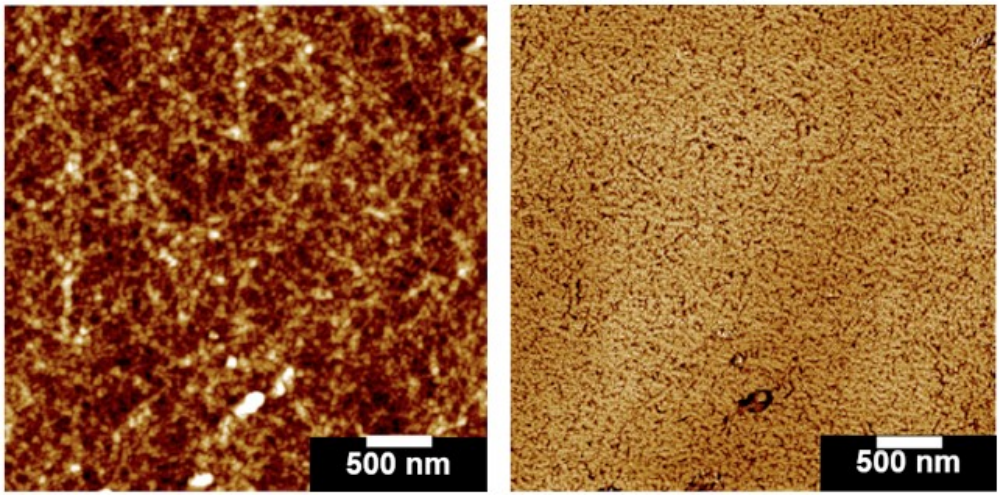

Figure S14 Representative AFM image for acidified 0.1 mg/mL EVV-4T dropcast film; hieght (left) and phase (right) profiles.

B.2.4 Laser Microscope Images of 4T-Peptides

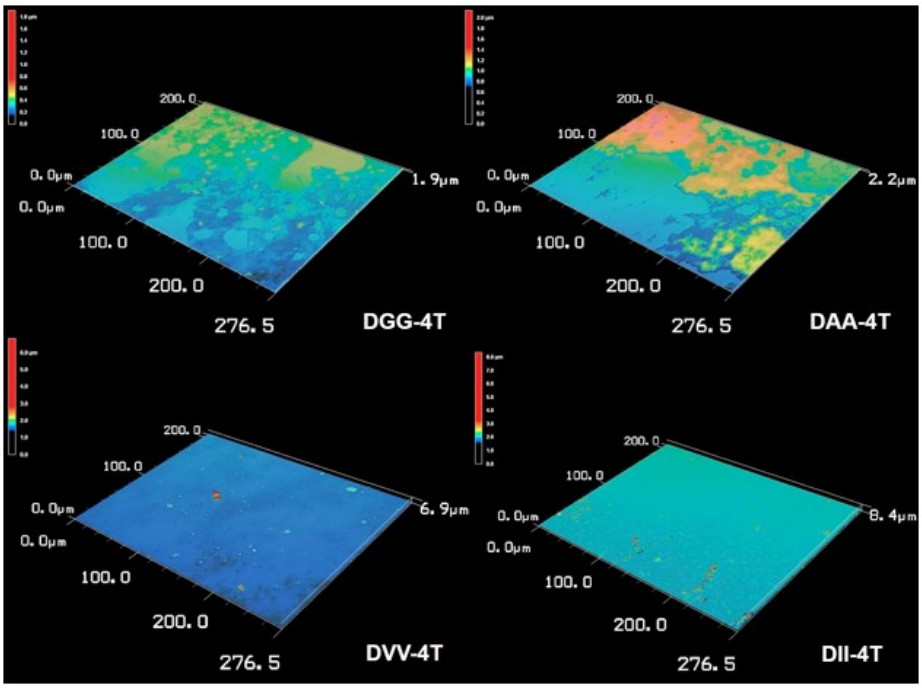

Figure S15 3D surface profiles of 1wt% DXX-4T peptide films generated from laser microscopy observation.

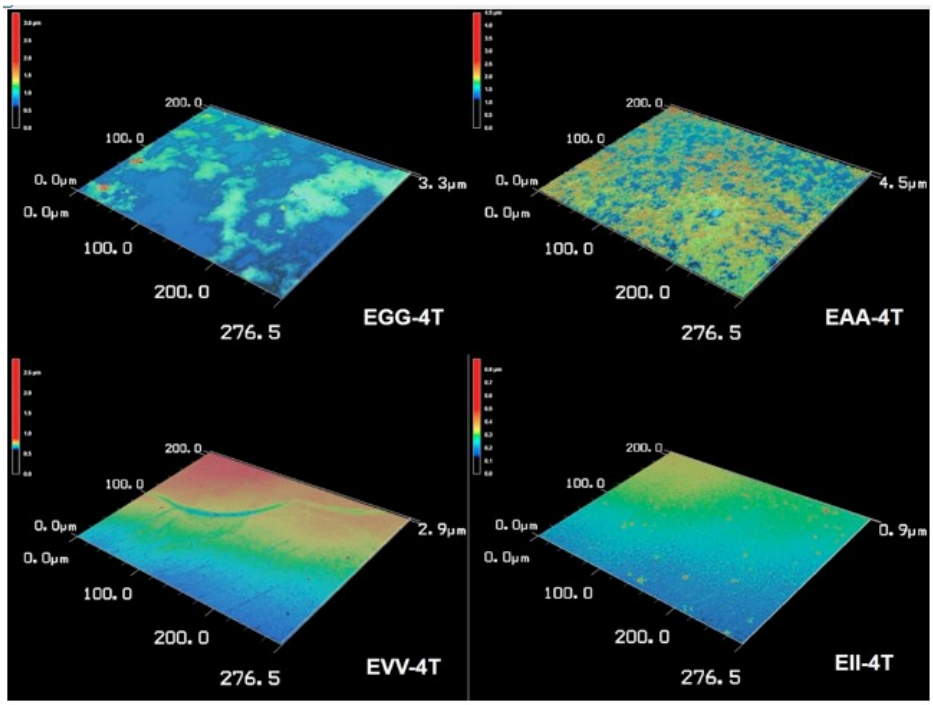

Figure S16 3D surface profiles of 1 wt% EXX-4T peptide films generated from laser microscopy observation.

B.2.5 Transmission Electron Microscopy Images of Control-Peptides

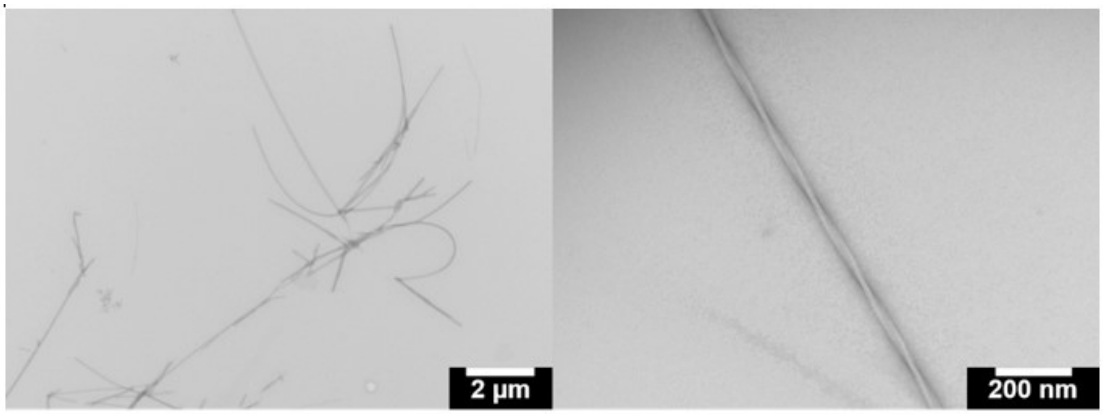

Figure S17 TEM images of 0.1 wt% solution of DVVC10 peptide**.**

B.3.6 Output Curves for Devices with 1 wt% EAA-4T as Gate

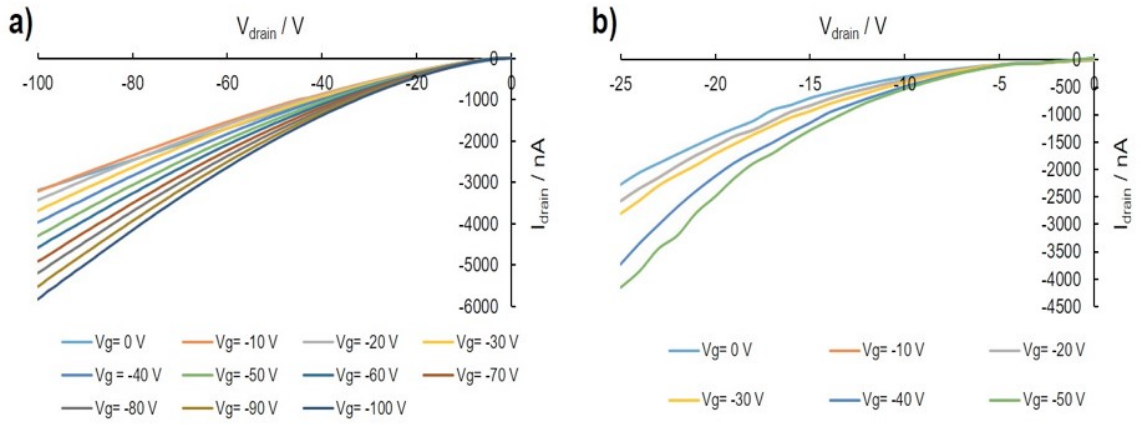

Figure S18 Output curves for devices with 1 wt% EAA-4T as gate, 40-nm pentaerthritol as dielectric and a) PQT-12 (poly(3,3"'-didodecylquaterthiophene)) and b) pentacene as the semiconducting layer.

References

1. Sanders, A. M.; Dawidczyk, T. J.; Katz, H. E.; Tovar, J. D., Peptide-Based Supramolecular Semiconductor Nanomaterials via Pd-Catalyzed Solid-Phase "Dimerizations". *ACS Macro Lett.* **2012,** *1*, 1326-1329.
2. Ardona, H. A. M.; Tovar, J. D., Energy Transfer Within Responsive Pi-Conjugated Coassembled Peptide-Based Nanostructures in Aqueous Environments. *Chem. Sci.* **2015,** *6*, 1474-1484.
3. Ardoña, H. A. M.; Besar, K.; Togninalli, M.; Katz, H. E.; Tovar, J. D., Sequence-Dependent Mechanical, Photophysical and Electrical Properties of Pi-Conjugated Peptide Hydrogelators. *J. Mater. Chem. C* **2015**, *3,* 6505-6514.
4. Wall, B. D.; Diegelmann, S. R.; Zhang, S.; Dawidczyk, T. J.; Wilson, W. L.; Katz, H. E.; Mao, H.-Q.; Tovar, J. D., Aligned Macroscopic Domains of Optoelectronic Nanostructures Prepared via Shear-Flow Assembly of Peptide Hydrogels. *Adv. Mater.* **2011,** *23*, 5009-5014.

About the Author

Kalpana Besar was born on the 1st of May 1989 in Alwar, Rajasthan, India. She completed her undergraduate education in 2011 with a major in Engineering Physics at Indian Institute of Technology Delhi (IITD), India. During her undergraduate program she was exposed to various areas of Engineering Physics such as optics, electromagnetics, and semiconductor device physics. She found the latter particularly fascinating, inspiring her to join Professor Howard Katz's lab at Johns Hopkins University to pursue a PhD in Material Science and engineering right after completing her undergraduate degree.

Professor Katz's lab broadly works with organic semiconductors, exploring and developing areas like thermoelectrics, interfaces, and biochemical sensors. For her dissertation topic Kalpana chose the sensors and biosensors area as that provided an optimal amalgamation of biology and engineering.

During her PhD Kalpana successfully completed five different projects, resulting in eight published manuscripts and four different patent applications. She received a Whiting school fellowship and a Rodbell academic excellence award (2014-2016) for her academic accomplishments.

Apart from investigating her organic field effect devices in Katz's lab, she also likes to read, cook, travel, and click photographs.